Utrecht University

Institute for Marine and Atmospheric research Utrecht

Master Thesis

Applying Mass Conservation to ADCP-data

Author:

Jelle Soons

Supervisors:

Prof. Dr. Leo R.M. Maas
Institute for Marine and Atmospheric research Utrecht

Prof. Dr. Jason E. Frank
Mathematical Institute

August, 2022

Abstract

Adding mass constraints to existing ADCP-data results in improved velocity estimates in various transducer configurations. The problem of estimating vertical velocity with a conventional set-up in horizontally dominant flow is that inhomogenities in the horizontal velocities can cause relatively large errors in the vertical velocity estimate. A possible solution to obtain more accurate vertical velocity estimates using mass constraints is introduced. The corrected data is compared to the original uncorrected data. Then a novel configuration of transducers that is a combination of multiple transducer-receivers in a buckyball set up is discussed. Mass constraints are applied to synthetic data of this set up, and this leads in various circumstances to improved estimates. Also discussed is a proof of concept showing the ability of this set up to measure the shearing motion of internal waves.

Acknowledgements

In the first place I would like to thank my supervisor Leo Maas for giving constructive feedback, for always being enthusiastic about new results, and most importantly for being very patient with me. Without him this thesis would not have been possible. I would also like to thank Jason Frank and Huib de Swart for helpful suggestions throughout my thesis. Furthermore I am grateful for my friends and family. They always listened to my complaints, supported me, and in general kept me sane.

Contents

Chapter 1

Introduction

Within the oceanographic community rapid and accurate measurements of current profiles are vital. The introduction of the acoustic Doppler current profiler (ADCP) in the late 1980s was a major step forward in obtaining these measurements. This device emits sound waves into the water and measures their reflection in order to obtain a reading of the local water currents. It offers multiple advantages over the conventional rotary-type current meters. The spatial resolution of the measurements increased, all three components of the velocities could be measured, and -most importantly- the ADCP allowed for remote sensing of the water column. Using sound waves a typical ADCP can have a range of up to two kilometers penetrating the water[27].

The applications of the ADCP are numerous. It can be mounted underneath a ship and map the current profile of a river, it can be placed looking upward at the bottom of the sea bed measuring wave activity, or it can be hung underneath a buoy in the middle of the ocean. Next to resolving water velocities, it can also be used in combined studies of biomass productivity by for example measuring zooplankton abundance[16].

Since its introduction the ADCP has been developed even further. Several improvements in the way an ADCP obtains measurements have been made, by for example fine tuning the time interval between sound pulses[2]. Other developments have been made regarding post-processing: using the same exact measurements but computing more accurate estimates. Examples of this are corrections in case the apparatus has a slight pitch [24][33], or when one of the returning sound signals is inaccurate [13]. In this thesis an attempt is made to improve the ADCP in both ways: an improved post-processing method is introduced as well as a hardware addition to a conventional ADCP.

In the second chapter the working principles of the ADCP are discussed. Only the relevant aspects are included in order to understand the succeeding chapters. Additionally, some disadvantages of the ADCP are mentioned. Solving these specific problems is tried in the rest of the thesis. In the third chapter a new post-processing method using mass constraints is introduced for conventional four-beam ADCP-measurements. This method is then applied to ADCP-data from a shallow sea resulting in more accurate velocity estimates. Thereafter in the fourth chapter a hardware addition to the ADCP is presented: the ADCP-buckyball. Hereby multiple directions for the sound pulses are added with the goal of observing more complicated water flows that current devices cannot accurately measure. Then the aforementioned post-processing method is applied to this buckyball, and using synthetic data in a simulated environment the ability of the buckyball to capture these complicated flows is analyzed. Thus the aim of this thesis is twofold. Firstly, to show a new processing technique of raw ADCP-data using mass constraints in order to generate more accurate velocity estimates. And secondly, to perform a feasibility analysis of the ADCP-buckyball in a synthetic environment where this processing technique is applied.

Chapter 2

The ADCP and its Problems

As mentioned in the introduction the ADCP has multiple applications and is a widely used device to measure oceanic currents. In this chapter the working principles of an ADCP are discussed: how the current velocities are measured, and how these can be recombined to produce estimates for the velocities. Moreover, a couple of disadvantages of the ADCP are highlighted.

2.1 The Transducer

Every ADCP has multiple transducer-receivers. A transducer is a flat device that transmits a sound pulse at a fixed frequency in one direction, and the receiver listens to echoes returning from sound scatterers in the water, see figure 2.1. These sound scatterers can be for example plankton or sediment floating in the water. Most of the sound energy emitted goes forward, while a part is scattered and a fraction of that returns to the transducer. The frequency of the returning signal is Doppler-shifted due to relative movement of the scatterers with respect to the transducer. So using the effects of Doppler-shifts in figure 2.1 the horizontal velocity of the scatterers can be deduced. Note that only the relative velocity with respect to the sound beam causes a Doppler shift, so any movement perpendicular to the beam is not measured.

Now the critical assumption is made that on average these scattering particles move with the same velocity as the water they are suspended in. Hence averaging the measurements of a couple of returning pings yields the water velocity in the beam direction. A second important condition is that the speed of sound in the water is constant and known. Knowing the speed of sound one can compute how far the returning ping has travelled, and therefore at what distance along the beam the reflection took place. Furthermore, the speed of sound needs to be constant in order for the beam to travel through the water in a straight line. If the speed were not constant refraction of the beam takes place, and the measurements would lie along a curved line. With both conditions holding, the transducer-receiver reports the along-beam velocity of the water along the entire beam.

In practice the beam is regularly spaced into cells, where the cell size (i.e. the length along the beam) is the length of the emitted pulse. For each cell one along-beam velocity is reported. This value is a weighted average of the results of different reflections. The weight functions are triangular and take into account all measurements from reflections that occurred within a pulse length of the centre of the cell. Note that the transducer receives reflections with the end of the pulse from the centre of cell at the same time as reflections with the start of the pulse from the end of the cell. This way these are all combined into one reported value. Moreover, the spacing into cells makes it easier to process and interpret the data. The weight functions and cells are illustrated in figure 2.2. So the length of the cell is determined by the pulse length, which in turn is determined by operational circumstances. A short pulse length leads to smaller cells and hence a better resolution. However, with a longer pulse length the results of more reflections are combined into one along-beam velocity value. So it would be

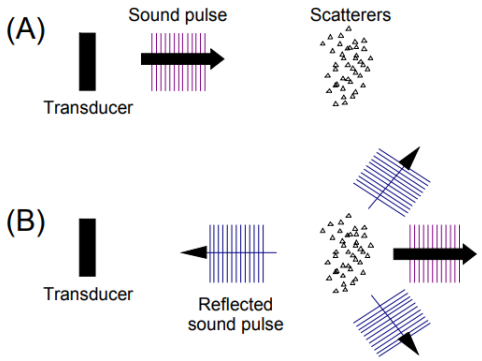

Figure 2.1: Transducer in operation, with (A) a transmitted pulse and in (B) a small amount of the pulse is reflected and returns Doppler-shifted while most goes forward, figure from [17].

the result of more echoes and hence the reported value is less noisy. All in all, the cell size is set by the goal of the measurement campaign.

In figure 2.2 one can also see the blanking distance. This is the distance from the transducer to the start of the first cell. A transducer emits its sound pulse by vibrating or 'ringing'. These vibrations fade away with time. The distance the pulse travels during the attenuation of the ringing is the minimum blanking distance. The echo of any reflection occurring within the blanking distance would arrive at the transducer-receiver while it is still ringing, and in this state the receiver cannot properly measure the returning echo. Therefore no measurements are made within the blanking distance. The size of the blanking distance is determined by the pulse length and the strength of the returning echo. A longer pulse or a very weak echo leads to a larger blanking distance.

Conventional ADCPs use a broad-band Doppler signal. Originally ADCPs were narrow-band, meaning that several pings would be emitted by the transducer all at the same frequency and averaged into a measurement. Now with these original ADCPs one could pick a high-frequency signal, leading to a better resolution since with less short-term variability short spatial and temporal scales could be resolved. This is ideal for use in shallow-water situations where depth resolution is important. However, with a higher frequency the sound absorption increases, and hence the distance the signal can travel decreases. So in open-ocean applications where a long profiling range is required, a low frequency is chosen at the expense of resolution. Nowadays with the broadband ADCP the signal contains a range of frequencies, and so one can overcome both these limitations. The range of a transducer is now only determined by the signal-to-noise ratio (SNR). This is the ratio of the amplitude of the returning signal to the amplitude of the background noise. As the distance to the instrument increases, the SNR drops due to the geometric spreading of the beam and sound absorption. At a certain distance from the instrument the SNR is too low to get reliable velocity estimates: this is the range of the transducer. Beyond this point the transducer can still compute along-beam velocities, but these are not reliable. Usually the threshold is roughly SNR ≈ 1.5 [27]. The SNR of the returning signal is determined by the power of the emitted signal and the scattering properties of the water. Low power usage by the transducer or very clear water -so with relatively few scattering particles- lead to a low SNR and hence a reduced range. A nice overview of the properties of a broadband transducer and its comparison to previous versions is Brumley et al.(1991).

To summarize, a conventional transducer-receiver emits sound beams into the water. Using the Doppler effect the along-beam velocities can be measured. These results are produced along evenly spaced cells along the beam. Necessary conditions are that the sound-scattering particles move with the current, and that the constant speed of sound is known. The range of the transducer-receiver is determined by the strength of the emitted pulse and the scattering properties of the water.

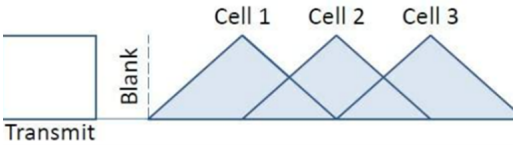

Figure 2.2: Transducer (or transmitter) with a series of cells, where the separation between cells is equal to length of a emitted pulse. At each cell centre there is a triangular weighting function, figure from [28].

2.2 The Set Up

An ADCP consists of multiple transducer-receivers combined in a geometrical configuration. Some consist of only three transducers, but four- or five-beam set ups are more common. Here a simple example is produced of a two-beam ADCP in two-dimensional environment. This illustrates how an ADCP proceeds from a set of along-beam velocities produced by the transducers to a set of current estimations.

Suppose a two-dimensional flow environment with horizontal coordinate x and vertical coordinate z. Since water is incompressible the flow will be divergence-free, and hence the flow can be described by a stream function ψ, where horizontal and vertical water velocities u and w follow via:

$$\begin{cases} u(x,z) &= \psi_z(x,z) \\ w(x,z) &= -\psi_x(x,z), \end{cases}$$

where the subscripts denote a partial derivative.

Now at the bottom of this basin two transducers are placed symmetrically, each inclined with an angle α with the vertical. The set up is illustrated in a dimensionless environment with figure 2.3. Each transducer i produces a set of measurements $b_{i,n}$ with $i \in \{1,2\}$ and $n \in \{1,2,\ldots,N\}$ where n indicates which transducer cell and N is the total numbers of cells. So $b_{1,1}$ is the along-beam velocity measured by the right transducer in the centre of the first cell from the bottom. This set of measurements $b_{i,n}$ is the raw ADCP-data. The distance to the centre of the n^{th} cell to the transducer is denoted by r_n. Then $b_{1,n}$ and $b_{2,n}$ are both along-beam velocities at height $z_n = r_n \cos\alpha$ above the bottom. Next, the volume in between the beams is also regularly divided into voxels where each has height d, and so $d/\cos\alpha$ is the previously discussed cell size in the along-beam direction, i.e. $d/\cos\alpha$ is the pulse length. The spacing of the measurement area into these voxels is also illustrated in figure 2.3.

Next, the homogeneity assumption is made: it is assumed that the flow within each of these voxels is homogeneous. In practice this typically implies that it is assumed that the flow is horizontally homogeneous, which is usually a valid assumption[23]. So for each voxel one has two measurements, each in a different beam direction, of one constant two-dimensional flow. This constant two-dimensional flow in the n^{th} voxel from the bottom is indicated by $(\hat{u}_n, \hat{w}_n)$. Then the along-beam measurements at the edges of this voxel would yield:

$$\begin{cases} b_{1,n} &= \cos(\alpha)\hat{w}_n + \sin(\alpha)\hat{u}_n \\ b_{2,n} &= \cos(\alpha)\hat{w}_n - \sin(\alpha)\hat{u}_n. \end{cases}$$

and recombining these begets that:

$$\begin{cases} \hat{u}_n &= (b_{1,n} - b_{2,n}) \,/\, (2\sin(\alpha)) \\ \hat{w}_n &= (b_{1,n} + b_{2,n}) \,/\, (2\cos(\alpha)) \,. \end{cases} \tag{2.1}$$

Hence the water velocity $(\hat{u}_n, \hat{w}_n)$ in each voxel is computed. These results are used as estimators for the flow at the centre of the voxel, i.e. (u, w) at height z_n above the transducers. These estimators

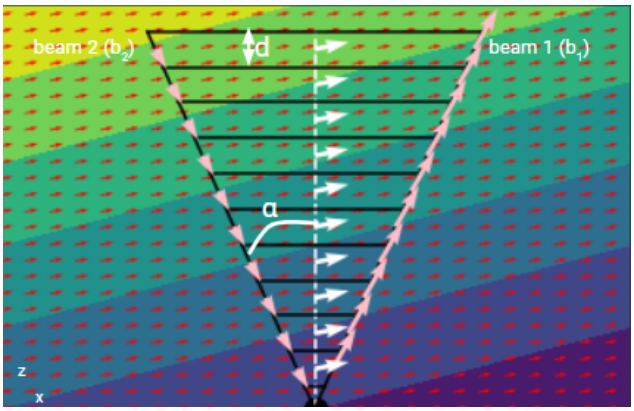

Figure 2.3: A two-beam ADCP in a two-dimensional flow (red arrows) determined by $\psi(x, z) = \frac{z}{2} - \frac{x}{10}$ in basin $(x, z) \in [-80, 80] \times [0, 80]$. Two transducers at the origin, inclined with angle $\alpha = 30°$, with beams b_1 and b_2 from right to left. The along-beam measurements (pink), and computed estimators (white) are not to scale. The estimators lie along a vertical line above the ADCP (dashed white). The voxel size d is indicated.

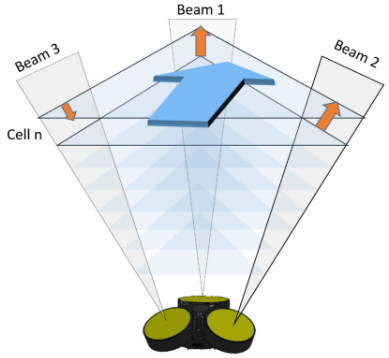

Figure 2.4: A three-beam ADCP, with measurements (orange) in order to compute the three-dimensional flow estimator in the n^{th} voxel, figure from [27].

are indicated by white arrows in figure 2.3, where they coincide exactly with the actual flow at the centre of the voxel, since the simulated flow here is indeed homogeneous within each voxel. So to recap, using this two-beam ADCP a depth profile of the two-dimensional water flow is created. At each voxel height z_n right above the ADCP a two-dimensional estimator of the flow is computed.

In this case a two-beam ADCP is illustrated. A simple extension with a third beam, illustrated in figure 2.4, provides a depth profile for a three dimensional flow. More common is the four-beam ADCP, illustrated in figure 3.1. This is essentially two two-beam ADCPs producing a horizontal and vertical velocity estimator in either the $(x, z)-$ or the $(y, z)-$plane. Note that this provides not only an estimator for the horizontal flow in the $x-$ and in the $y-$direction, but also *two* estimators for the vertical velocity. Each set of two opposing beams yields a vertical velocity estimate. A relatively large difference between these two estimates -the so-called error velocity- indicates that the homogeneity assumption does not hold well, in which case the horizontal estimators might also be invalid. In general the difference between the two estimates for the same vertical velocity is an indicator of the flow inhomogeneity[24].

2.3 Error Analysis

The errors occurring with the use of an ADCP can be split into two groups. Firstly one has intra-beam errors, which are errors in measuring the along-beam velocities within a beam. Secondly there are inter-beam errors, which are errors occurring due to combining the data from different beams.

2.3.1 Intra-Beam Errors

Now a critical assumption is that these scatterers move at the same velocity as the water that they are suspended in. Of course these scattering particles do not follow the flow perfectly which causes an error in the water velocity estimate[14]. Another source of error with this single-beam measurement is that the beam is of finite width: the produced value consists of reflections off all particles within the beam and within the cell. The resulting value is a spatially averaged computation of all these returning echos. So, although in the previous example it seemed as if the measurements were the along-beam component of the water velocity exactly at the centre of the beam and cell, this is certainly not the case. Lastly, the produced measurement is not instantaneous: it is usually the result of the average of several pings. Although modern broadband transducer have excellent single-ping accuracy[14], a demanding turbulent environment requires averaging over several pings in order to filter out any noise to obtain presentable measurements.

So the sources of the intra-beam errors are the spatial and temporal averaging and the inability of the scatterers to always follow the local flow promptly. All these errors depend on the flow properties: what kind of scatterers are suspended, and how steady the flow is in time and space. There are several thorough analyses of these inaccuracies, see for example Guion & Young (2014), or Theriault (1986I & 1986II).

Later in this thesis raw ADCP-data will be synthesised, and therefore a justified model for the intra-beam error is required. It was decided that instead of incorporating the more complicated models of the aforementioned papers, a simpler model should be adopted. It was firstly assumed that the noise in a measurement is Gaussian white noise, similar to the modelling assumptions in Stacey et al. (1999) and Mirshak & Kelley (2008). The magnitude of this error is difficult to quantify since it very much depends on the operational circumstances. Based on ADCP manuals [17][28], and the results in Lu & Lueck(1999I) a standard deviation of 2% of the actual along-beam velocity component is thought to be appropriate. Of course this is a rough estimate, and in turbulent environment this proportional error can actually be as high as 10%[17]. The estimate chosen here is better suited for a shallow-sea environment or a tidally dominated channel. The increase of the error with distance to the transducer due to geometrical spreading of the beam is not included, since it is usually not significant[22].

2.3.2 Inter-Beam Errors

The inter-beam errors are due to an invalid homogeneity assumption. The estimates for the velocities at the centres of the voxels are computed based on the assumption of a homogeneous flow. If this is not the case, this inhomogeneity error occurs, which is again an error very much dependent on environmental circumstances. Throughout this thesis this error will be regularly mentioned. For now it will be illustrated with the previous example of the two-beam ADCP.

Suppose the same two-beam ADCP is placed at the bottom of the basin, i.e. at the origin in the $(x,z)-$plane. The actual flow velocities are $(u(x,z),w(x,z))$ again. Using (2.1) the estimates $(\hat{u}_n,\hat{w}_n)$ for the velocities $(u(0,z_n),w(0,z_n))$ are computed. Now, the actual measured beam velocities -when intra-beam error is omitted- are the along-beam velocity components of the flow at the measurement points $(\pm z_n\tan\alpha,z_n)$. So

$$\begin{cases} b_{1,n} &= \cos(\alpha)w(z_n\tan\alpha,z_n)+\sin(\alpha)u(z_n\tan\alpha,z_n) \\ b_{2,n} &= \cos(\alpha)w(-z_n\tan\alpha,z_n)-\sin(\alpha)u(-z_n\tan\alpha,z_n). \end{cases} \tag{2.2}$$

Substituting equations (2.2) into (2.1) and then Taylor-expanding around the voxel centre $(0, z_n)$ yields for the computed estimates:

$$\begin{cases} \hat{u}_n &= u(0,z_n) + \sum_{k=1}^{\infty} \frac{(z_{2k}\tan\alpha)^{2k}}{(2k)!} \frac{\partial^{2k} u}{\partial x^{2k}}(0,z_{2k}) + \frac{1}{\tan\alpha} \sum_{k=1}^{\infty} \frac{(z_{2k-1}\tan\alpha)^{2k-1}}{(2k-1)!} \frac{\partial^{2k-1} w}{\partial x^{2k-1}}(0,z_{2k-1}) \\ \hat{w}_n &= w(0,z_n) + \sum_{k=1}^{\infty} \frac{(z_{2k}\tan\alpha)^{2k}}{(2k)!} \frac{\partial^{2k} w}{\partial x^{2k}}(0,z_{2k}) + \tan\alpha \sum_{k=1}^{\infty} \frac{(z_{2k-1}\tan\alpha)^{2k-1}}{(2k-1)!} \frac{\partial^{2k-1} u}{\partial x^{2k-1}}(0,z_{2k-1}). \end{cases}$$

So the inter-beam error is extremely sensitive to the type of turbulence present in the flow[14], since significant higher-order derivatives cause a larger deviation of the estimators from the true water velocities. A thorough analysis of the inter-beam error can be found in Theriault (1986II).

2.4 Goal of the Thesis

As mentioned in the Introduction the goal of this thesis is twofold: it is to investigate the usefulness of incorporating mass constraints in ADCP-measurements, and to analyze the feasibility of the ADCP-buckyball.

In section 2.3.2 the inhomogeneity error was introduced. This error is in a planar context the consequence of having two one-dimensional measurements of the flow at the edges of a voxel, and then having to produce a two-dimensional estimate at the centre of the voxel. In order to do so an assumption has to be made about the structure of the flow inside the voxel. Normally the homogeneity assumption is made: the flow is supposedly constant within the voxel. Now, water is incompressible and hence the flow is divergence-free, i.e. mass of the water is conserved[4, Ch 3]. By adding this mass constraint perhaps the homogeneity assumption about the flow structure can be relaxed, and hence the inhomogeneity error might be reduced. This will be examined in the next chapter.

Also, in this thesis the concept of an ADCP-buckyball is introduced. Here multiple transducer-receivers are combined into a buckyball configuration, see figure 4.1. Since this device would measure in a multitude of different directions it might overcome the disadvantage of a conventional ADCP namely that it only produces velocity estimates along one vertical line. This disadvantage is illustrated in figure 2.5: in order to measure the cross-sectional velocity profile of a river an ADCP has to be mounted underneath a crossing boat. Whereas with a buckyball that can measure and produce estimates in multiple directions one only needs to mount it to a buoy in the middle of the river, which is cheaper and easier.

But this is not the main motivation for the buckyball. An example of a complicated underwater flow is the shearing motion associated with an internal wave, which will be further discussed later. Currently it is difficult to reliably measure internal waves with conventional ADCP set ups[3]. Perhaps with the buckyball design this becomes easier. The second goal of this thesis is therefore to examine whether the buckyball set up -using mass constraints- can measure spatial flow inhomogeneities, specifically the wave properties of these internal waves. This is done using synthetic internal wave data in chapter 5.

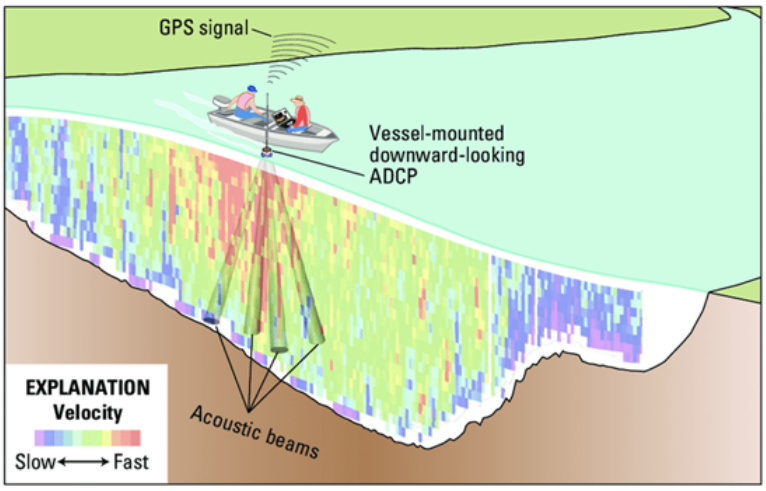

Figure 2.5: A conventional four-beam ADCP mounted at the underside of a boat to measure current profile of a river, figure from [32]

Chapter 3

Mass Constraints in a Conventional Set Up

This chapter discusses the usefulness of applying mass constraints to existing ADCP-data obtained using a regular ADCP set up. Firstly, the problem of estimating vertical velocity with a regular set up in horizontally dominant flow is illustrated. Then a possible solution to obtain more accurate vertical velocity estimates using mass constraints is introduced. This post-processing method is applied to actual ADCP-data from the Irish Sea, and the corrected data is compared to the original uncorrected data. The added bonus of estimates for horizontal velocity gradients, especially as method for estimating turbulence parameters, is also discussed.

3.1 Posing the Problem

Consider a regular four-beam ADCP set up in Janus configuration anchored to the sea bed. It is assumed the apparatus stands completely horizontal, and the horizontal x- and y-axis are aligned with the beams. The set up is also illustrated in figure 3.1. Beams 1 and 2 lie along the x-axis, while beams 3 and 4 lie along the y-axis. The beams have an angle α with the vertical. Furthermore, the beams are divided into N bins with $b_{i,n}$ the measurement of beam i in bin n for $1 \leq n \leq N$ and $i \in \{1, 2, 3, 4\}$. The centre height of each voxel is given by $z_n = Z_0 + (n - \frac{1}{2})d$, where Z_0 is the vertical blanking distance, and d is the vertical separation between subsequent bins.

So for each bin or voxel n the following measurements are made:

$$\begin{cases} b_{1,n} &= \cos(\alpha)w(\mathbf{x}_{1,n}) + \sin(\alpha)u(\mathbf{x}_{1,n}) \\ b_{2,n} &= \cos(\alpha)w(\mathbf{x}_{2,n}) - \sin(\alpha)u(\mathbf{x}_{2,n}) \\ b_{3,n} &= \cos(\alpha)w(\mathbf{x}_{3,n}) + \sin(\alpha)v(\mathbf{x}_{3,n}) \\ b_{4,n} &= \cos(\alpha)w(\mathbf{x}_{4,n}) - \sin(\alpha)v(\mathbf{x}_{4,n}) \end{cases} \tag{3.1}$$

where $\mathbf{u} = (u, v, w)$ is the true velocity field, and $\mathbf{x}_{i,n}$ the centre of beam i at height z_n. Then, usually, the estimates for the velocity field at the centre line $(0, 0, z_n)$ are calculated as follows, based on the assumption that the velocities are homogeneous within each bin over the four beams[24]:

$$\begin{cases} \hat{u}_n &= (b_{1,n} - b_{2,n})/(2\sin(\alpha)) \\ \hat{v}_n &= (b_{3,n} - b_{4,n})/(2\sin(\alpha)) \\ \hat{w}_n &= (b_{1,n} + b_{2,n} + b_{3,n} + b_{4,n})/(4\cos(\alpha)). \end{cases} \tag{3.2}$$

Now, let the true velocity vector at the centre of bin n be denoted by $\mathbf{U}_n = (U_n, V_n, W_n)$, and define

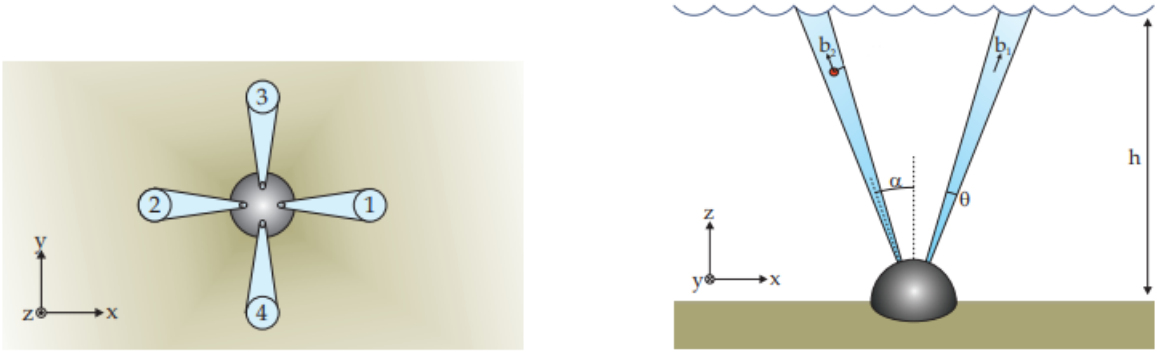

(a) Top view

(b) Transverse view

Figure 3.1: Four-beam ADCP in the Janus configuration, figures from [14]

the actual velocities in beam i and bin n as

$$\mathbf{u}(\mathbf{x}_{i,n}) = \mathbf{U}_n + \tilde{\mathbf{u}}_{i,n}$$

so the usual estimates can be written as:

$$\begin{cases} \hat{u}_n &= U_n + \frac{\tilde{u}_{1,n}+\tilde{u}_{2,n}}{2} + \frac{\tilde{w}_{1,n}-\tilde{w}_{2,n}}{2\tan(\alpha)} \\ \hat{v}_n &= V_n + \frac{\tilde{v}_{3,n}+\tilde{v}_{4,n}}{2} + \frac{\tilde{w}_{3,n}-\tilde{w}_{4,n}}{2\tan(\alpha)} \\ \hat{w}_n &= W_n + \frac{\tilde{w}_{1,n}+\tilde{w}_{2,n}+\tilde{w}_{3,n}+\tilde{w}_{4,n}}{4} + \frac{\tan(\alpha)}{4}(\tilde{u}_{1,n} - \tilde{u}_{2,n} + \tilde{v}_{3,n} - \tilde{v}_{4,n}). \end{cases} \tag{3.3}$$

Next, it is assumed that the inhomogeneities are relatively small compared to the main flow in each bin, hence $|\tilde{u}_{i,n}| \ll |U_n|$, $|\tilde{v}_{i,n}| \ll |V_n|$ and $|\tilde{w}_{i,n}| \ll |W_n|$. Furthermore, in a horizontally dominant flow the horizontal main flow and inhomogeneities are much larger than those of the vertical flow, so $|W_n| \ll |U_n|, |V_n|$ and $|\tilde{w}_{i,n}| \ll |\tilde{u}_{i,n}|, |\tilde{v}_{i,n}|$. So the estimates for the horizontal velocities can be approximated as:

$$\begin{aligned} \hat{u}_n &\underset{\text{since } |\tilde{w}_{i,n}| \ll |\tilde{u}_{i,n}|}{\approx} U_n + \frac{\tilde{u}_{1,n} + \tilde{u}_{2,n}}{2} \underset{\text{since } |\tilde{u}_{i,n}| \ll |U_n|}{\approx} U_n \\ \hat{v}_n &\underset{\text{since } |\tilde{w}_{i,n}| \ll |\tilde{v}_{i,n}|}{\approx} V_n + \frac{\tilde{v}_{3,n} + \tilde{v}_{4,n}}{2} \underset{\text{since } |\tilde{v}_{i,n}| \ll |V_n|}{\approx} V_n \end{aligned}$$

while for the vertical velocity estimate the following approximation holds:

$$\hat{w}_n \underset{\text{since } |\tilde{w}_{i,n}| \ll |\tilde{u}_{i,n}|, |\tilde{v}_{i,n}|}{\approx} W_n + \frac{\tan(\alpha)}{4}(\tilde{u}_{1,n} - \tilde{u}_{2,n} + \tilde{v}_{3,n} - \tilde{v}_{4,n}). \tag{3.4}$$

Here lies the problem. The velocity inhomogeneities are small compared to the horizontal flow, so the horizontal flow estimates have usually a negligible error. However, the horizontal velocity inhomogeneities do not necessarily have to be small compared to the vertical flow. It is indeed not always the case that $|\tilde{u}_{i,n}| \ll |W_n|$ and $|\tilde{v}_{i,n}| \ll |W_n|$. Hence the relative error in the vertical velocity estimate $\hat{w}_n$ can be large. Gargett(1994) already mentioned this problem, and illustrated it by comparing $\hat{w}$ with directly measured vertical velocities.

3.2 Mass Constraints Applied

The continuity equation is applied to correct the original vertical velocity estimate. Let $s = 2z_n \tan(\alpha)$ be the separation distance between two opposing beams in bin n. The following approximations are made:

$$\frac{\partial U_n}{\partial x} \approx (\tilde{u}_{1,n} - \tilde{u}_{2,n})/s \qquad \frac{\partial V_n}{\partial y} \approx (\tilde{v}_{3,n} - \tilde{v}_{4,n})/s.$$

Hence (3.4) becomes

$$\begin{aligned}\hat{w}_n &\approx W_n + \frac{s\tan\alpha}{4}\left(\frac{\partial U_n}{\partial x} + \frac{\partial V_n}{\partial y}\right) \\ &= W_n + \frac{z_n \tan^2\alpha}{2}\left(\frac{\partial U_n}{\partial x} + \frac{\partial V_n}{\partial y}\right) \\ &= W_n - \frac{z_n \tan^2\alpha}{2}\frac{\partial W_n}{\partial z}\end{aligned}$$

where mass conservation was applied by demanding

$$\frac{\partial U_n}{\partial x} + \frac{\partial V_n}{\partial y} + \frac{\partial W_n}{\partial z} = 0$$

for every bin n. A new vertical velocity estimator $\bar{w}_n$ is introduced, inspired by the approximation just found for $\hat{w}_n$:

$$\hat{w}_n = \bar{w}_n - z_n \frac{\tan^2\alpha}{2}\frac{\partial \bar{w}_n}{\partial z}. \tag{3.5}$$

The benefit of this new vertical velocity estimate $\bar{w}$ is that the error caused by the horizontal velocity inhomogeneities is corrected.

Note that with the implemented mass constraint the homogeneity assumption can be relaxed. Whereas previously with the computation of the conventional $\hat{w}_n$ one needed the flow within the voxel to be constant -the homogeneity assumption- in order for $\hat{w}_n$ to be accurate, now with the computation of $\bar{w}_n$ one only needs the second and higher order derivatives of the flow to be negligible within the voxel in order for $\bar{w}_n$ to be accurate.

3.2.1 Analytical Solution to Correction Equation

A continuous version of the correction equation (3.5) would be

$$\hat{w}(z) = \bar{w}(z) - \gamma z \frac{d\bar{w}}{dz} \tag{3.6}$$

where $\gamma = \tan^2(\alpha)/2$. This is a simple ODE with exact solution:

$$\bar{w}(z) = \bar{w}(z_*)\left(\frac{z}{z_*}\right)^{\frac{1}{\gamma}} - \frac{z^{\frac{1}{\gamma}}}{\gamma}\int_{z_*}^{z} \frac{\hat{w}(\tilde{z})}{\tilde{z}^{1+\frac{1}{\gamma}}}\, d\tilde{z}, \tag{3.7}$$

with as boundary condition that $\bar{w} = \bar{w}(z_*)$ at $z = z_*$. Note that equation (3.6) is sensitive to the boundary condition: suppose there is an error δ in the boundary condition, so we use $\bar{w} = \bar{w}(z_*) + \delta$ at $z = z_*$ as condition, then:

$$\bar{w}_{\text{new}}(z) = \bar{w}(z) + \delta\left(\frac{z}{z_*}\right)^{\frac{1}{\gamma}}.$$

Now, since it holds that $\gamma = \tan^2(\alpha)/2 < 1/2$ for all angles $\alpha < \pi/4$ and therefore $1/\gamma > 2$, then this error can grow quite fast at heights $z > z_*$. In the next section it will be discussed how this error is handled.

Next, a theoretical comparison between the corrected and uncorrected vertical velocity estimate can be made. The original uncorrected vertical velocity estimate (3.2) is Taylor expanded:

$$\begin{aligned}
\hat{w}_n =&(b_{1,n} + b_{2,n} + b_{3,n} + b_{4,n})/(4\cos(\alpha)) \\
=&\frac{1}{4}\big(w(s/2,0,z_n) + w(-s/2,0,z_n) + w(0,s/2,z_n) + w(0,-s/2,z_n)\big) \\
&+ \frac{\tan(\alpha)}{4}\big(u(s/2,0,z_n) - u(-s/2,0,z_n) + v(0,s/2,z_n) - v(0,-s/2,z_n)\big) \\
=&w(0,0,z_n) + \frac{z_n\tan^2(\alpha)}{2}\big(u_x(0,0,z_n) + v_y(0,0,z_n)\big) + \frac{z_n^2\tan^2(\alpha)}{4}\big(w_{xx}(0,0,z_n) + w_{yy}(0,0,z_n)\big) \\
&+ \mathcal{O}\big(z_n^4 w_{xxxx}(\zeta_1,0,z_n)\big) + \mathcal{O}\big(z_n^4 w_{yyyy}(0,\xi_1,z_n)\big) \\
&+ \mathcal{O}\big(z_n^3 u_{xxx}(\zeta_2,0,z_n)\big) + \mathcal{O}\big(z_n^3 v_{yyy}(0,\xi_2,z_n)\big) \\
&\text{with } -s/2 < \zeta_1,\zeta_2,\xi_1,\xi_2 < s/2 \text{ and } u_x \text{ indicating } \frac{\partial u}{\partial x} \\
\approx&w(0,0,z_n) + \frac{z_n\tan^2(\alpha)}{2}\big(u_x(0,0,z_n) + v_y(0,0,z_n)\big) \\
&\text{since the flow is horizontally dominant.}
\end{aligned}$$

Hence the leading error term is linear in height and contains the first spatial derivatives of the horizontal velocities, which -as stated before- can be large compared to $w(0,0,z_n)$ itself. The new estimate will correct this, as is shown heuristically in the derivation of (3.5). Assuming that the other errors present in $\hat{w}$ are negligible, then the only error introduced in $\bar{w}$ is due to the sensitivity of the differential equation, which was just discussed. Therefore an analytical approximation for the error term in $\bar{w}$ is

$$\begin{aligned}
\bar{w}_n &\approx w(0,0,z_n) + \epsilon(z) \\
\text{with error } \epsilon(z) &= \epsilon(z_*)\left(\frac{z_n}{z_*}\right)^{\frac{1}{\gamma}}.
\end{aligned}$$

Since $1/\gamma > 2$ the error in $\bar{w}_n$ will grow faster with height z_n than the leading error in $\hat{w}_n$. Nevertheless, as long as the initial error $\epsilon(z_*)$ in $\bar{w}$ at height z_* is small enough compared to the gradients u_x and v_y then the new estimate will be more accurate than the original estimate for the vertical velocity.

3.2.2 Numerical Solution to Correction Equation

In practice the correction equation is solved using finite differences, since the set up is already in N discrete bins with height $z \in \{z_1, z_2, \ldots, z_N\}$ with step size d. The derivative is discretized using the midpoint rule

$$\hat{w}_n = \bar{w}_n - \gamma z_n \frac{\bar{w}_{n+1} - \bar{w}_{n-1}}{2d} \qquad \text{for } 2 \le n \le N-1$$

and at the top of the water column

$$\hat{w}_N = \bar{w}_N - \gamma z_N \frac{\bar{w}_N - \bar{w}_{N-1}}{d}$$

with near-bottom boundary condition

$$\hat{w}_1 = \bar{w}_1.$$

This is motivated by assuming that the estimate $\hat{w}_n$ is most accurate when made close to the apparatus, since errors in the estimate grow with distance z_n. Hence as new estimate in the bottom bin the old estimate is taken. This system of equations is rewritten as

$$\hat{\mathbf{w}} = A\bar{\mathbf{w}}$$

where one has solution $\bar{\mathbf{w}} = (\bar{w}_1, \bar{w}_2, \ldots, \bar{w}_N)^T$, measurements $\hat{\mathbf{w}} = (\hat{w}_1, \hat{w}_2, \ldots, \hat{w}_N)^T$ and discretization matrix

$$A = \mathbb{I}_N - \frac{\gamma}{2d} \begin{pmatrix} 0 & 0 & & & & \emptyset \\ -z_2 & 0 & z_2 & & & \\ & -z_3 & 0 & z_3 & & \\ & & \ddots & \ddots & \ddots & \\ & & & -z_{N-1} & 0 & z_{N-1} \\ \emptyset & & & & -2z_N & 2z_N \end{pmatrix}$$

with $\mathbb{I}_N$ the $N \times N$ identity matrix.

Regularization

As stated before the correction equation (3.6) is sensitive to the boundary condition, and small errors in calculating $\bar{w}_n$ can grow quickly with increasing height in the water column. Therefore some kind of regularization needs to be implemented such that the solution $\bar{w}_n$ does not explode near the top of the water column.

Initially the problem was tackled using Tikhonov regularization [8, Ch 5], where solution $\bar{\mathbf{w}}$ is taken such that

$$\bar{\mathbf{w}} = \text{argmin}\big(||\hat{\mathbf{w}} - A\bar{\mathbf{w}}||_2 + \tau||D_4\bar{\mathbf{w}}||_2\big)$$

with D_4 the discretization matrix for the fourth order derivative and τ the Tikhonov parameter. Essentially one selects here for solutions $\bar{\mathbf{w}}$ that have no fourth or higher order derivative. This method does prevent the solution from blowing up, but the resulting solution is so smooth that small physical phenomena are no longer visible. Hence this approach was abandoned.

Another approach was to 'tie down' the solution at the top. This means that an estimate ω is found for the top estimate $\bar{w}_N$. So the numerical scheme becomes:

$$\begin{aligned} \hat{w}_1 &= \bar{w}_1 \\ \hat{w}_n &= \bar{w}_n - \gamma z_n \frac{\bar{w}_{n+1} - \bar{w}_{n-1}}{2d} \qquad \text{for } 2 \leq n \leq N-1 \\ \omega &= \bar{w}_N \end{aligned}$$

Still the task remains to find a suitable estimate ω. One way was to define ω as

$$\omega = \text{argmin}||\bar{\mathbf{w}} - \hat{\mathbf{w}}||_2$$

where it was assumed that $\bar{\mathbf{w}}$ should not differ much from $\hat{\mathbf{w}}$. However, in practice in some cases the solution still became nonphysical near the top. Ideally, a great estimate for the vertical velocity near the surface would be

$$\omega = \frac{D\zeta}{Dt}$$

with ζ the sea surface height. However, this data is not always available, and moreover the top bin does not necessarily need to be close to the surface. Therefore, it is decided that the best available estimate ω for solution $\bar{w}_N$ is the original measurement:

$$\omega = \hat{w}_N. \tag{3.8}$$

Of course using this as estimate introduces some error into the solution. As derived previously the error in the original measurements is

$$\begin{aligned}\hat{w}_N - w(0,0,z_N) &= \gamma z_N(u_x(0,0,z_N) + v_y(0,0,z_N)) \\ &= -\gamma z_N w_z(0,0,z_N) \sim \gamma z_N \frac{W}{H}\end{aligned}$$

where W is the typical magnitude of the vertical velocity and H the average depth of the water column. Now, since the error $\epsilon(z)$ in the solution $\bar{w}$ goes like $z^{\frac{1}{\gamma}}$, the error introduced by stating $\bar{w}_N = \hat{w}_N$ decreases when descending in the water column. The error δ_n in $\bar{w}_n$ due to (3.8) is

$$\begin{aligned}\delta_n &= \delta_N \big(\frac{z_n}{z_N}\big)^{\frac{1}{\gamma}} \\ &= -\gamma z_N w_z(0,0,z_N)\big(\frac{z_n}{z_N}\big)^{\frac{1}{\gamma}} \\ &\sim \gamma z_N \frac{W}{H}\big(\frac{z_n}{z_N}\big)^{\frac{1}{\gamma}}.\end{aligned}$$

So the error introduced by stating $\bar{w}_N = \hat{w}_N$ will be insignificant, say $|\delta_n| < 0.05W$, beneath a certain depth:

$$z_n < z_N\big(\frac{H}{20\gamma z_N}\big)^{\gamma} \tag{3.9}$$

which in practice means that a few top bins will not have the first order correction that $\bar{w}_n$ has compared to the original estimates $\hat{w}_n$.

Lastly, it was noted that since there is a stated boundary condition at the top, the boundary condition near the bottom is no longer necessary. Therefore near the bottom an Euler Backward scheme was implemented. Leading to

$$\begin{aligned}\hat{w}_1 &= \bar{w}_1 - \gamma z_1 \frac{\bar{w}_2 - \bar{w}_1}{d} \\ \hat{w}_n &= \bar{w}_n - \gamma z_n \frac{\bar{w}_{n+1} - \bar{w}_{n-1}}{2d} \qquad \text{for } 2 \le n \le N-1 \\ \hat{w}_N &= \bar{w}_N\end{aligned}$$

In conclusion, to compute $\bar{\mathbf{w}}$ the linear system:

$$\hat{\mathbf{w}} = B\bar{\mathbf{w}} \tag{3.10}$$

is solved with discretization matrix B

$$B = \mathbb{I}_N - \frac{\gamma}{2d}\begin{pmatrix} -2z_1 & 2z_1 & & & & \emptyset \\ -z_2 & 0 & z_2 & & & \\ & -z_3 & 0 & z_3 & & \\ & & \ddots & \ddots & \ddots & \\ & & & -z_{N-1} & 0 & z_{N-1} \\ \emptyset & & & & 0 & 0 \end{pmatrix}.$$

3.2.3 Estimating Horizontal Gradients

Using the corrected vertical velocity estimate $\bar{w}_n$ one can get estimates for the spatial gradients of the horizontal velocities u_x and v_y as an added bonus. These estimates are formulated as

$$\begin{cases} \frac{\partial \bar{u}_n}{\partial x} &= \frac{b_{1,n}+b_{2,n}-2\cos(\alpha)\bar{w}_n}{s\sin(\alpha)} \\ \frac{\partial \bar{v}_n}{\partial y} &= \frac{b_{3,n}+b_{4,n}-2\cos(\alpha)\bar{w}_n}{s\sin(\alpha)}. \end{cases} \tag{3.11}$$

Note that if the true vertical velocity $w(\mathbf{x})$ were known, these estimates can be rewritten using Taylor expansions around the centre of the bin to formulate the best-case-scenario for these estimates:

$$\begin{aligned}
\frac{\partial \bar{u}_n}{\partial x} =& \frac{b_{1,n} + b_{2,n} - 2\cos(\alpha) w(0,0,z_n)}{s\sin(\alpha)} \\
=& \frac{1}{s\sin(\alpha)} \Big(\sin(\alpha) u(s/2,0,z_n) + \cos(\alpha) w(s/2,0,z_n) - \sin(\alpha) u(-s/2,0,z_n) \\
& + \cos(\alpha) w(-s/2,0,z_n) - 2\cos(\alpha) w(0,0,z_n) \Big) \\
=& u_x(0,0,z_n) + \mathcal{O}\big(z_n u_{xx}(\zeta_1,0,z_n)\big) + \mathcal{O}\big(z_n w_{xx}(\zeta_2,0,z_n)\big) \qquad \text{for } -s/2 < \zeta_1, \zeta_2 < s/2
\end{aligned}$$

and similarly

$$\frac{\partial \bar{v}_n}{\partial y} = v_y(0,0,z_n) + \mathcal{O}\big(z_n v_{yy}(0,\xi_1,z_n)\big) + \mathcal{O}\big(z_n w_{yy}(0,\xi_2,z_n)\big) \qquad \text{for } -s/2 < \xi_1, \xi_2 < s/2.$$

Hence these estimates have -at best- a leading error term linear in height and second derivatives of the velocities.

Also, note that these gradient estimations just produce the straining rate when $\hat{w}$ is used as vertical velocity estimate. Plugging $\hat{w}$ into the estimate for u_x yields:

$$\begin{aligned}
\frac{b_{1,n} + b_{2,n} - 2\cos(\alpha)\hat{w}_n}{s\sin(\alpha)} =& \frac{1}{s\sin(\alpha)} \big(b_{1,n} + b_{2,n} - \frac{1}{2}(b_{1,n} + b_{2,n} + b_{3,n} + b_{4,n}) \big) \\
=& \frac{1}{2s\sin(\alpha)} \big(b_{1,n} + b_{2,n} - b_{3,n} - b_{4,n} \big) \\
=& \frac{1}{2} \big(u_x(0,0,z_n) - v_y(0,0,z_n) \big) + \mathcal{O}(z_n u_{xx}(\zeta_1,0,z_n) + \mathcal{O}(z_n v_{yy}(0,\xi_1,z_n) \\
& + \mathcal{O}(z_n w_{xx}(\zeta_2,0,z_n) + \mathcal{O}(z_n w_{yy}(0,\xi_2,z_n)) \\
& \text{for } -s/2 < \zeta_1, \zeta_2, \xi_1, \xi_2 < s/2
\end{aligned}$$

and similarly as estimate for v_y:

$$\begin{aligned}
\frac{b_{3,n} + b_{4,n} - 2\cos(\alpha)\hat{w}_n}{s\sin(\alpha)} =& \frac{1}{2} \big(v_y(0,0,z_n) - u_x(0,0,z_n) \big) + \mathcal{O}(z_n u_{xx}(\zeta_1,0,z_n) + \mathcal{O}(z_n v_{yy}(0,\xi_1,z_n) \\
& + \mathcal{O}(z_n w_{xx}(\zeta_2,0,z_n) + \mathcal{O}(z_n w_{yy}(0,\xi_2,z_n)) \\
& \text{for } -s/2 < \zeta_1, \zeta_2, \xi_1, \xi_2 < s/2.
\end{aligned}$$

So these expressions are quite useless as estimates for the velocity gradients u_x and v_y when $\hat{w}$ is applied as vertical velocity estimate.

Lastly, it needs to be noted that the estimates $\frac{\partial \bar{u}_n}{\partial x}$ and $\frac{\partial \bar{v}_n}{\partial y}$ in combination with $\bar{w}_n$ guarantee mass conservation in each bin n:

$$\begin{aligned}
\frac{\partial \bar{u}_n}{\partial x} + \frac{\partial \bar{v}_n}{\partial y} =& \frac{1}{s\sin(\alpha)} \big(b_{1,n} + b_{2,n} + b_{3,n} + b_{4,n} - 4\cos(\alpha)\bar{w}_n \big) \\
=& \frac{4}{s\tan(\alpha)} \big(\hat{w}_n - \bar{w}_n \big) \\
=& -\frac{\partial \bar{w}_n}{\partial z}.
\end{aligned}$$

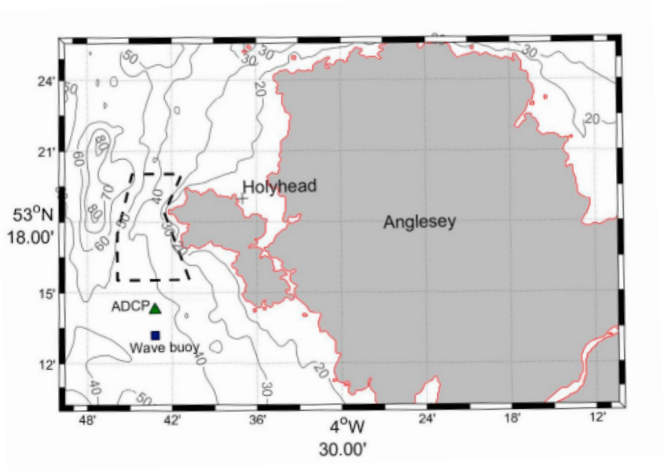

Figure 3.2: Location of the ADCP off the coast of Anglesey, and the extent of the West Anglesey Demonstration Zone shown by dashed black lines. Figure from [42].

3.3 Results: Processed ADCP-data

The ADCP-data presented here was kindly provided by M.Togneri [42], and can also be obtained online through the *IMARDIS*-portal. The data is obtained with a deployment of an RDI Sentinel V five-beam ADCP near the West Anglesey Demonstration Zone off the Welsh Coast; a map of the deployment zone is shown in figure 3.2. This apparatus has a standard Janus configuration with an additional fifth vertical beam in the middle. Here the analyzed data was recorded between 19/9/2014 and 22/9/2014 for a total of nearly three full days. The water depth at the site was measured using the fifth central beam and with the ongoing tidal motion varied in this time between 43.7m and 47.3m. The vertical velocity measurements done by the fifth beam are ignored, since their average deviation from $\hat{w}$ and $\bar{w}$ are relatively large at roughly 0.01m/s. Average velocity magnitudes were $U \sim 0.4$m/s, $V \sim 0.8$m/s and $W \sim 0.02$m/s. So the flow was horizontally dominant, which makes this data-set suitable for the previously described post-processing. There was a blanking distance $Z_0 = 1.89$m between the instrument and the first bin, and subsequent bins had a vertical separation of $d = 0.6$m. In the analysis the first $N = 60$ bins from the bottom are taken into account. The beam angle with respect to the vertical was $\alpha = 25°$. The ADCP collected at a sampling rate of 2Hz for fifteen minutes every hour, and at a sampling rate of $\frac{1}{15}$Hz for the remaining time. The ping frequency was 491kHz, and the tilt of the apparatus remained constant at 2°. Note that the previous analysis still holds if the apparatus has a slight tilt, as long as the tilt is roughly constant and the velocity along this 'tilted vertical' is small compared to the other velocity directions. The average water depth is $H \sim 45m$, and $\gamma = \tan(25°)^2/2 = 0.11$, so using (3.9), the effect of estimating the vertical velocity in top bin with the original measurement can be neglected beneath a depth of 35.2m, in other words only the top 3 bins are affected by using $\hat{w}_N$ as top estimate.

Given from the data are four series of beam measurements. Firstly, the data is re-sampled by averaging all measurements that occurred within one minute such that for each minute for each beam one value is recorded. Hence one has $b_{1,t,n}$, $b_{2,t,n}$, $b_{3,t,n}$ and $b_{4,t,n}$ for the four beams, each at minute t with $1 \leq t \leq T$ where $T = 4144$ minutes and at bin n with $1 \leq n \leq N$ where $N = 60$. Then the beam data is smoothed with a 15-minute moving average in order to reduce the impact of any inaccurate single measurement [42].

From the smoothed beam data the regular estimates $\hat{u}_{t,n}$, $\hat{v}_{t,n}$ and $\hat{w}_{t,n}$ are determined using the equations (3.2). The new vertical velocity estimates $\bar{w}_{t,n}$ are computed from $\hat{w}_{t,n}$ using the numerical method from (3.10).

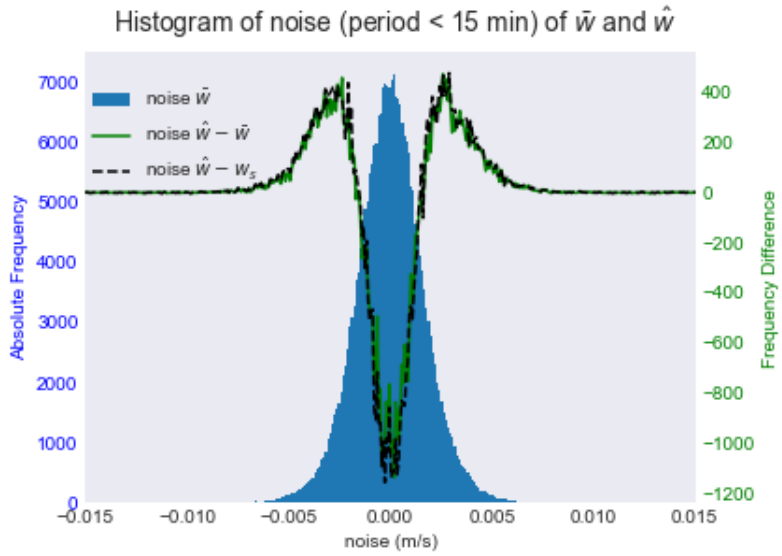

Figure 3.3: Histograms of the noise-signals (period less than 15 minutes) in estimators $\hat{w}$, w_s and $\bar{w}$, with on the left vertical axis the absolute frequency of the noise in $\bar{w}$, and on the right vertical axis the frequency difference with the noise in $\hat{w}$ and in w_s.

3.3.1 Noise Comparison

A straightforward comparison is by analyzing how noisy each series is [13]. Firstly, for each series $\hat{w}_{t,n}$ and $\bar{w}_{t,n}$ signals with a period of less than 15 minutes are removed using a spectral filter. Each distribution of these noise signals are symmetric around zero and moreover, for both extracted signals their respective auto-correlation stays within 0.4, so it is justified to classify this as white noise. A comparison of the noise in each estimator can be seen in the histogram in figure 3.3. From the frequency differences, it is observed that the $\bar{w}$-estimator has more cases (negative difference) in the lower noise-classes (less than 0.02m/s) than $\hat{w}$, and vice versa in the higher noise-classes, resulting in a higher peak with a smaller base. Both distributions are roughly symmetric around zero, with negligible averages $-4.8 \cdot 10^{-20}$m/s and $-4.6 \cdot 10^{-20}$m/s, and standard deviations 0.17cm/s and 0.21cm/s for the noise $\bar{w}$ and $\hat{w}$ respectively. Hence, it can be concluded that the new estimator is clearly less noisy than the old one. For the sake of comparison another estimator w_s is introduced, where w_s at bin n is the average of the estimators $\hat{w}$ from the nearest 5 bins to bin n i.e. w_s is a vertically smoothed version of $\hat{w}$. This produces roughly the same noise-levels as $\bar{w}$. Estimator $\bar{w}$ has the same smoothing effect as averaging over the nearest 5 bins, but is not the same, as will be shown in the next paragraphs.

3.3.2 Comparison with Smoothing

In figure 3.4 an overview of some vertical profiles of $\hat{w}$, $\bar{w}$ and w_s during half a M_2-period are presented. It shows that the corrected estimator $\bar{w}$ contains fewer and lower spikes than the uncorrected original estimator $\hat{w}$, especially for higher bins. For lower bins near the apparatus it was assumed that the errors introduced by inhomogeneities are less relevant since the beams are less separated than at the top. Therefore for lower bins the two estimators coincide more, although also here spikes are still damped. Meanwhile, the smoothed version w_s also contains less spikes, but the difference with $\hat{w}$ is equally large at every depth. Moreover, w_s and $\bar{w}$ still differ significantly although they have the same noise levels. As will be discussed later, there are some nice examples where the difference between w_s and $\bar{w}$ can be justified. In any case figure 3.4 already indicates that $\bar{w}$ is not just a smoothed version of $\hat{w}$. Lastly, it needs to be noted that a temporal spectral analysis of $\bar{w}$, $\hat{w}$ and w_s does not show any

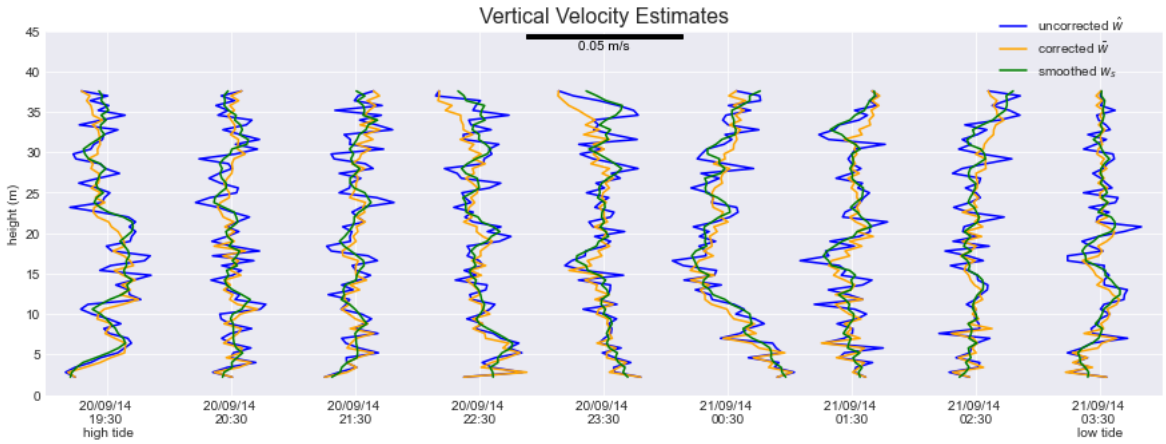

Figure 3.4: Vertical profiles of $\bar{w}$ and $\hat{w}$ from various times on 20/09/14 going from high tide to low tide, showing that $\bar{w}$ is a smoother version of $\hat{w}$. All computed with 15-minutes smoothed beam data from an ADCP-deployment[42].

significant differences. For instance, the magnitude of the tidal constituents of both estimators does not differ. By contrast the vertical spectra of the estimators do differ.

Now, in some ways w_s and $\bar{w}$ do not differ significantly as they have roughly the same spectrum and noise levels. However, small features show the difference between them. One such feature is shown in figure 3.5. In this figure $\hat{w}$, $\bar{w}$ and w_s for the same heights and times are shown, and all three indicate that between 26m and 35m above the sea-bed upwelling occurs. The original estimator $\hat{w}$ and its smoothed version w_s suggest that this upwelling starts at roughly 31m and then moves upward in a period of 20 minutes, while $\bar{w}$ suggests that this upwelling starts almost instantaneously over all heights 31m to 35m. Now, physically this last case makes more sense. As the ADCP is located on a shelf sea where depth never exceeds 48m, the water is vertically well-mixed and the local fluid dynamics are barotropic. This is confirmed by the fact that at this time and depth the horizontal velocity estimates $\hat{u}$ and $\hat{v}$ show no clear vertical structure, and by the fact that heights 30m-35m fall outside the Ekman layers. The latter fact follows from typical Ekman boundary thickness of roughly 10m [4, Ch 8] and at that time the total water height was 47m. So the bins 30m-35m are well away from surface and bed. Now, since circumstances are barotropic the vertical velocity changes only linearly with height [4, Ch 7]. This is the case for $\bar{w}$ in figure 3.5, but not with w_s and $\hat{w}$ where the vertical velocity initially increases and then decreases again with height. So not only does figure 3.5 show that the new estimator $\bar{w}$ is not the same as a simple vertical smoothing of $\hat{w}$, but it also shows that $\bar{w}$ is a more physically sound estimate of vertical velocity.

This last claim, that $\bar{w}$ is more physically realistic than $\hat{w}$ and w_s since it is more barotropic, can be made more concrete. At each time t the absolute differences between the local and the mean vertical gradients of the depth profiles of the estimates $\bar{w}$, w_s and $\hat{w}$ are calculated. These differences should be zero in a perfect barotropic setting. Here the estimates which are within 7.5m of the sea bed are omitted in order to neglect effects from bottom friction. The residual differences between the mean velocity gradient and the local gradients are pooled together. For the original measurements $\hat{w}$ there is a standard deviation of 0.0054/s, while for w_s it is 0.0023/s and for $\bar{w}$ 0.0019/s. This again shows that $\bar{w}$ is more than just a smoothed $\hat{w}$.

3.3.3 Horizontal Gradients

Lastly, the added bonus of this new estimator is presented: the estimates of the horizontal gradients. It was found that these estimates are quite noisy. These estimates have magnitudes $\frac{\partial \bar{u}_n}{\partial x} \sim 0.002$/s and

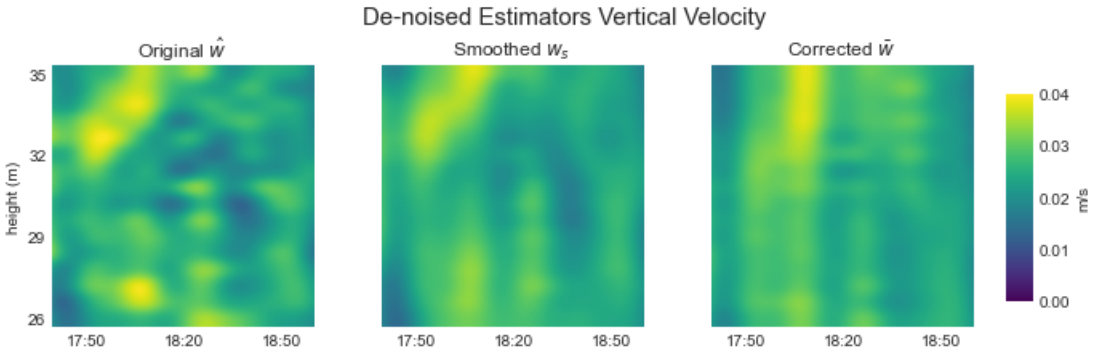

Figure 3.5: Three estimators for the vertical velocity at heights 29m to 37m on 19/09/14 between 17:40 and 19:00: original estimator $\hat{w}$, new estimator $\bar{w}$ based on mass conservation, and vertically smoothed w_s. The estimates shown in this figure are de-noised i.e. all signal with a period of less than 15 minutes is removed.

$\frac{\partial \bar{v}_n}{\partial y} \sim 0.002$/s, while the associated noise -as before all signal with a period of less than 15 minutes- is not much smaller. For both estimates the noise has a magnitude of roughly 0.0006/s, which is quite a large proportion of the estimators themselves.

In order to see some coherence a spectral filter is applied for periods of at least 5.3 hours. The tidal components in the signal might indicate that the gradients are sensible. The estimates do show the tidal signal that is also present in the $(\hat{u}, \hat{v})$-estimates. However, it is hard to prove the reliability of these spatial gradient estimates. It is tried to indicate reliability by assuming the tidal wave was either a simple propagating or standing wave or behaved like a Kelvin wave in a channel[38], and then to compare the fits to $(\hat{u}, \hat{v})$ and $\left(\frac{\partial \bar{u}_n}{\partial x}, \frac{\partial \bar{v}_n}{\partial y}\right)$, but this does not yield any hard conclusive results. It could be that the separation between the beams is just too small for any passing tidal wave to cause any significant difference between the two beams compared to the effects caused by -for example- local eddies. That notion is supported by the spectra of $\frac{\partial \bar{u}_n}{\partial x}$ and $\frac{\partial \bar{v}_n}{\partial y}$: for both it holds that signals with relatively high frequencies (periods less than an hour) are as prominent as signals in the tidal range.

3.3.4 Turbulence Estimation

However, these horizontal gradient estimates might be useful in the estimation of turbulence parameters in a horizontally dominant flow. As per Lu&Lueck(1999II) in order to estimate turbulence quantities using a four beam ADCP in a Janus set up one has to postulate the anisotropy ratio α_{iso}, since it cannot be determined with only four beams. Here, a method is presented to obtain this ratio using four beams and the constraint of mass conservation.

Firstly, again following Lu&Lueck(1999II), the velocities are decomposed into a mean part and a turbulent fluctuating part:

$$\mathbf{U}_n = \langle \mathbf{U}_n \rangle_\tau + \mathbf{u}'_n$$

where $< \cdot >_\tau$ indicates a time average over a period τ. For a typical tidal channel, as here is the case, τ should be roughly 10 to 20 minutes [24][35]. Here, $\tau = 20$ minutes is used, since this is also the time period applied in Togneri et al.(2017) in which the same data set is analyzed.

The anisotropy is defined [25] as

$$\alpha_{iso} = \frac{< w'^2 >_\tau}{< u'^2 >_\tau + < v'^2 >_\tau}$$

which is a measure of turbulence anisotropy. It is the ratio of the contribution of the vertical velocity to the turbulent energy in the flow compared to the contribution of the horizontal velocities. The

ratio α_{iso} ranges from zero for an extremely anisotropic turbulent flow where all turbulence is in the horizontal flow direction, to 0.5 for isotropic turbulence where turbulent flow contributes equally in each dimension. As mentioned this value cannot be determined from an ADCP with only four beams, and the addition of a fifth beam is needed to measure the variance of w. The problem with the four-beam set up is that the variance of the vertical estimate cannot be separated from the variance in the horizontal flow, and hence an independent estimate of the vertical velocity is needed.

However, with the addition of mass constraints it might be possible to compute α_{iso} after all. At each time t the following estimates are made:

$$< w'^2 >_\tau \Big|_{z_n} =< \bar{w}_{t,n}^2 >_\tau - < \bar{w}_{t,n} >_\tau^2$$

which is the variance of the vertical velocity estimates $\{\bar{w}_{t',n}\}_{t-\tau/2\leq t'\leq t+\tau/2}$. For the turbulence due to the horizontal velocities the gradient estimates are used. The fluctuation at time t and height z_n is estimated as:

$$u'_{t,n} = z_n \tan(\alpha)\frac{\partial \bar{u}_{t,n}}{\partial x}$$
$$v'_{t,n} = z_n \tan(\alpha)\frac{\partial \bar{v}_{t,n}}{\partial y}$$

and so for the estimation of horizontal turbulence

$$< u'^2 >_\tau \Big|_{z_n} =< \left(z_n \tan(\alpha)\frac{\partial \bar{u}_{t,n}}{\partial x}\right)^2 >_\tau$$
$$< v'^2 >_\tau \Big|_{z_n} =< \left(z_n \tan(\alpha)\frac{\partial \bar{v}_{t,n}}{\partial y}\right)^2 >_\tau$$

which are the averages of the squares of the sets $\{u'_{t,n}\}_{t-\tau/2\leq t'\leq t+\tau/2}$ and $\{v'_{t,n}\}_{t-\tau/2\leq t'\leq t+\tau/2}$ respectively. Note that in the estimation of $u'_{t,n}$ it is assumed that the fluctuation of u in the x-direction is a good representation of the actual turbulent part $u'_{t,n}$, i.e. it is assumed that the fluctuation is isotropic. The same assumption is made for the estimation of $v'_{t,n}$.

Combining these would yield an estimate for the anisotropy ratio at time t and height z_n. This is combined into the depth-averaged ratio at time t:

$$\alpha_{iso}\big|_t = \frac{1}{n_1 - n_0}\sum_{n=n_0}^{n_1} \frac{< w'^2 >_\tau \Big|_{z_n}}{< u'^2 >_\tau \Big|_{z_n} + < v'^2 >_\tau \Big|_{z_n}}$$

where the averaging is done over bins n_0 to n_1. To correct for the disturbing effect of surface waves only the deepest 20 m of the water column is taken into account, as is done in Togneri et al.(2017). Hence $n_0 = 1$ and $n_1 = 35$ are taken.

The results can be seen in figure 3.6. Figure 3.6(a) shows the depth-averaged ratio in time as just discussed. The bottom figure (b) depicts the time-averaged ratio per bin. Three depth profiles are shown: one of the ratio averaged over all three days, one averaged over all intervals with high tide and one averaged over all intervals with low tide. It can be seen that the ratio varies quite strongly in time, and therefore its moving average is added in (a). Averaging all values over all bins and the whole 3 days yields $\alpha_{iso} = 0.10 \pm 0.04$.

A couple trends can be seen in figure 3.6. Firstly, looking at the depth profile it seems that the turbulence is more isotropic near the bottom than in the rest of the water column. For heights 10m to 35m it seems that $\alpha_{iso} \sim 0.08$, while in the lowest 10m the ratio increases with depth to roughly 0.25. Secondly, the ratio is slightly out of phase with the surface height. This can be observed when comparing the surface height and the moving time average. Another indication for this would be the depth profile: at most heights the ratio during high tide is greater than during low tide. This observation can be made more substantial by computing the correlation between the moving time average and the surface height. The correlation between the surface height and the 2-hour delayed

ratio is as high as 0.78. Both have roughly a period of 12.3h (the M_2-tide), so the ratio is $\frac{\pi}{3}$ out of phase with the tide. In the same figure the depth-averaged horizontal velocity magnitude is added in the lower panel, which shows that the horizontal velocity is smallest a couple hours after high and low tide.

The reduction of anisotropy near the bottom is expected and has been measured for different beds [5, Ch 3]. Furthermore, the delayed increase in isotropy after high tide can be explained intuitively: the combination of high surface water, which allows for larger vertical motions [29], and the small horizontal velocities just after high tide, brings on an increase in isotropy. Now, in literature for a typical tidally dominated, non-rotating and completely unstratified channel often $\alpha_{iso} \approx 0.2$ is used [24][35], which is also used in the Irish Sea [42]. The average value found with this method is about two standard deviations below this standard value. Of course it could be that the method presented here is biased. The estimates for the horizontal fluctuations may not be that reliable. Moreover, the vertical velocity turbulence could be underestimated when using $\bar{w}$ which is an already smoothed version of the original $\hat{w}$. However, the conditions for the standard $\alpha_{iso} \approx 0.2$ do not completely hold here. For instance, adding stratification would reduce vertical motion, and hence decrease isotropy [35]. So a value lower than the theoretical 0.2 can be expected. Moreover, the computed values are closer to 0.2 during high surface levels, which can also be explained by the reduced effect of surface waves on the lower water depths. So the ratio might be closer to the standard values if one were to select for data with hardly any surface waves [42].

3.4 Conclusion on Mass Constraints with four-beam Set Up

The standard beam-to-current velocity components solution, described in (3.2), has been and will continue to work well for many years. However, it relies on the homogeneous velocity field assumption, which is a drawback when measuring 3D currents or when the flow is horizontally dominant but the vertical velocity is of relevance [9]. Here, a processing method for the data, based on the principle of mass conservation, was introduced. It was shown that this process will increase the quality of the vertical velocity data for a horizontally dominant flow. Not only did this method have a smoothing effect and reduced the noise in the data, but it did also produce on small scales physically more realistic signals. Equally important is the fact that the background reasoning behind this method is quite clear and simple. Of course, as seen in the mathematical analysis, the accuracy of these new estimators can decrease quickly with distance to the apparatus, and so the resulting new estimators need to be compared with the original old estimates to make sure they don't deviate extremely far from the device. Furthermore, it needs to be suggested that this processing method can further increase data quality with other correction techniques, such as a method to correct for the tilt [33], or a weighted-least-squares approach where beams are weighted according to their own reliability[13].

The presented method also allows for estimates of the horizontal velocity gradients. The accuracy of these estimates can be questioned. For tidal time scales the results do not produce expected results. However, for the estimation of turbulence parameters these velocity gradients can be useful. Moreover, an additional benefit of these estimates -besides having an estimate for the velocity gradients- is that the homogeneity assumption in each horizontal direction for the ADCP can be directly quantified. Other methods [24] of testing the homogeneity assumption rely on the magnitude of the error velocity. A disadvantage with this error velocity is that it makes no distinction between the two horizontal directions. With the new gradient estimates this would be possible. If inhomogeneity is large in one direction, but not in the other, then the beams along this 'homogeneous direction' can still be reliably used to produce velocity estimates.

Lastly, the main goal of this chapter was to illustrate the benefit of mass constraints for already-existing ADCP-data. It has been show that indeed mass constraints can be of use. Theoretically with mass constraints the homogeneity assumption can be relaxed and the computed estimates should be more accurate. As long as higher order derivatives of the flow can be neglected. Furthermore, in practice improved estimates are obtained. So applying mass constraints partially removes the

inhomogeneity error. With these results it can be justified that this processing method is also applied to the buckyball in upcoming simulations.

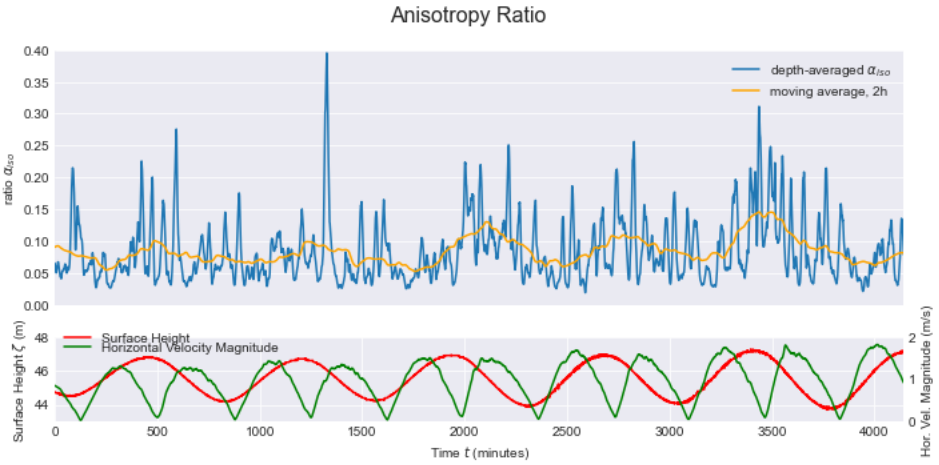

(a)

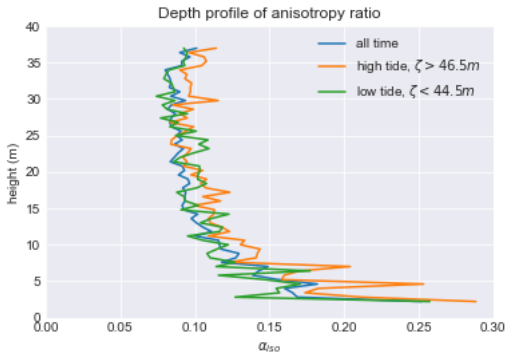

(b)

Figure 3.6: Top figure (a) depicts the depth-averaged anisotropy ratio as described in text, and its rolling average over 2 hours. Underneath it the surface height ζ and horizontal velocity magnitude is shown. Bottom figure (b) is the depth profile of the time-averaged anisotropy ratio, for ratio during all three days, during high tide ($\zeta > 46.5$m) and during low tide ($\zeta < 44.5$m).

Chapter 4

Mass Constraints in a Buckyball Set Up

This chapter introduces the simulation environment for the feasibility study of the buckyball. Moreover, the post-processing method of using mass constraints is applied to this set up. Similar to the previous chapter also here one can conclude that mass constraints can lead to more accurate velocity estimates by relaxing the homogeneity assumption.

4.1 The Buckyball

As stated before the buckyball is a set up of multiple transducer-receivers in a buckyball configuration, illustrated in figure 4.1. The idea is originally by L.R.M. Maas. The obvious advantage of this device is that it can produce velocity estimates in many directions, and not only in one.

In this thesis this device will be analyzed in a two-dimensional setting in order to simplify computations. The two-dimensional version of the buckyball is illustrated in figure 4.2. It was decided to use six transducer-receivers in a hexagonal set up. This way there is still a symmetrical setting with the minimal number of transducers, where this minimal number of six transducers is determined by the common ADCP devices. Conventionally the maximum angle between two opposing beams of an ADCP-apparatus is 60° [28], which is also the case here.

In figure 4.2(a) the general idea behind the feasibility study is illustrated: a synthetic streamfunction with the associated flow field is generated. Note that this guarantees a divergence-free flow in which mass is conserved. At equispaced distances along the radial transducer beams measurements are done. These measurements are the local radial component of the velocity field, with a 2% proportional Gaussian error, as discussed in section 2.3.1. So the goal is to approximate the flow field knowing only these measurements and the measurement locations. In this chapter it is examined whether this approximation can be improved by not only using the measurements but also adding mass conservation constraints. In the next chapter as synthetic flow the shearing motion associated with an internal wave is used, and it is examined how well this flow field can be approximated.

The following notations are introduced, as can be seen in figure 4.2(b). The apparatus lies with its centre at the origin in a $(x, z)-$plane. There are 6 transducer-receivers each directed with polar angle θ_i for $i \in \{1, 2, \ldots, 6\}$ where $\theta_i = \frac{\pi}{3}\left(i - \frac{1}{2}\right)$. Each transducer has blanking distance R_0, and cell size d with in total N cells. Hence there are in each beam N measurements, where the n^{th} measurement is placed at a distance $r_n = R_0 + \left(n - \frac{1}{2}\right) d$ from its corresponding transducer. The range is then $r_N + \frac{d}{2} = R_0 + Nd$. The measurement done by transducer i at the centre of cell n is denoted by $M_{i,n}$, and is placed at point $\mathbf{s}_{i,n} = r_n(\cos\theta_i, \sin\theta_i)$.

Like a conventional set up the measurement area here is also divided into voxels. With $\Omega_{i,n}$ is the n^{th} voxel denoted between beams i and $i-1$ (one beam further clockwise). The voxels lie in 6 different

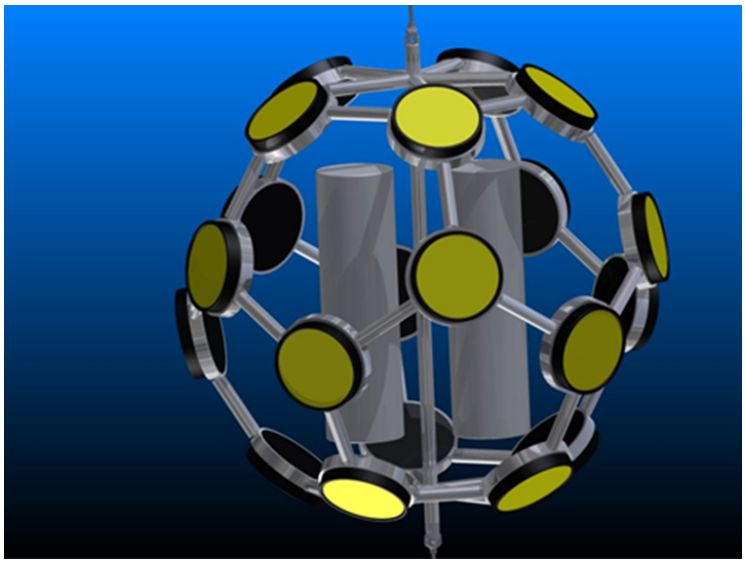

Figure 4.1: The ADCP-Buckyball, with 20 transducers in a buckyball configuration at the edges of a dodecahedron, figure provided by L.R.M. Maas.

angular sections. So all voxels $\Omega_{i,n}$ lie in section i. Moreover, for voxel $\Omega_{i,n}$ one has measurements $M_{i,n}$ and $M_{i-1,n}$. The centre of this voxel lies a distance $\frac{r_n}{2}\sqrt{3}$ from the origin at polar angle $\Theta_i = \theta_i + \frac{\pi}{6}$. This centre is denoted by $\mathbf{x}_{i,n} = \frac{r_n}{2}\sqrt{3}\big(\cos\Theta_i, \sin\Theta_i\big)$. Note that $\Omega_{i,n}$ is a trapezium with width $\frac{d}{2}\sqrt{3}$ and the parallel sides have lengths $r_n - \frac{d}{2}$ and $r_n + \frac{d}{2}$. Therefore its area is $|\Omega_{i,n}| = \frac{dr_n}{2}\sqrt{3}$.

4.2 Best Estimates

In order to quantify any improvement by applying mass constraints in the computation of velocity estimates one first has to define the best possible single two-dimensional representation of the flow within a voxel. Suppose the two-dimensional estimate $\mathbf{U}_{i,n} = \big(U_{i,n}, W_{i,n}\big)$ for the true water velocity $\mathbf{u} = (u, w)$ in voxel $\Omega_{i,n}$. Now it is stated that the best possible estimate $\mathbf{U}_{i,n}$ minimizes the following error term E:

$$E = \int_{\Omega_{i,n}} \big(\mathbf{u}(x,z) - \mathbf{U}_{i,n}\big)^2 \, dxdz.$$

Its derivative with respect to the estimate $\mathbf{U}_{i,n}$ should be zero, and hence:

$$\begin{aligned} 0 &= \int_{\Omega_{i,n}} \mathbf{u}(x,z)\, dxdz - \int_{\Omega_{i,n}} \mathbf{U}_{i,n}\, dxdz \\ &= \int_{\Omega_{i,n}} \mathbf{u}(x,z)\, dxdz - \mathbf{U}_{i,n}|\Omega_{i,n}|. \end{aligned}$$

Therefore the best possible estimate for the velocity in each voxel is its average velocity:

$$\mathbf{U}_{i,n} = \frac{1}{|\Omega_{i,n}|} \int_{\Omega_{i,n}} \mathbf{u}(x,z)\, dxdz. \tag{4.1}$$

Now expression (4.1) is not in a workable form for the upcoming computations. Thus a stream-function ψ for the underlying flow is again assumed, and so for the best possible estimates one has:

$$\begin{cases} U_{i,n} &= \frac{1}{|\Omega_{i,n}|} \int_{\Omega_{i,n}} \psi_z(x,z)\, dxdz \\ W_{i,n} &= -\frac{1}{|\Omega_{i,n}|} \int_{\Omega_{i,n}} \psi_x(x,z)\, dxdz. \end{cases} \tag{4.2}$$

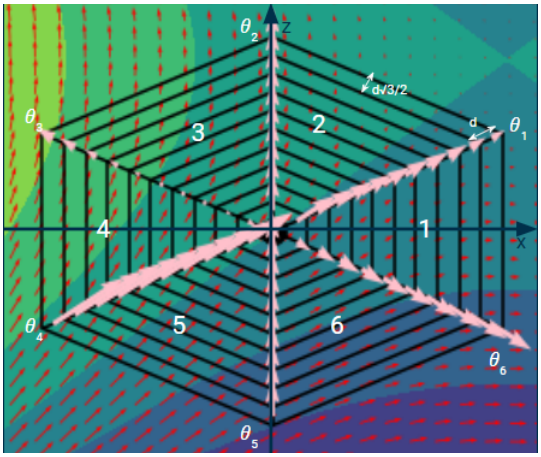

(a) Simulation set up of the buckyball, with radial measurements of the flow (pink), beam angles, cell and voxel sizes indicated. The angular sections are indicated by numbers. Underneath a streamfunction is plotted as a contour, with the associated vectors indicating (u, w) (red, not to scale).

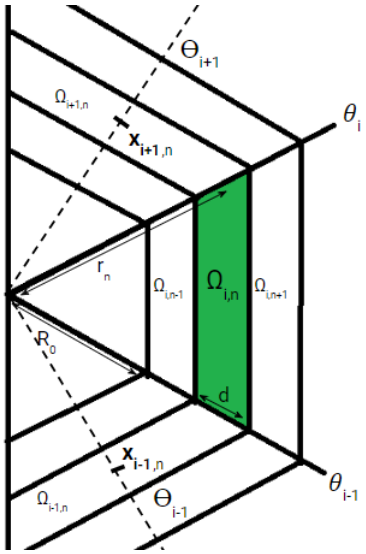

(b) Schematic set up of an angular section, with cell sizes, blanking distance and radial distance indicated, as well as beam angles θ_i and θ_{i-1} and polar angles Θ_{i-1} and Θ_{i+1} through voxel centres $\mathbf{x}_{i-1,n}$ and $\mathbf{x}_{i+1,n}$ respectively.

Figure 4.2: Two-dimensional simulation set up of the buckyball.

Then applying Simpson's rule[1] to approximate these integrals yields

$$\begin{cases} U_{i,n} \approx & \psi_z(\mathbf{x}_{i,n}) + \frac{d^2\sqrt{3}}{24r_n} \\ & \Big(-\cos^2(\Theta_i)\cos(\theta_{i+1})\psi_{xx}(\mathbf{x}_{i,n}) \\ & +\frac{1}{2}(2\cos(\Theta_i) + \sin(\theta_{i+1}) - \sin(3\theta_i))\psi_{xz}(\mathbf{x}_{i,n}) \\ & +\frac{1}{4}(3\sin(\Theta_i) - 4\cos(\theta_{i+1}) + \cos(3\theta_i))\psi_{zz}(\mathbf{x}_{i,n})\Big) \\ W_{i,n} \approx & -\psi_x(\mathbf{x}_{i,n}) + \frac{d^2\sqrt{3}}{24r_n} \\ & \Big(-\sin^2(\Theta_i)\sin(\theta_{i+1})\psi_{zz}(\mathbf{x}_{i,n}) \\ & +\frac{1}{2}(-2\sin(\Theta_i) + \cos(\theta_{i+1}) + \cos(3\theta_i))\psi_{xz}(\mathbf{x}_{i,n}) \\ & +\frac{1}{4}(-3\cos(\Theta_i) - 4\sin(\theta_{i+1}) - \sin(3\theta_i))\psi_{xx}(\mathbf{x}_{i,n})\Big). \end{cases}$$

The complete derivation can be found in Appendix A.1. In this approximation, similar to the analysis done in the previous chapter, it is assumed that third and higher order derivatives of $\psi(x, z)$ -so second and higher order derivatives of the velocities- are negligible compared to the first and second derivatives of $\psi(x, z)$. This assumption is made throughout this chapter. It is also assumed that the width of a voxel is much smaller than its length, which is often the case with ADCPs, so $\frac{d}{r_n} \ll 1$. Thus for the best possible estimates the following approximations are used:

$$\begin{cases} U_{i,n} & \approx \psi_z(\mathbf{x}_{i,n}) \\ W_{i,n} & \approx -\psi_x(\mathbf{x}_{i,n}), \end{cases} \tag{4.3}$$

in other words the best possible estimates for the flow velocities within a voxel are the flow velocities at the voxel's centre.

4.3 Conventional Estimates

Here the estimates $(\hat{u}_{i,n}, \hat{w}_{i,n})$ for each voxel are computed in the conventional way, which means it is assumed that the flow within each voxel is completely constant. From now on $\hat{\cdot}$ indicates an estimator that is calculated in the conventional way. In this way the two-dimensional buckyball becomes six two-beam ADCPs as in section 2.2. So taking constant velocities $(\hat{u}_{i,n}, \hat{w}_{i,n})$ for voxel $\Omega_{i,n}$ would result in the along-beam measurements, i.e. the radial velocities:

$$\begin{cases} M_{i,n} & = \cos(\theta_i)\hat{u}_{i,n} + \sin(\theta_i)\hat{w}_{i,n} \\ M_{i-1,n} & = \cos(\theta_{i-1})\hat{u}_{i,n} + \sin(\theta_{i-1})\hat{w}_{i,n} \end{cases}$$

and rearranging produces the conventional estimates:

$$\begin{cases} \hat{u}_{i,n} & = \frac{2}{\sqrt{3}}\Big(\sin(\theta_i)M_{i-1,n} - \sin(\theta_{i-1})M_{i,n}\Big) \\ \hat{w}_{i,n} & = \frac{2}{\sqrt{3}}\Big(\cos(\theta_{i-1})M_{i,n} - \cos(\theta_i)M_{i-1,n}\Big), \end{cases} \tag{4.4}$$

where pre-factor $\frac{2}{\sqrt{3}}$ arises from $\sin(\theta_i - \theta_{i-1}) = \sqrt{3}/2$. Note that here, and also in the rest of the section, measurements $M_{i,n}$ are equalized to their expectation value i.e. the radial velocities.

4.3.1 Error Analysis of Conventional Estimates

The quality of these conventional estimates can be quantified by comparing them to the best possible estimates (4.2). The error E_C in these estimates is defined as follows:

$$E_{C,\,i,n} = \sqrt{(\hat{u}_{i,n} - U_{i,n})^2 + (\hat{w}_{i,n} - W_{i,n})^2}.$$

Firstly to compute this error the estimates (4.4) are expressed into the true streamfunction ψ, where it is used that the measurements $M_{i,n}$ are the radial velocities at the measurement points $\mathbf{s}_{i,n} = r_n(\cos\theta_i, \sin\theta_i)$. So

$$M_{i,n} = \cos(\theta_i)\psi_z(\mathbf{s}_{i,n}) - \sin(\theta_i)\psi_x(\mathbf{s}_{i,n})$$

and inserting this into (4.4) yields

$$\begin{cases} \hat{u}_{i,n} \approx & \psi_z(\mathbf{x}_{i,n}) + \frac{2}{\sqrt{3}}r_n \\ & \Big[\sin(\theta_{i-1})\sin(\theta_i)(\cos(\theta_i) - \cos(\theta_{i-1}))\psi_{xx}(\mathbf{x}_{i,n}) \\ & -(\sin(\theta_{i-1})\sin(\theta_i)(\cos(\theta_i) - \cos(\theta_{i-1})) + \tfrac{3}{4}\sin(\Theta_i))\psi_{zz}(\mathbf{x}_{i,n}) \\ & +(\sin(\theta_i)\cos(2\theta_{i-1}) - \sin(\theta_{i-1})\cos(2\theta_i) - \tfrac{3}{4}\cos(\Theta_i))\psi_{xz}(\mathbf{x}_{i,n})\Big] \\ \hat{w}_{i,n} \approx & -\psi_z(\mathbf{x}_{i,n}) + \frac{2}{\sqrt{3}}r_n \\ & \Big[\cos(\theta_{i-1})\cos(\theta_i)(\sin(\theta_i) - \sin(\theta_{i-1}))\psi_{zz}(\mathbf{x}_{i,n}) \\ & -(\cos(\theta_{i-1})\cos(\theta_i)(\sin(\theta_i) - \sin(\theta_{i-1})) - \tfrac{3}{4}\cos(\Theta_i))\psi_{xx}(\mathbf{x}_{i,n}) \\ & -(\cos(\theta_i)\cos(2\theta_{i-1}) - \cos(\theta_{i-1})\cos(2\theta_i) - \tfrac{3}{4}\sin(\Theta_i))\psi_{xz}(\mathbf{x}_{i,n})\Big], \end{cases}$$

where again third and higher order derivatives of the streamfunction are neglected. This derivation is done in Appendix A.2. Combining these with the approximate expressions for the best estimators produces an approximation for the error in this conventional method. For simplicity only the error in the first angular section, between the first and sixth beam, is calculated, since one would get similar expressions in the other sections due to the rotational symmetry of the buckyball. Additionally, in this angular section some coefficients multiplying second derivative terms vanish.

$$E_{C,\,1,n} \approx \sqrt{\big(\psi_z(\mathbf{x}_{1,n}) - \frac{r_n}{2\sqrt{3}}\psi_{xz}(\mathbf{x}_{1,n}) - \psi_z(\mathbf{x}_{1,n})\big)^2 + \big(-\psi_x(\mathbf{x}_{1,n}) - \frac{r_n\sqrt{3}}{2}\psi_{zz}(\mathbf{x}_{1,n}) + \psi_x(\mathbf{x}_{1,n})\big)^2}$$

$$= \frac{r_n}{2\sqrt{3}}\sqrt{(\psi_{xz}(\mathbf{x}_{1,n}))^2 + 9(\psi_{zz}(\mathbf{x}_{1,n}))^2}$$
$$= \frac{r_n}{2\sqrt{3}}\sqrt{(w_z(\mathbf{x}_{1,n}))^2 + 9(u_z(\mathbf{x}_{1,n}))^2}.$$

So in each angular section the error in the conventional method is caused by a velocity difference in the long direction of each voxel, where the difference in the radial outward velocity causes nine times the error as the difference in azimuthal velocity.

4.4 Mass Constraints Applied

4.4.1 Mass Conservation Equation

Firstly for each voxel $\Omega_{i,n}$ the mass conservation equation is formulated. Suppose one has velocities $(u_{i,n}, w_{i,n})$ located at the centre $\mathbf{x}_{i,n}$ of voxel $\Omega_{i,n}$. Define $\Sigma_{i,n}$ and $\Phi_{i,n}$ by

$$\Sigma_{i,n} = \frac{1}{2}\big(\cos\Theta_i\big(u_{i,n} + u_{i,n+1}\big) + \sin\Theta_i\big(w_{i,n} + w_{i,n+1}\big)\big)$$
$$\Phi_{i,n} = \frac{1}{2}\big(\cos\theta_i\big(w_{i,n} + w_{i+1,n}\big) - \sin\theta_i\big(u_{i,n} + u_{i+1,n}\big)\big).$$

By linear interpolation $\Sigma_{i,n}$ would be the radial velocity from $\Omega_{i,n}$ to $\Omega_{i,n+1}$ and $\Phi_{i,n}$ the azimuthal velocity from $\Omega_{i,n}$ to $\Omega_{i+1,n}$, see also figure 4.3(a). Demanding mass conservation for voxel $\Omega_{i,n}$ would equate to:

$$\big(r_n - \frac{d}{2}\big)\Sigma_{i,n-1} - \big(r_n + \frac{d}{2}\big)\Sigma_{i,n} + d\Phi_{i-1,n} - d\Phi_{i,n} = 0.$$

This equation can be rewritten as:

$$\begin{aligned}
&\big(r_n - \frac{d}{2}\big)\big(\cos\Theta_i u_{i,n-1} + \sin\Theta_i w_{i,n-1}\big)\\
&+d\big(\cos\theta_{i-1} w_{i-1,n} - \sin\theta_{i-1} u_{i-1,n}\big)\\
&+d\big(\sin\theta_i u_{i+1,n} - \cos\theta_i w_{i+1,n}\big)\\
&-\big(r_n + \frac{d}{2}\big)\big(\cos\Theta_i u_{i,n+1} + \sin\Theta_i w_{i,n+1}\big)\\
&+d\big(\underbrace{\cos\theta_{i-1} - \cos\theta_i - \sin\Theta_i}_{0}\big)w_{i,n} + d\big(\underbrace{\sin\theta_i - \sin\theta_{i-1} - \cos\Theta_i}_{0}\big)u_{i,n}\\
&=0.
\end{aligned} \tag{4.5}$$

In the next subsections an algorithm that implements this mass conservation law will be discussed.

4.4.2 Corrective Algorithm

Initial Idea

Looking at the formulated mass conservation law (4.5) one notices that the contribution of the radial flow $\Sigma_{i,n}$ is roughly a factor r_n/d as large as the contribution of the sideways flow $\Phi_{i,n}$. So if in (4.5) the radial estimates were to be used to correct the azimuthal contributions then the error in these radial estimates would be enlarged by a factor r_n/d. For most to all voxels it holds that $d \ll r_n$, so this error would be enlarged in the correction of the azimuthal contributions. Therefore it was decided to first correct the radial estimates using mass constraints with uncorrected azimuthal estimates, and then use these improved radial estimates to correct the angular estimates. This avoids using any uncorrected radial estimates in calculations.

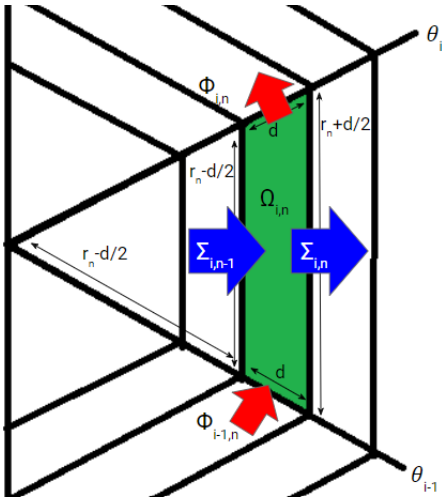

(a) The mass conservation law for voxel $\Omega_{i,n}$ with in blue radial flows $\Sigma_{i,n}$ and $\Sigma_{i,n-1}$ and azimuthal flows $\Phi_{i,n}$ and $\Phi_{i-1,n}$.

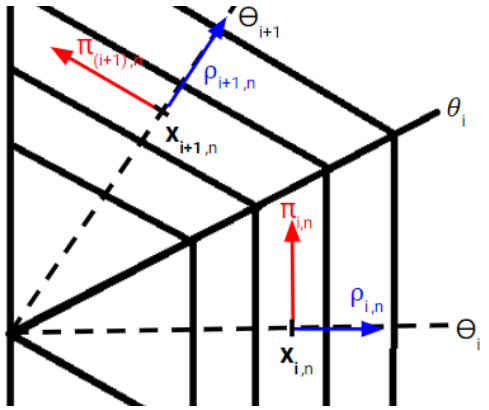

(b) The polar velocities $(\rho_{i,n}, \pi_{i,n})$ at the centre $\mathbf{x}_{i,n}$ of $\Omega_{i,n}$, and similarly for $\Omega_{i+1,n}$. Angles θ_i and Θ_i through the centre are also indicated.

Figure 4.3: Schematic overviews of $\Omega_{i,n}$.

So the estimates need to be presented in a radial and angular direction. Therefore the coordinate system is changed to a polar system. Suppose again velocities $(u_{i,n}, w_{i,n})$ at the centre of $\Omega_{i,n}$. Define

$$\begin{cases} \rho_{i,n} &= \sin\theta_{i+1} u_{i,n} - \cos\theta_{i+1} w_{i,n} \\ \pi_{i,n} &= \cos\Theta_i w_{i,n} - \sin\Theta_i u_{i,n}, \end{cases} \tag{4.6}$$

so $\rho_{i,n}$ and $\pi_{i,n}$ are the radial and azimuthal velocity in the centre $\mathbf{x}_{i,n}$, see also figure 4.3(b). Then the mass constraint (4.5) becomes

$$(r_n - \frac{d}{2})\rho_{i,n-1} - (r_n + \frac{d}{2})\rho_{i,n+1} - \frac{d}{2}(\rho_{i-1,n} + \rho_{i+1,n}) + \frac{d}{2}\sqrt{3}(\pi_{i-1,n} - \pi_{i+1,n}) = 0. \tag{4.7}$$

Radial Correction

Suppose initially for every voxel the estimates $\hat{\rho}_{i,n}$ and $\hat{\pi}_{i,n}$. These are the radial and azimuthal velocity estimates computed with the conventional method. So rewriting (4.4) with (4.6) yields:

$$\begin{cases} \hat{\rho}_{i,n} &= \frac{1}{\sqrt{3}}(M_{i,n} + M_{i-1,n}) \\ \hat{\pi}_{i,n} &= M_{i,n} - M_{i-1,n}, \end{cases} \tag{4.8}$$

where again and also in the rest of this section, measurements $M_{i,n}$ are equalized to their expectation value i.e. the radial velocities.

Then mass constraints (4.7) are applied to these voxel-based estimators by finding new corrected radial estimator $\bar{\rho}_{i,n+1}$ based on the previously corrected estimators $\bar{\rho}_{i,n-1}$, $\bar{\rho}_{i-1,n}$ and $\bar{\rho}_{i+1,n}$ and uncorrected estimates $\hat{\pi}_{i-1,n}$ and $\hat{\pi}_{i+1,n}$. From now on $\bar{\cdot}$ indicates an estimator that is calculated with mass constraints corrections. Inserting these estimators in the mass conservation law (4.7) yields:

$$(r_n - \frac{d}{2})\bar{\rho}_{i,n-1} - (r_n + \frac{d}{2})\bar{\rho}_{i,n+1} - \frac{d}{2}(\bar{\rho}_{i-1,n} + \bar{\rho}_{i+1,n}) + \frac{d}{2}\sqrt{3}(\hat{\pi}_{i-1,n} - \hat{\pi}_{i+1,n}) = 0,$$

and so for the new radial estimator:

$$\bar{\rho}_{i,n+1} = \frac{r_n - d/2}{r_n + d/2}\bar{\rho}_{i,n-1} - \frac{d}{2r_n + d}\big(\bar{\rho}_{i-1,n} + \bar{\rho}_{i+1,n}\big) + \frac{d}{2r_n + d}\sqrt{3}\big(\hat{\pi}_{i-1,n} - \hat{\pi}_{i+1,n}\big). \tag{4.9}$$

This equation does not work for the radial estimates of the two inner rings of voxels, so for these the conventional estimates are taken:

$$\begin{aligned}\bar{\rho}_{i,1} &= \hat{\rho}_{i,1}\\ \bar{\rho}_{i,2} &= \hat{\rho}_{i,2},\end{aligned}$$

which is justified since the inner conventional estimates are the most accurate. So using the already corrected radial estimates from inner rings the radial estimates of outer rings are corrected. This mechanism in equation (4.9) has two advantages. Firstly, errors in $\bar{\rho}_{i\pm1,n}$ and $\hat{\pi}_{i\pm,n}$ are multiplied by $d/(2r_n + d) \ll 1$, so $\bar{\rho}_{i,n+1}$ is as accurate as $\bar{\rho}_{i,n-1}$ since $(r_n - d/2)/(r_n + d/2) \approx 1$. Hence the correction in $\bar{\rho}_{i,n+1}$ mainly depends on measurements along beams i and $i-1$, instead of far off beams $i+1$ and $i-2$. Secondly, estimates in ring $n+1$ are only based on estimates in closer rings. So any inaccurate estimates in the outer rings -where the voxels are larger and so the inter-beam errors too- are ignored. Moreover, the outer measurements are then also ignored, and these measurements would be more inaccurate if geometric beam spreading were included in the simulations.

Azimuthal Correction

Next, the corrected azimuthal velocity estimates $\bar{\pi}_{i,n}$ are determined. Again new notation needs to be introduced. With $\pi_{i_2,n}$ and $\pi_{i_1,n}$ the velocities in the same direction of $\pi_{i,n}$ are denoted but now at the measurement sites $\mathbf{s}_{i,n}$ and $\mathbf{s}_{i-1,n}$ respectively, see figure 4.4(a). To be more precise:

$$\begin{aligned}\pi_{i_2,n} &= \cos\Theta_i w(\mathbf{s}_{i,n}) - \sin\Theta_i u(\mathbf{s}_{i,n})\\ \pi_{i_1,n} &= \cos\Theta_i w(\mathbf{s}_{i-1,n}) - \sin\Theta_i u(\mathbf{s}_{i-1,n}).\end{aligned}$$

Now, the flow is divergence free since mass is conserved and so the following should hold approximately with the corrected estimators:

$$\frac{\pi_{i_2,n} - \pi_{i_1,n}}{r_n} + \frac{(\bar{\rho}_{i,n+1} + \bar{\rho}_{i,n})/2 - (\bar{\rho}_{i,n} + \bar{\rho}_{i,n-1})/2}{d\sqrt{3}/2} = 0 \tag{4.10}$$

which means that the gradient of the flow along the long side of $\Omega_{i,n}$ should add with the gradient of the flow along the short side to zero. Also, the flow along the long side is assumed to be linear, leading to:

$$\bar{\pi}_{i,n} = \frac{\pi_{i_2,n} + \pi_{i_1,n}}{2}. \tag{4.11}$$

Combining equations (4.10) and (4.11) produces

$$\begin{aligned}\bar{\pi}_{i,n} &= \pi_{i_1,n} + \frac{r_n}{2}\Big(\frac{\bar{\rho}_{i,n+1} - \bar{\rho}_{i,n-1}}{d\sqrt{3}}\Big)\\ \pi_{i_2,n} &= \bar{\pi}_{i,n} + \frac{r_n}{2}\Big(\frac{\bar{\rho}_{i,n+1} - \bar{\rho}_{i,n-1}}{d\sqrt{3}}\Big).\end{aligned} \tag{4.12}$$

Now note that at each measurement point $\mathbf{s}_{i,n}$ there are now three different velocities defined, see also figure 4.4(b):

$$\begin{cases} M_{i,n} & = \cos\theta_i u(\mathbf{s}_{i,n}) + \sin\theta_i w(\mathbf{s}_{i,n})\\ \pi_{i_2,n} & = \cos\Theta_i w(\mathbf{s}_{i,n}) - \sin\Theta_i u(\mathbf{s}_{i,n})\\ \pi_{(i+1)_1,n} & = \cos\Theta_{i+1} w(\mathbf{s}_{i,n}) - \sin\Theta_{i+1} u(\mathbf{s}_{i,n}).\end{cases}$$

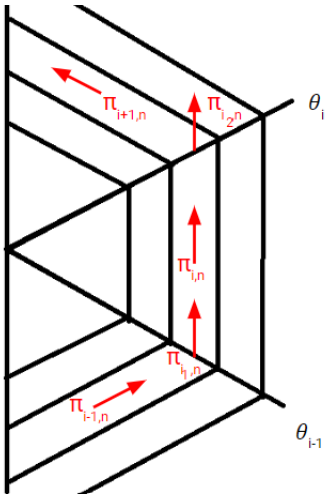

(a) Velocities $\pi_{i,n}$, $\pi_{i-1,n}$ and $\pi_{i+1,n}$ at the centre of their respective voxels with the newly introduced $\pi_{i_1,n}$ and $\pi_{i_2,n}$ indicated at the measurement points at the edges of voxel $\Omega_{i,n}$.

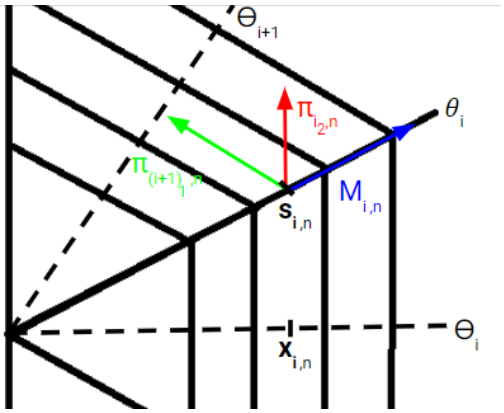

(b) The three different estimators at measuring point $\mathbf{s}_{i,n}$: radial measurement $M_{i,n}$ (blue), and newly defined $\pi_{i_2,n}$ (red) and $\pi_{(i+1)_1,n}$ (green). Voxel centre $\mathbf{x}_{i,n}$, beam angles θ_i and angle Θ_i through the centre are also indicated.

Figure 4.4: Schematic overview of $\Omega_{i,n}$ with relevant estimates for the azimuthal correction.

This is used to derive the following:

$$\begin{aligned}
\pi_{i_2,n} - M_{i,n} &= [\cos\Theta_i - \sin\theta_i]w(\mathbf{s}_{i,n}) - [\sin\Theta_i + \cos\theta_i]u(\mathbf{s}_{i,n}) \\
&= [\cos\left(\Theta_{i+1} - \frac{\pi}{3}\right) - \sin\left(\Theta_{i+1} - \frac{\pi}{6}\right)]w(\mathbf{s}_{i,n}) - [\sin\left(\Theta_{i+1} - \frac{\pi}{3}\right) + \cos\left(\Theta_{i+1} - \frac{\pi}{6}\right)]u(\mathbf{s}_{i,n}) \\
&= \cos\Theta_{i+1}w(\mathbf{s}_{i,n}) - \sin\Theta_{i+1}u(\mathbf{s}_{i,n}) \\
&= \pi_{(i+1)_1,n}.
\end{aligned}$$

Combining this with equations (4.12) yields the iterative equations

$$\begin{aligned}
\bar{\pi}_{i,n} &= \pi_{i_1,n} + \frac{r_n}{2}\left(\frac{\bar{\rho}_{i,n+1} - \bar{\rho}_{i,n-1}}{d\sqrt{3}}\right) \\
&= \pi_{(i-1)_2,n} - M_{i-1,n} + \frac{r_n}{2}\left(\frac{\bar{\rho}_{i,n+1} - \bar{\rho}_{i,n-1}}{d\sqrt{3}}\right) \\
&= \bar{\pi}_{i-1,n} + \frac{r_n}{2d\sqrt{3}}\left(\bar{\rho}_{i,n-1} - \bar{\rho}_{i,n+1} + \bar{\rho}_{i-1,n-1} - \bar{\rho}_{i-1,n+1}\right) - M_{i-1,n}.
\end{aligned} \tag{4.13}$$

It is assumed that $\bar{\pi}_{1,n}$ is some value ω_n, then via reiterating (4.13) one can express all other azimuthal estimators:

$$\begin{aligned}
\bar{\pi}_{1,n} &= \omega_n \\
\bar{\pi}_{2,n} &= \omega_n + \frac{r_n}{2d\sqrt{3}}\left(\bar{\rho}_{2,n-1} - \bar{\rho}_{2,n+1} + \bar{\rho}_{1,n-1} - \bar{\rho}_{1,n+1}\right) - M_{1,n} \\
\bar{\pi}_{3,n} &= \bar{\pi}_{2,n} + \frac{r_n}{2d\sqrt{3}}\left(\bar{\rho}_{3,n-1} - \bar{\rho}_{3,n+1} + \bar{\rho}_{2,n-1} - \bar{\rho}_{2,n+1}\right) - M_{2,n} \\
&= \omega_n + \frac{r_n}{2d\sqrt{3}}\left(\bar{\rho}_{3,n-1} - \bar{\rho}_{3,n+1} + 2\bar{\rho}_{2,n-1} - 2\bar{\rho}_{2,n+1} + \bar{\rho}_{1,n-1} - \bar{\rho}_{1,n+1}\right) - M_{1,n} - M_{2,n} \\
&\vdots
\end{aligned} \tag{4.14}$$

Note that reiterating six times would again yield $\bar{\pi}_{1,n}$, which is indeed the case:

$$\begin{aligned}\bar{\pi}_{1,n} &= \omega_n + \frac{r_n}{d\sqrt{3}} \sum_{i=1}^{6} \left(\bar{\rho}_{i,n-1} - \bar{\rho}_{i,n+1}\right) - \sum_{i=1}^{6} M_{i,n} \\ &= \omega_n\end{aligned}$$

where the last step follows since $\sum_i \bar{\rho}_{i,n} = 0$ and $\sum_i M_{i,n} = 0$. This is due to mass conservation: both sums describe the total flow going into an enclosed hexagon, so both should be zero, see also Appendix A.3. Finally ω_n is determined by fitting the expressions (4.14) to the conventional estimates:

$$\omega_n = \arg\min \sqrt{\sum_{i=1}^{6} (\bar{\pi}_{i,n} - \hat{\pi}_{i,n})^2}. \tag{4.15}$$

This results in:

$$\begin{aligned}\omega_n = &\frac{1}{6}\left(3M_{1,n} + 2M_{2,n} + M_{3,n} - M_{5,n} - 2M_{6,n}\right) \\ &+ \frac{1}{6}\frac{r_n}{d\sqrt{3}}\left(2\bar{\rho}_{6,n-1} - 2\bar{\rho}_{6,n+1} + \bar{\rho}_{5,n-1} - \bar{\rho}_{5,n+1} - \bar{\rho}_{3,n-1} + \bar{\rho}_{3,n+1} - 2\bar{\rho}_{2,n-1} + 2\bar{\rho}_{2,n+1}\right)\end{aligned} \tag{4.16}$$

which is derived in Appendix A.4. With ω_n determined all other azimuthal estimates $\bar{\pi}_{i,n}$ for $1 \leq i \leq 6$ can be determined via the iterative equation (4.13).

Note that this method only works for interior rings n, so for the outer ($n = N$) and inner ring ($n = 1$) the original estimates are used: $\bar{\pi}_{i,1} = \hat{\pi}_{i,1}$ and $\bar{\pi}_{i,N} = \hat{\pi}_{i,N}$.

The advantages of this method to compute $\bar{\pi}_{i,n}$ are that mainly the already corrected estimates $\bar{\rho}_{i,n\pm1}$ are used and that the original estimates $\hat{\pi}_{i,n}$ are not needed. Moreover, in this approach to formulate the iterative equation (4.13) for $\bar{\pi}_{i,n}$ only measurements from the closest beams i and $i \pm 1$ are needed.

Summary

Here a brief recap of the corrective algorithm to compute the conventional estimates is presented. Initially for each voxel one has the conventional estimates $(\hat{u}_{i,n}, \hat{w}_{i,n})$, and rewrites them in polar form $(\hat{\rho}_{i,n}, \hat{\pi}_{i,n})$. Then as a first step the radial estimates are corrected via (4.9), see also figure 4.5(a). With these corrected estimates in the radial direction the gradient in the angular direction can be determined via the continuity equation (divergence-free flow), see (4.10). Using these gradients the iterative equation (4.13) can be formulated that connects all azimuthal estimates within a ring. Using this the corrected estimates are then determined by fitting the expressions from the iterative equation to the conventional azimuthal estimates, see figure 4.5(b). Then the corrected estimates $(\bar{\rho}_{i,n}, \bar{\pi}_{i,n})$ can be rewritten as the Cartesian corrections $(\bar{u}_{i,n}, \bar{w}_{i,n})$ via

$$\begin{cases} \bar{u}_{i,n} &= \cos\Theta_i \bar{\rho}_{i,n} + \cos\theta_{i+1} \bar{\pi}_{i,n} \\ \bar{w}_{i,n} &= \sin\Theta_i \bar{\rho}_{i,n} + \sin\theta_{i+1} \bar{\pi}_{i,n}. \end{cases}$$

4.4.3 Error Analysis of Corrected Estimates

The formulation of an error term for the corrected estimates is rather difficult, since a corrected estimate -especially those at the outer edges- (in)directly depends on a multitude of measurements. Therefore only a crude approximation of the error will be constructed here. The error of the corrected estimates is defined in a similar manner as before:

$$E_{N\,i,n} = \sqrt{(\bar{u}_{i,n} - U_{i,n})^2 + (\hat{w}_{i,n} - W_{i,n})^2}$$

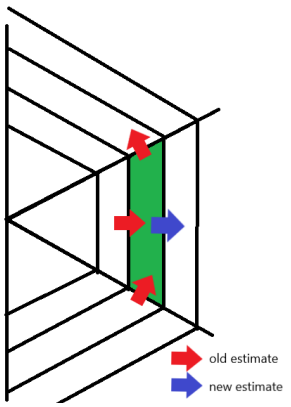

(a) Step 1: correcting the radial estimates from the inner to the outer ring.

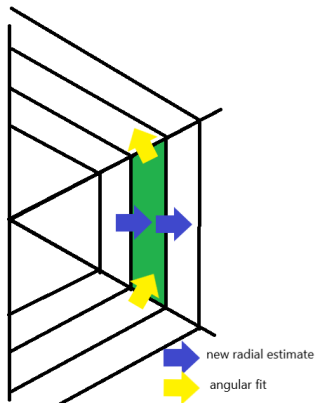

(b) Step 2: correcting the azimuthal estimates with a linear fit.

Figure 4.5: Steps of the corrective algorithm, where mass conservation of the green voxel is demanded.

$$\approx \sqrt{(\bar{u}_{i,n} - \psi_z(\mathbf{x}_{i,n}))^2 + (\hat{w}_{i,n} + \psi_x(\mathbf{x}_{i,n})^2}$$

Again only angular section 1 is considered for simplicity. The errors in $(\bar{\rho}_{i,n}, \bar{\pi}_{i,n})$ are denoted by $(\epsilon_{i,n}, \eta_{i,n})$. In appendices A.5 and A.6 the following expressions are derived:

$$\begin{aligned}
\epsilon_{1,n} &= \bar{\rho}_{1,n} - \psi_z(\mathbf{x}_{1,n}) \\
&= -r_n/2\psi_{xz}(\mathbf{x}_{1,n}) \\
\eta_{1,n} &= \bar{\pi}_{1,n} + \psi_x(\mathbf{x}_{1,n}) \\
&= \frac{r_n}{\sqrt{3}}\psi_{xx}(\mathbf{x}_{1,n}) + \frac{r_n}{2\sqrt{3}}\psi_{zz}(\mathbf{x}_{1,n}).
\end{aligned}$$

Combining the expressions for $\epsilon_{1,n}$ and $\eta_{1,n}$ to formulate the error $E_{N,\,1,n}$ in the new estimates $(\bar{u}_{1,n}, \bar{w}_{1,n})$:

$$\begin{aligned}
E_{N,\,1,n} &\approx \sqrt{\epsilon_{1,n}^2 + \eta_{1,n}^2} \\
&= \frac{r_n}{2\sqrt{3}}\sqrt{3\psi_{xz}(\mathbf{x}_{1,n})^2 + (2\psi_{xx}(\mathbf{x}_{1,n}) + \psi_{zz}(\mathbf{x}_{1,n}))^2} \\
&= \frac{r_n}{2\sqrt{3}}\sqrt{3w_z(\mathbf{x}_{1,n})^2 + (u_z(\mathbf{x}_{1,n}) - 2w_x(\mathbf{x}_{1,n}))^2},
\end{aligned}$$

and again by using the rotational symmetry of the buckyball a similar expressions can be obtained for the other angular sections.

4.5 Results: Processed Buckyball-data

Comparing the application of mass constraints with the conventional method can be done analytically by comparing $E_{C,\,1,n}$ and $E_{N,\,1,n}$. Those are:

$$\begin{aligned}
\left(\frac{E_{C,\,1,n}}{r_n}\right)^2 &= \frac{w_z(\mathbf{x}_{1,n})^2}{12} + \frac{3u_z(\mathbf{x}_{1,n})^2}{4} \\
\left(\frac{E_{N,\,1,n}}{r_n}\right)^2 &= \frac{w_z(\mathbf{x}_{1,n})^2}{4} + \frac{u_z(\mathbf{x}_{1,n})^2}{12} - \frac{2u_z(\mathbf{x}_{1,n})w_x(\mathbf{x}_{1,n})}{3} + \frac{w_x(\mathbf{x}_{1,n})^2}{3}
\end{aligned}$$

which indicate that there are some instances in which applying mass constraints worsen the estimators, depending on the local flow. This is also observed in the simulations. In both cases the error grows linearly with distance r_n, which is inevitable since the distance between the measurement points and the voxel centres grows linearly with r_n. Note that for both methods the errors vanish when the homogeneity assumption holds.

Next, three simulation results are presented. These three results are representative for the other simulated results. The following parameters are used during the simulations: a plane $(x, z) \in [-L, L]^2$ where $L = 100$, and cell properties $R_0 = 10$, $d = 4$ and $N = 20$. The number of cells is chosen such that the computation time of the algorithm is not too long. The cell size d is picked such that the illustrations are clear, and then blanking distance R_0 is taken to be $2 - 3$ times larger than d, as is common with actual transducers. Furthermore, as discussed before, each measurement $M_{i,n}$ has a 2% error. All simulation parameters are dimensionless, since the goal is to show that the mass constraints increase accuracy of the estimates compared to the conventional method: the exact scale of the flows considered are not relevant The results are shown in figures 4.6, 4.7 and 4.8. In all simulations a streamfunction ψ is used that has no third or higher order derivatives, as used in the approximations. In an actual experimental set up this would mean that the measurement area needs to be small enough such that the flow is approximately quadratic. In each figure the streamfunction and velocities are illustrated in the top left figure, while in the top right figure the relative change in the error is visualized. The change in relative error in voxel $\Omega_{i,n}$ is computed as $(E_{C,\,i,n} - E_{N,\,i,n})/||\mathbf{U}_{i,n}||_2$. In the bottom left figure the relative error $E_{C,\,i,n}/||\mathbf{U}_{i,n}||_2$ in the conventional estimates is shown, and in the bottom right figure the same for the corrected estimates by computing $E_{N,\,i,n}/||\mathbf{U}_{i,n}||_2$.

The results in figures 4.6 represent cases in which the corrective algorithm improves the estimates in almost all voxels. Characteristic for cases like figure 4.6 is that the algorithm barely improves the estimates for voxels lying in two opposing angular sections, in this case sections 2 and 5. This is because the conventional method already performs quite good in these sections, as can be seen in figure(c), with a relative error of roughly $10\% - 20\%$. So the algorithm hardly improves the estimates in these two sections. In the other sections where the conventional method does not perform that well, the algorithm reduces the proportional error by up to 64 percentage points in this specific case. Also noteworthy is the difference in relative errors across voxels between the methods: the corrected estimates have in each voxel roughly the same error. The conventional estimates have a voxel-averaged relative error of 0.218, and corresponding variance 0.019, which is lowered to 0.035 and 0.0006 respectively by the corrected method. So not only do the mass constraints lower the overall error, but they also decrease the difference in accuracy between voxels.

In figure 4.7 a case is depicted where the conventional method already performs near-perfect in two angular sections. For velocity field $(u(x, z), w(x, z)) = (0, -5x - \frac{x+100}{50})$, which is dominant in the vertical direction, the conventional errors $E_{C\,1,n}$ and $E_{C\,4,n}$ almost disappear, were it not for the measurement errors. In these angular sections the dominant vertical flow is in the along-voxel direction. Here the conventional method performs well, and the mass constraints actually worsen the estimates in these sections, by up to 16 points. However, in the other four angular sections the conventional method has errors up to 20%, and here the corrected method causes improvements. All in all, the voxel-averaged error of the standard method is 6.9%, and mass constraints slightly reduce that to 6.5%. But also here the difference across voxels reduces: the variance in relative error between voxels drops from 0.0031 to 0.0011.

Lastly, figure 4.8 represents a set of cases, where the algorithm only improves the estimates in two opposing angular sections. Here the conventional method fails in the angular sections 1 and 4 lying on the $x-$axis, and produces quite accurate estimates in the other sections. Again the algorithm improves the worst conventional estimates, but also worsens the best estimates. In some voxels the accuracy increases by 30 percentage points, but in others it decreases by up to 20 percentage points. By using mass constraints nearby estimates are used to correct other estimates, and by doing this the error seems to disperse among the voxels. In this specific case the voxel-averaged error barely decreased from 16.4% to 15.6%, but the voxel-based variance of the relative error went from 0.018 to 0.0058. So by applying the algorithm the errors in the estimates became more uniform among the voxels. One can

see in figure 4.8(d): with mass constraints every voxel produces roughly equally accurate estimates.

4.6 Conclusion on Mass Constraints with Buckyball

In many simulations it was shown that applying mass constraints improve the estimates in almost all voxels, but there were also cases were mass constraints worsened the estimates in some voxels. Overall the average accuracy increased by demanding mass conservation in each voxel. Hence mass constraints seem also in this case a promising addition to the standard beam-to-current method.

In these specific cases, in which this method actually worsens the original estimates, the original estimation technique already produces accurate estimates in some areas of the buckyball measurement area, while in others the homogeneity assumption fails and the result is inaccurate estimates. The corrective algorithm uses nearby estimates to correct other estimates, and so inaccurate estimates are used to correct accurate estimates and vice versa. Therefore the best original estimates lose accuracy, while the worst estimates see an increase in accuracy. As a consequence the difference in quality between the corrected estimates had decreased: in each voxel the estimates are equally accurate. In order to distinguish in which areas of the buckyball measurement area the algorithm might worsen the estimates it needs to be assessed where the conventional method might perform well by for example knowing a dominant flow direction. So an analysis based on the local conditions needs to be made to determine the areas where the homogeneity conditions for each voxel hold quite well. This way for some voxels the conventional method is used, while for the remaining the corrections can be applied.

The error analysis of the conventional method gave insight in when this method is accurate, and could be of use here. The error analysis of the corrected method is not as useful, since in this method an estimate depends on multiple other estimates and measurements, and so a clear analytical expression is hard to obtain. The analysis did however show that just like in the original method the errors grow linearly with distance, and a decrease in errors for the radial estimates.

As a point of discussion the simulation environment needs to be mentioned. As discussed before, the choice of the measurement error model was made based on simplicity and not necessarily realism. So to conclude more convincingly whether mass constraints also have benefit a more realistic simulation for synthetic buckyball data is needed. An easy extension would be to simulate a three-dimensional buckyball. In this case a three-dimensional variant of the streamfunction is needed, where a Helmholtz decomposition can be of use. Even more helpful would be actual raw buckyball data, in which case a similar and more convincing approach as in chapter 3 can be done.

Lastly, the goal of this chapter was to illustrate that also in the buckyball set up mass constraints have a place. It was shown that in most simulations this is the case. For both the buckyball and the common configurations higher order derivatives of the flow need to be neglected. With these results in mind it is attempted in the next chapter to use the buckyball with mass constraints for measuring internal waves.

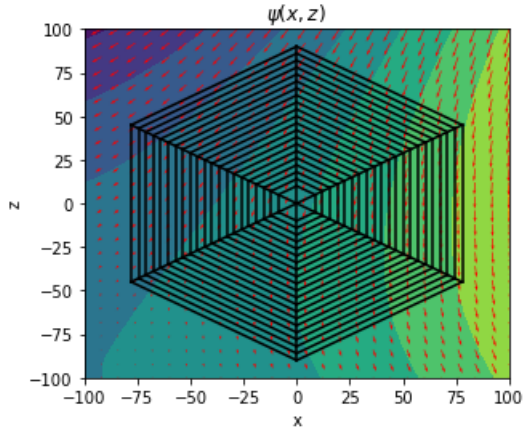

(a) Streamfunction $\psi(x, z)$, where vectors indicate $(u(x, z), w(x, z))$.

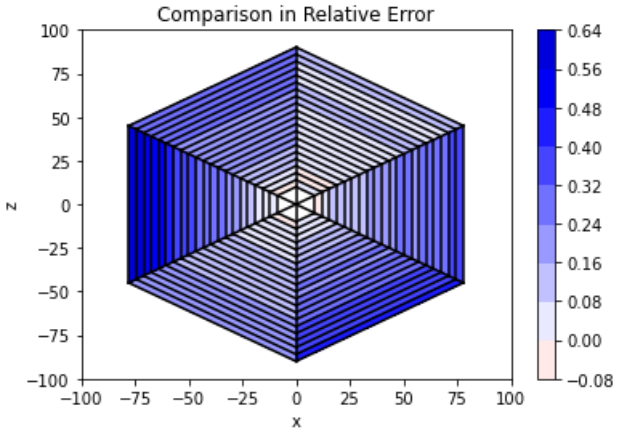

(b) Change in relative error per voxel by applying mass constraints - mass constraints improve the estimates almost everywhere.

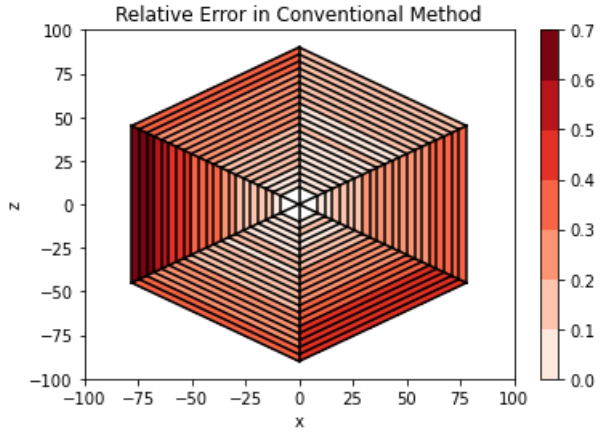

(c) Relative error in the conventional estimates per voxel.

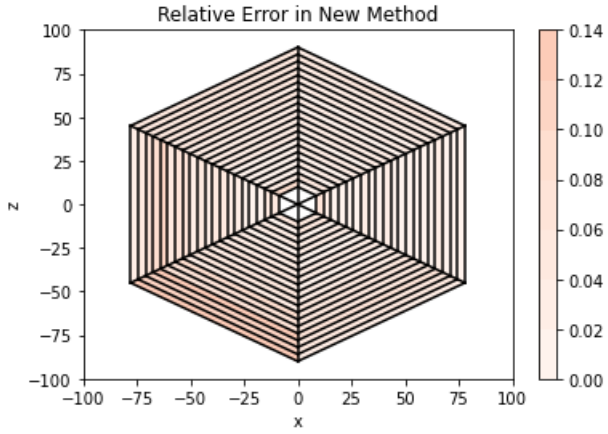

(d) Relative error in the corrected estimates per voxel.

Figure 4.6: Streamfunction $\psi(x, z) = 2(x + 100)(z + 100) + 2((x + 100)^2 - (z + 100)^2) + 2x$, where conventional estimates have a voxel-averaged error of 21.8%, and with mass constraints 3.5%.

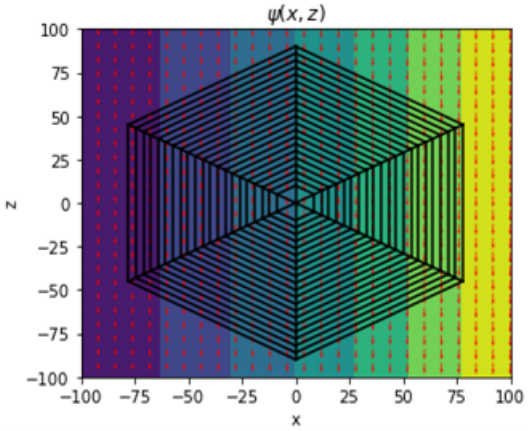

(a) Streamfunction $\psi(x, z)$, where vectors indicate $(u(x, z), w(x, z))$.

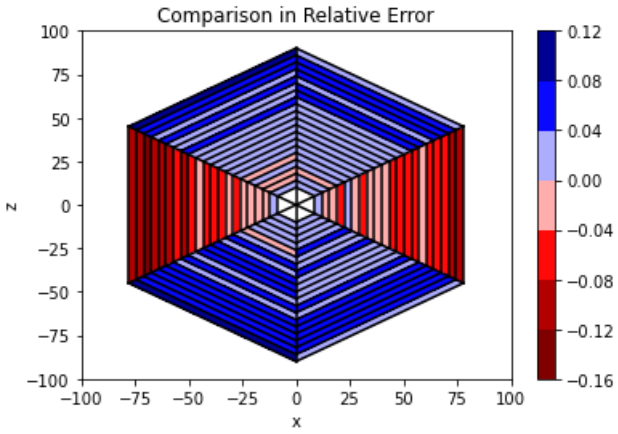

(b) Change in relative error per voxel by applying mass constraints - mass constraints improve the estimates in angular sections 2,3,5 and 6, but worsen them in 1 and 4.

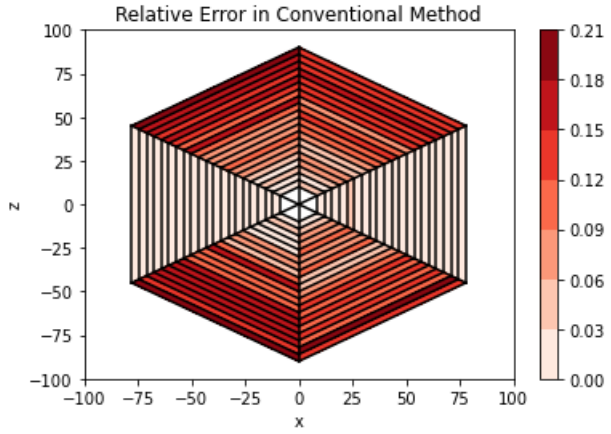

(c) Relative error in the conventional estimates per voxel.

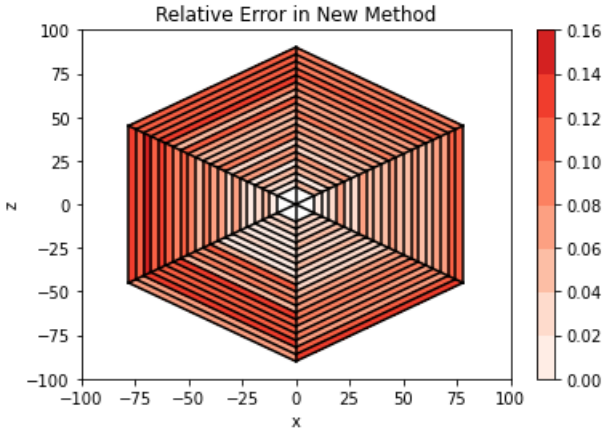

(d) Relative error in the corrected estimates per voxel.

Figure 4.7: Streamfunction $\psi(x, z) = 5(x + 100) + \frac{1}{100}(x + 100)^2$, where conventional estimates have a voxel-averaged error of 6.9%, and with mass constraints 6.5%.

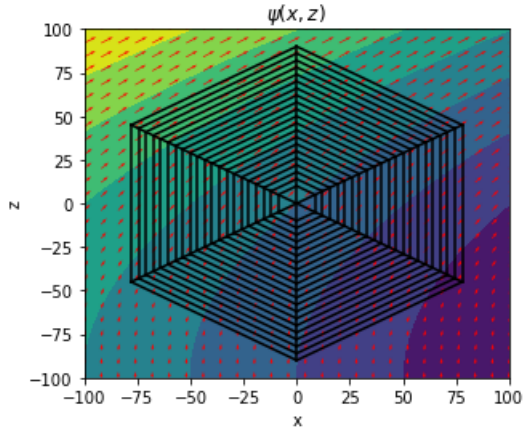

(a) Streamfunction $\psi(x, z)$, where vectors indicate $(u(x, z), w(x, z))$.

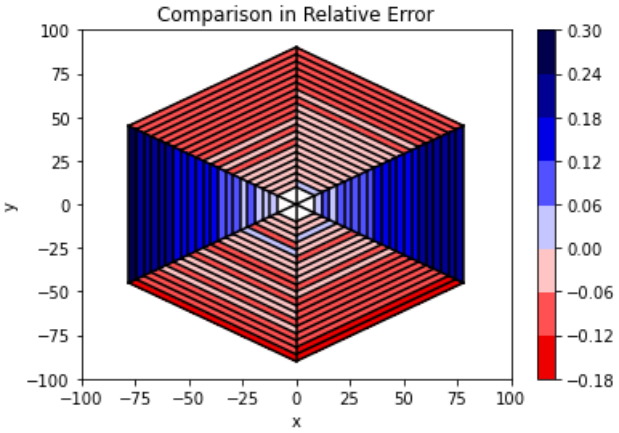

(b) Change in relative error per voxel by applying mass constraints - mass constraints improve the estimates only in sections 1 and 4.

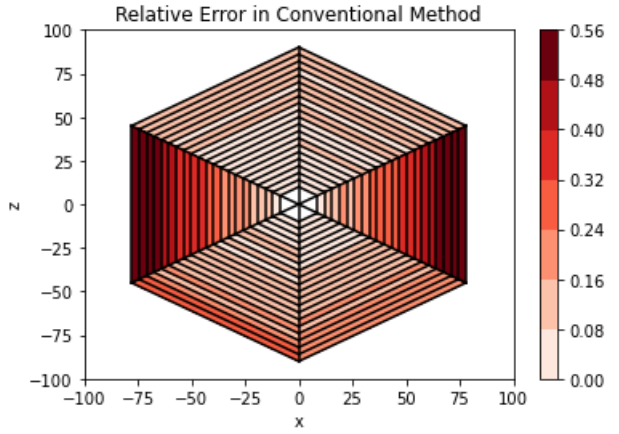

(c) Relative error in the conventional estimates per voxel.

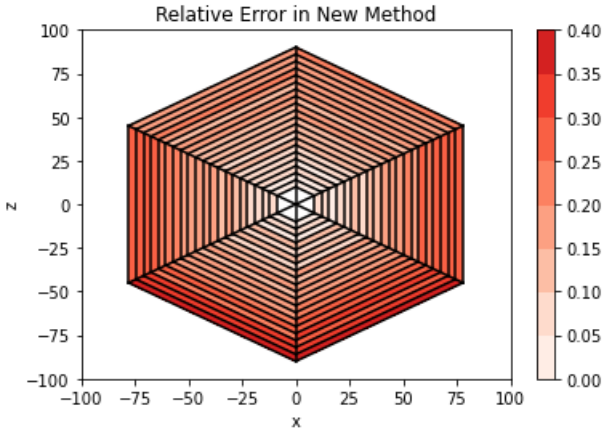

(d) Relative error in the corrected estimates per voxel.

Figure 4.8: Streamfunction $\psi(x, z) = -5((x + 100)^2 - (z + 100)^2) + 5x + 5z + 5x^2$, where conventional estimates have a voxel-averaged error of 16.4%, and with mass constraints 15.6%.

Chapter 5

The Buckyball and Internal Waves

Here the feasibility of the buckyball is examined by testing its capability to measure the shearing motion of internal waves. First, internal waves are introduced, and then the current methods and their disadvantages to measure internal waves using conventional ADCPs are discussed. Next, several methods to capture internal waves using the buckyball are introduced, and their results are discussed.

5.1 Internal Waves

Internal waves are gravity waves occurring in the interior of a fluid. They exist in a stably stratified fluid where lighter layers are above the heavier ones. The physics of these waves is similar to the one of surface waves: an oscillating displacement of a pycnocline around the equilibrium. An internal wave in a lab setting is illustrated in figure 5.1: an internal wave generated by an oscillating plate is travelling through the fluid. This figure illustrates the characteristic aspects of an internal wave: it is a bundle shooting obliquely through the fluid. Depending on the stratification of the fluid the bundle travels at an angle with the vertical: in a non-stratified fluid the bundle travels horizontally, while in a uniformly stratified fluid the bundle travels at an angle. Within the bundle itself the velocity is described by a wave, as indicated by the arrows in figure 5.1. The particle velocity and energy of the wave travel along the bundle, while the phase travels in the cross-bundle direction. An internal wave needs a source: in the experimental set up it was an oscillating plate, while in the ocean it can be storms or tides. In the ocean itself the internal waves can bounce off the surface or sea bed, and so bathymetric features like shelf edges or underwater hills can amplify and direct internal waves[12]. As nice overviews of the physics of internal waves several lecture notes are available [11][26].

Internal waves take place throughout the world's oceans[18], and are therefore relevant for a number of scientific and engineering fields. Internal waves transport energy, heat and nutrients to the deeper parts of the oceans to help sustain life there[31]. There are suggestions that the pycnocline disturbance caused by large internal waves have sunk multiple submarines[37], and that these waves can damage offshore drilling equipment[19]. It is therefore important to accurately measure internal waves. Relevant wave parameters are the velocity and propagation direction of the wave, as well as its width and the wave length in the cross-beam direction.

5.1.1 Observing Internal Waves

There are several ways to measure internal waves in the ocean. One way is using several moored sensitive temperature sensors[15], or using a ship-mounted ADCP[12]. However, here the main focus is on measuring internal wave properties using a single moored ADCP. This would also be the cheapest option.

As touched upon earlier the standard algorithm (3.2) to transform beam measurements to current estimates for a standard ADCP relies on the homogeneity assumption. This condition may be violated

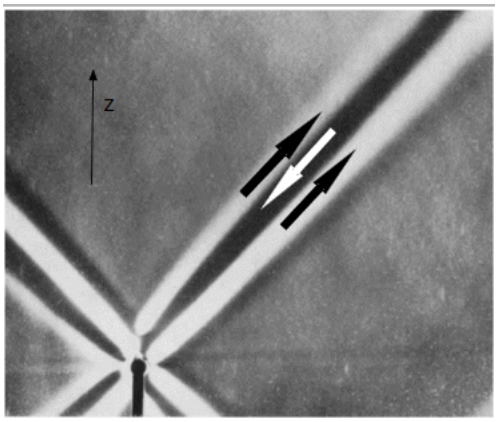

Figure 5.1: Schlieren photograph from [41] of an internal wave, where the arrows indicate flow direction. The source of the wave is an oscillating beam, from which four wave beams in total originate.

when an internal wave passes through the measurement area, and in this case high error velocities can occur. Scotti et al.(2005) introduced a modification to the standard algorithm in order to still measure a passing internal wave using a single ADCP. It was assumed that when an internal wave passed the beams of a moored ADCP, it will cause a significant increase in the intensity of the returning echos. The time delay between the spikes in backscatter intensity for the different beams provides the propagation speed of the passing wave, where it is assumed that the internal wave travels horizontally. This last assumption holds in case of a surface or inter-facial wave. Using this speed a model of a passing internal wave -with the propagation direction as unknown parameter- was taken and fitted to the beam data such that the error velocity, mentioned in section 2.2, was minimized. This was applied to raw ADCP-data in the Massachusetts Bay, a shelf sea. The results were verified by measuring the same waves with an array of different instruments. It showed that this technique could produce the propagation speed and direction of the passing internal waves reliably.

This method was improved upon by Chang et al.(2011) by including background flow and vertical displacement into the fit to the internal wave model. This method was applied to measurements from a single moored ADCP in the South-China Sea and yielded useful estimates of vertical displacement, propagation direction and speed of internal waves. Using this very same method Endoh et al.(2022) were able to again measure these wave properties, but now also the second-order structure within the bundle of internal waves was determined. It needs to be noted that here two moored ADCPs in the South-China Sea were used.

The method introduced by Scotti et al.(2005) and improved by Chang et al.(2011) has its disadvantages. Firstly, the fit of the internal wave model to the beams can only be done when the horizontal length scale is small and the signal remains coherent for the time it takes the wave to pass through the ADCP beam array, in other words there needs to be significant difference between beam measurements within a measuring interval in order to detect a passing wave. Secondly, the signals in the backscatter intensity need to be large enough to estimate the passage of time of the wave front between beams, so mainly large-amplitude internal waves are suitable. Also, the modulation in backscatter intensity could also be due to for example turbulence or zooplankton moving about[9]. And thirdly, in all mentioned research the internal waves considered were all travelling horizontally. It was not discussed why only internal waves moving along interfaces were considered, although these are the most relevant to the off-shore industry. Moreover, if a wave travelling at an angle with the vertical hits the beam array of a moored ADCP, then it is likely that one of the ADCP beams is hit nearly perpendicular by the wave bundle, which would not produce a significant measurement by that beam.

The buckyball configuration might be able to solve these problems partially. Since the buckyball has multiple beams directed in all directions it will observe a larger area (or volume) than a conventional

ADCP, and hence the first problem is partially helped. The second problem of needing a clear signal in backscatter intensity arises because the propagation speed of the wave is needed before the fit to the conventional ADCP-data is made. Now, with the buckyball the wave front will likely strike more beams than in case of a regular set up, and so the propagation speed can be included in the fit to the raw data. And the third problem may also be partially solved, since by hitting more beams it is also likelier to hit more beams at a non-perpendicular angle.

5.2 Simulation Set Up

The following model is used to generate a standard two-dimensional internal wave[11, Ch 6]:

$$\begin{aligned} &\begin{cases} u(x,z) &= V\ \exp\left(\xi/l\right)^2 \cos(k\xi) \\ w(x,z) &= \mu V\ \exp\left(\xi/l\right)^2 \cos(k\xi) \end{cases} \\ &\text{where } \xi = \mu x - z + z_0 \\ &\quad \text{and } \mu = \tan(\varphi) \end{aligned} \tag{5.1}$$

where V the velocity amplitude, ξ the across-bundle coordinate, μ follows from φ which is the angle of the bundle with the horizontal, z_0 is where the centre of the bundle hits the vertical axis, l is the typical width of the bundle and k the wave number. The resulting wave is visualized in figure 5.2(a), and next to it the simulation set up from the previous chapter with the 2% measurement error. So in figure 5.2(a) a bundle whose shape is Gaussian, shoots through the basin and inside the bundle the flow oscillates with wave number k. The phase moves in the direction of increasing ξ.

Now, this simulation environment has some weaker points, especially compared to the non-linear internal wave models used to create synthetic ADCP-data in literature[3][30][34]. However, all those models create horizontally travelling waves, and an extra demand here is a wave travelling at an angle, so the cited models were not copied. These models did though include a temporal component, whereas the model here has not. This is done for simplicity reasons, and the synthetic data presented here to the buckyball would be realistic if the passing internal wave is wide enough to stretch across the whole measurement area, or if the beam transformation step from Scotti et al.(2005) has already been performed. The model can however be easily extended to include this temporal component by including a frequency term and time in the cosine.

In figure 5.2(b) the simulation set up is visualized: a typical internal wave beam striking several beams of the two-dimensional buckyball. Note that in the model no background flow is generated, although it can have a large impact on the measurement of the wave parameters[3][30][36]. The reasoning behind this is that the background flow can simultaneously be determined by the non-stricken beams of the buckyball via the conventional method, i.e. the bottom right beams in figure 5.2(b). So the raw data from the stricken beams can be corrected with this background flow, and so it is as if a wave without background flow is measured.

5.3 Methods

5.3.1 Abandoned Approaches

Initially it was attempted to reconstruct the internal wave from the measurements by using the original discrete approach: the measurement area is divided into voxels and for each voxel a two-dimensional velocity estimate is made. The two methods from chapter 4 were applied: both could yield accurate estimates if the flow had no significant derivatives, and the corrected method can partially compensate the error introduced by a first order derivative. However both failed: the conventional method as well as adding mass constraints cannot produce accurate estimates for the internal wave since the wave contains significant second or higher order derivatives of the velocities.

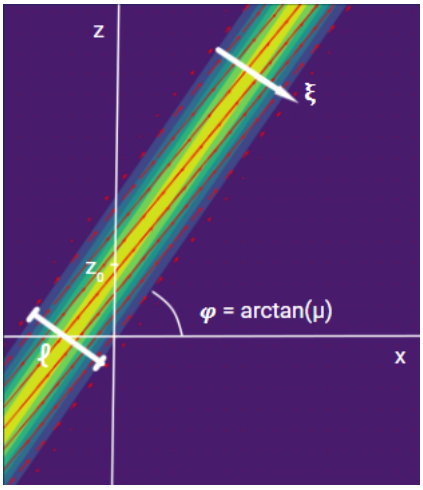

(a) $u(x, z)$ of generated internal wave, with parameters denoted, and vectors indicating $(u(x, z), w(x, z))$.

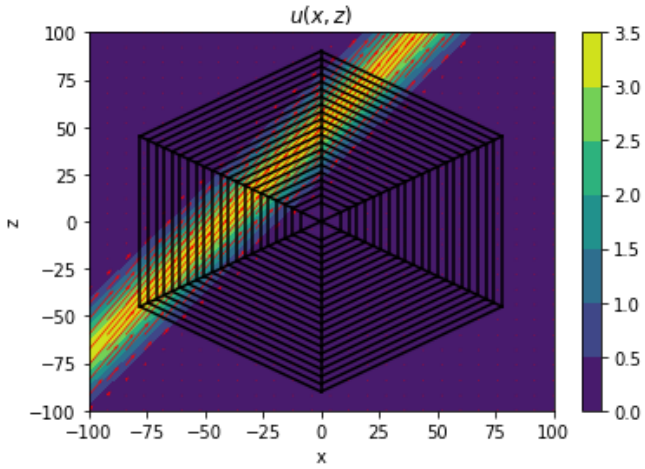

(b) Simulation set up with the generated internal wave, with buckyball parameters $N = 20$, $d = 4$ and $R_0 = 10$.

Figure 5.2: Generated internal wave with parameters $V = 5$, $\phi = 50°$, $z_0 = 50$, $l = 20$ and $k = 0.0025$ in basin $(x, z) \in [-100, 100]^2$.

Next a continuous approach was attempted. The standard procedure of dividing the measurement area into voxels was abandoned, and it was attempted to estimate the flow field in a continuous way instead of using a discrete set of voxel-based estimates. It is assumed that the unknown streamfunction can be written as linear combination of some basis functions. So in other words it is assumed that one can write:

$$\psi(x, z) = \sum_j c_j f_j(x, z)$$

with basis functions f_j and coefficient c_j. These coefficients can be determined with the measurements:

$$\begin{aligned} M_{i,n} &= \cos\theta_i \psi_z(\mathbf{s}_{i,n}) - \sin\theta_i \psi_x(\mathbf{s}_{i,n}) \\ &= \sum_j c_j \big(\cos\theta_i \frac{\partial f_j}{\partial z}(\mathbf{s}_{i,n}) - \sin\theta_i \frac{\partial f_j}{\partial x}(\mathbf{s}_{i,n}) \big) \end{aligned}$$

which yields $6N$ equations for the coefficients c_j. Note that mass conservation is implicitly enforced by assuming that the measurements all follow from an underlying streamfunction.

The first set of basis functions are Bessel functions, and the following is in essence a Fourier-Bessel transform[6][10][20]. This approach was chosen since it is the two-dimensional Fourier transform in polar coordinates, and the measurements are regularly spaced in this coordinate system. Note that in this polar coordinate system (r, θ) are radius and polar angle, (v_r, v_θ) are the radial and azimuthal velocity which follow from a streamfunction $\psi(r, \theta)$, where $(v_r, v_\theta) = (\frac{1}{r}\psi_\theta, -\psi_r)$. It is assumed that:

$$\psi(r, \theta) = \sum_{q=1}^{Q} \sum_{p=0}^{P} \Big(A_{pq} \cos(p\theta) + B_{pq} \sin(p\theta) \Big) J_p\big(\frac{\alpha_{pq}}{L} r\big)$$

where

A_{pq}, B_{pq} are real coefficients

J_p is the p^{th} Bessel function of the first kind with $p \geq 0$

α_{pq} is the q^{th} positive root of $J_p with q \geq 1$

and L is the radius of the disk domain that is considered. Note that the radial velocity $v_r(r,\theta) = \frac{1}{r}\psi_\theta(r,\theta)$ is always zero at the edge of the domain $r = L$, so with these basis functions there are some restrictions. Here $L = r_N + d/2$ is taken such that the farthest echoes are just included in the domain considered. Also B_{pq} are zero for $p = 0$, since their values do not matter in the computation of ψ.

Along Bessel functions for the radial basis functions also Zernike polynomials are tried. Zernike polynomials are often used in optics, and might therefore also be useful here. They were chosen as alternative to the Bessel functions, since these do not need to be zero at the edge of the disk domain. So with this so-called Fourier-Zernike Transform[10] a non-zero radial velocity at the edge can be reproduced. The streamfunction is now written as:

$$\psi(r,\theta) = \sum_{q=1}^{Q}\sum_{p=0}^{P}\Big(A_{pq}\cos(p\theta) + B_{pq}\sin(p\theta)\Big)R_q^p\big(\frac{r}{L}\big)$$

where

A_{pq}, B_{pq} are real coefficients

R_q^p is the radial part of the Zernike polynomial
of radial degree q and azimuthal degree p with $q \geq p \geq 0$

$\cos(p\theta)R_q^p$ is the even Zernike polynomial $Z_q^p(r,\theta)$

$\sin(p\theta)R_q^p$ is the uneven Zernike polynomial $Z_q^{-p}(r,\theta)$

and again $L = r_N + d/2$ is the radius of the disk domain that is considered, but -as mentioned- unlike before the radial velocity need not be zero at the edge, and again B_{pq} are zero for $p = 0$. The Zernike polynomial Z_0^0 is omitted, since this is a constant function, and hence not relevant for a streamfunction.

The derivation of the coefficients in both these transforms is given in Appendix B.1. Both sets of basis functions are orthogonal which simplifies the determination of the coefficients. Also in figure 5.3 a scope of the different basis functions is given. Although with the Fourier-Bessel as with the Fourier-Zernike Transform the underlying streamfunction may now contain higher order derivatives, the results still yielded an inaccurate figure of the internal wave input. The number of coefficients in the transformation were not enough to reproduce the wave, and hence extract the relevant parameters.

5.3.2 Fit to the Wave Model

Instead of trying to reproduce an accurate image of the measurement area now a fit of an internal wave is done to the measurements in order to compute the parameters directly [30][34]. If an internal wave were to pass through the area of the buckyball then one beam would report a burst of water moving towards the buckyball, and another would report a burst moving away, see figure 5.2(b). In such a case one could presume that an internal wave passed through, although similar signals can also be produced by turbulence[34]. So assuming an internal wave passed through, the model (5.1) is fitted to the measurement data.

Based on an internal wave, (5.1), a measurement, i.e. the radial velocity at distance r_n and angle θ_i, should be:

$$\cos\theta_i u(\mathbf{s}_{i,n}) + \sin\theta_i w(\mathbf{s}_{i,n}) = \big(\cos\theta_i + \mu\sin\theta_i\big)V\,\exp\big(-(\xi_{i,n}/l)^2\big)\,\cos(k\xi_{i,n})$$
$$\text{where } \xi_{i,n} = \mu r_n\cos\theta_i - r_n\sin\theta_i + z_0$$

and so a cost function J can be defined as:

$$J:\ (V,\mu,l,z_0,k) \mapsto \sum_{i=1}^{6}\sum_{n=1}^{N}\Big(\big(\cos\theta_i + \mu\sin\theta_i\big)V\,\exp\big(-(\xi_{i,n}/l)^2\big)\,\cos(k\xi_{i,n}) - M_{i,n}\Big)^2.$$

An estimate $\tilde{\mathbf{u}}$ for the wave parameters $\mathbf{u} = (V,\mu,l,z_0,k)$, see figure 5.2(a), minimizes this cost function. Initially it was tried to approximate $\tilde{\mathbf{u}}$ using Newton's Algorithm[1], but here the algorithm

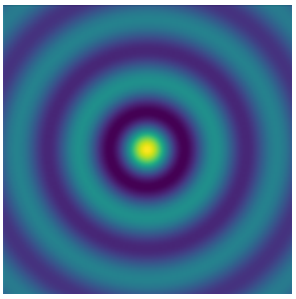

(a) Fourier-Bessel function $J_0(\alpha_{05}r)$.

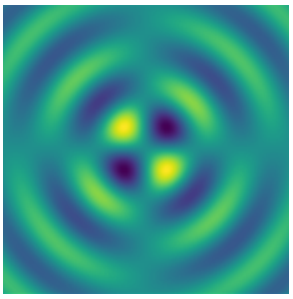

(b) Fourier-Bessel function $J_2(\alpha_{24}r)\sin(2\theta)$.

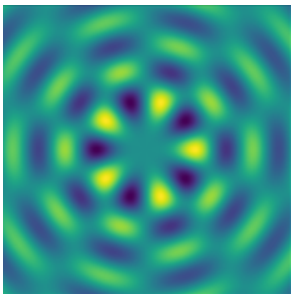

(c) Fourier-Bessel function $J_5(\alpha_{54}r)\cos(5\theta)$.

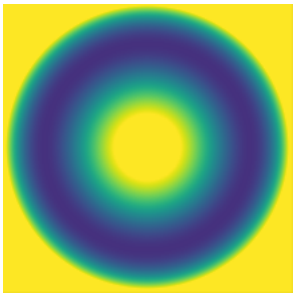

(d) Zernike polynomial $Z_4^0(r,\theta) = R_4^0(r)$.

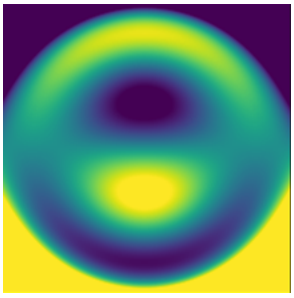

(e) Zernike polynomial $Z_5^{-1}(r,\theta) = \sin(\theta)R_5^1(r)$.

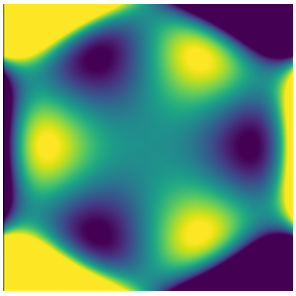

(f) Zernike polynomial $Z_5^3(r,\theta) = \cos(3\theta)R_5^3(r)$.

Figure 5.3: A couple examples of the used basis functions on the Cartesian plane $[0,1]\times[0,1]$.

would sometimes divert and produce an estimate corresponding to a local maximum of J. Therefore the Gradient Descent Method was used[21, Ch 6]. Suppose a guess $\tilde{\mathbf{u}}_0$ for the wave parameters, then the next improved estimate can be found via:

$$\tilde{\mathbf{u}}_{n+1} = \tilde{\mathbf{u}}_n - \lambda J'\big(\tilde{\mathbf{u}}_n\big) \qquad \text{for } n \in \mathbb{N}_0 \tag{5.2}$$

where λ is the step size and

$$\begin{aligned} J'(V,\mu,l,z_0,k) &= \Big(\frac{\partial J}{\partial V}, \frac{\partial J}{\partial \mu}, \frac{\partial J}{\partial l}, \frac{\partial J}{\partial z_0}, \frac{\partial J}{\partial k}\Big)(V,\mu,l,z_0,k) \\ &= 2\sum_{i,n}\big(\rho_{IW}(r_n,\theta_i) - M_{i,n}\big)\Big(\frac{\partial \rho_{IW}}{\partial V}, \frac{\partial \rho_{IW}}{\partial \mu}, \frac{\partial \rho_{IW}}{\partial l}, \frac{\partial \rho_{IW}}{\partial z_0}, \frac{\partial \rho_{IW}}{\partial k}\Big)(r_n,\theta_i) \end{aligned}$$

where $\rho_{IW}(r,\theta)$ indicates the radial velocity of the internal wave (5.1) at radius r and polar angle θ and so

$$\begin{aligned} \rho_{IW}(r,\theta) &= \big(\cos\theta_i + \mu\sin\theta_i\big)V\,\exp\big(-(\xi_{i,n}/l)^2\big)\,\cos(k\xi_{i,n}) \\ \frac{\partial \rho_{IW}}{\partial V}(r_n,\theta_i) &= (\cos\theta_i + \mu\sin\theta_i)\exp\big(-(\xi_{i,n}/l)^2\big)\cos(k\xi_{i,n}) \\ \frac{\partial \rho_{IW}}{\partial \mu}(r_n,\theta_i) &= (\cos\theta_i + \mu\sin\theta_i)V\exp\big(-(\xi_{i,n}/l)^2\big)\Big(\frac{-2r_n\xi_{i,n}}{l^2}\cos\theta_i\cos(k\xi_{i,n}) \\ &\qquad - kr_n\cos\theta_i\sin(k\xi_{i,n}) + \sin\theta_i\cos(k\xi_{i,n})\Big) \\ \frac{\partial \rho_{IW}}{\partial l}(r_n,\theta_i) &= \frac{2\xi_{i,n}^2}{l^3}(\cos\theta_i + \mu\sin\theta_i)V\exp\big(-(\xi_{i,n}/l)^2\big)\cos(k\xi_{i,n}) \\ \frac{\partial \rho_{IW}}{\partial z_0}(r_n,\theta_i) &= (\cos\theta_i + \mu\sin\theta_i)V\exp\big(-(\xi_{i,n}/l)^2\big)\cos(k\xi_{i,n})\Big(-\frac{2\xi_{i,n}}{l^2}\cos(k\xi_{i,n}) - k\sin(k\xi_{i,n})\Big) \end{aligned}$$

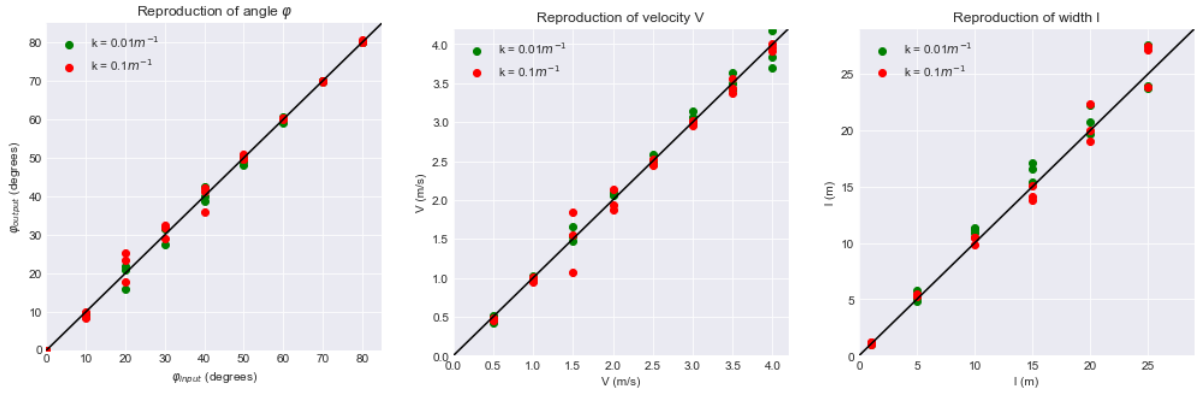

(a) Several different φ-values as input, and their reproduced results for two different k-values.

(b) Several different V-values as input, and their reproduced results for two different k-values.

(c) Several different l-values as input, and their reproduced results for two different k-values.

Figure 5.4: Reproduced internal wave parameters, where input parameters are $V = 1\text{m/s}$, $\varphi = 50°$, $l = 5\text{m}$ and $z_0 = 25\text{m}$, unless otherwise indicated.

$$\frac{\partial \rho_{IW}}{\partial k}(r_n, \theta_i) = \xi_{i,n}(\cos\theta_i + \mu \sin\theta_i) V \exp\big(-(\xi_{i,n}/l)^2\big) \sin(k\xi_{i,n}).$$

This method provided useful results which will be discussed in the next section.

5.4 Results: Internal Wave Fit

For the transducer parameters in the simulation realistic values are chosen: $N = 50$ cells, $R_0 = 2\text{m}$ and $d = 1\text{m}$, while for the internal wave parameters values were based on Stepanyants(2021). It is tested how well the velocity amplitude V, the propagation angle φ and characteristic width l can be reproduced from the measurements. As explained before any background flow is omitted in the simulation, but the background flow can still induce an extra measurement error. Suppose a zonal background flow of $U \sim 1\text{m/s}$, which is equivalent to a radial velocity of $U\cos\theta_i$ in beam i. So next to the original 2% measurement error in measuring the internal wave, an additional Gaussian error is added with standard deviation $|0.02 \times U\cos\theta_i|$. The results are in figures 5.4 for two values of the wave number k.

For each simulation the iteration started with an initial guess $\tilde{\mathbf{u}}_0$ that is the true $\mathbf{u}$ with a 10% proportional Gaussian error. The iteration was either terminated after 1500 steps, or if the cost function J is smaller than 0.2. These choices were made to limit CPU-time. The step size was $\lambda \sim 0.0001$.

The results show that the wave parameters V, φ and beam width l can be reproduced accurately with an error of roughly 0.2m/s for V, 3° for φ and 5% for l. For all parameters the proportional error seems to be within 10%. There seems to be no effect of the wave number on the accuracy of the produced estimates. Furthermore, there is for each parameter a noteworthy anomaly. Firstly for V it seems that the estimates for $V \sim 1.5\text{m/s}$ are significantly more inaccurate than for the other values. There is no clear argument why this should be the case, and moreover there are only two points deviating from the diagonal, so it could be a coincidence. Then for φ it shows that near $\varphi \sim 20°$ the estimates are more inaccurate, this is because at this input angle the position of the internal wave is a bit unfortunate: if the internal wave were more horizontal it would hit three beams, while if it were more vertical it would hit only two beams but it hits the second beam at a more acute angle. Lastly, it is notable that the error in the width-estimates seems to be proportional, whereas that is not the case for the velocity V. This is because the model is linear in V, whereas the model results are

$\rho|_{IW} \sim exp(-l^{-2})$, so only a proportional increase in l has impact. Note that for φ no proportional error is expected, since its magnitude is not physical.

5.5 Conclusion on Internal Wave Measurements

It was shown that fitting the internal wave model to the measurements yields estimates of the velocity V, angle ϕ and width l with a proportional error of no more than 10%. This should be mainly seen as a proof of concept: the buckyball is able to extract the relevant wave parameters from a passing internal wave. Comparing this ability with a conventional ADCP's ability can be done qualitatively but not quantitatively. Due to the additional beams a buckyball should be able to measure an internal wave travelling at an angle, without relying on backscatter intensity to extract the velocity and using its other beams to determine the background velocity, unlike a standard ADCP. So one could expect -also because a buckyball makes more measurements- that the buckyball provides more accurate estimates for a wider range of internal waves.

It cannot be said in a quantitative way whether the buckyball delivers more accurate estimates based on the results presented here. Firstly because the simulation set up has its weak points: it does not contain a temporal component, the measurement errors are simplified, and it is only two-dimensional. Secondly, the exact same model to generate the flow is also fitted to the synthetic measurements. So one could expect a good fit. Thirdly, the algorithm to minimize the cost function can be greatly improved upon. Here the Gradient Descent Method was chosen, since it was easy to implement, but more advanced and computationally efficient algorithms, like the Conjugate Gradient Method for example[21, Ch 6], should be used. This was not done due to time constraints. So in both the synthetic data as in the post-processing significant improvements can be made, and therefore the results are not quantifiable. In order to obtain those an experimental set up of the buckyball should be done.

The purpose of this chapter was to illustrate the buckyball's capabilities in measuring internal waves, which is lacking in the current ADCPs. This has been shown qualitatively, and can be included in the feasibility analysis of the buckyball.

Chapter 6

Conclusion and Outlook

6.1 Application of Mass Constraints

In both chapters 3 and 4 the estimates in each voxel were corrected by demanding that the mass of the water is conserved between voxels. This is a novel post-processing procedure for raw ADCP-data that seems very promising. In chapter 3 mass constraints are applied to a standard ADCP set up in a horizontally dominated flow. Here it was shown that correcting the estimates by demanding mass conservation leads to theoretically more accurate vertical velocity estimates. This was also confirmed by post-processing the actual raw ADCP-data: the new vertical velocity estimate was less noisy and physically more sound. Moreover, with this novel vertical velocity estimate the turbulence anisotropy ratio could now be estimated, whereas typically it has to be postulated. In chapter 4 mass constraints are used to correct the estimates in each voxel of a two-dimensional ADCP-buckyball. The theoretical analysis showed that depending on the local flow conditions in the voxel the corrections could improve or worsen the estimate. Similar results were provided by simulations. Over all voxels averaged the corrections did improve the estimates. Also, because with this post-processing method estimates are used to correct other nearby estimates, the (in)accuracy of the estimate in each voxel was roughly equally large as in other voxels. So as a bonus with mass constraints the buckyball could determine the flow in each direction with the same accuracy.

When comparing the findings of chapter 3 with those of chapter 4 it seems that mass constraints have more use in the conventional set up instead of the two-dimensional buckyball. However, this assessment is not completely fair. Firstly, in chapter 3 experimental data could be used to evaluate the post-processing method, whereas for the buckyball synthetic data had to be used. The simulation environment to generate this data has its weak points, such as the simplified model for the intra-beam errors. To get a fairer evaluation of the use of mass constraints with the buckyball actual experimental data is needed. Secondly, in chapter 3 an extra particular was used: the horizontally dominant flow. Using this it was assessed that the conventional horizontal flow estimates were reliable, and only the vertical estimate needed correction. A dominant flow direction would have also aided in the case of the buckyball. As was concluded in chapter 4 the angular sections where the conventional method performed well, were the sections where the mass constraint corrections did not work. So knowing a dominant flow direction would indicate the sections where the conventional method would perform well, and hence to which sections the mass constraints should be applied. For both ADCP configurations can be concluded that mass constraints are an improvement in combination with a dominant flow direction.

Also in the conventional set up and some angular sections of the buckyball it was seen that the usual homogeneity assumption can be relaxed, and that with mass constraints a linear change in the flow velocities can be handled. This indicates that mass constraints can also be of use in other ADCP-configurations, and a next step is to apply mass constrains to other configurations. It is also interesting to investigate the use of mass constraints with conventional raw ADCP-data from measurement sites

other than a shallow sea. For specifically the use of mass constraints with the buckyball a logical follow up is to extend the simulation to the three dimensions. For this setting it is expected that the corrections are also here beneficial. Moreover, mass constraints offer opportunities in determining turbulence parameters. All in all, it can be concluded that applying mass constraints can increase accuracy of ADCP-estimates, and should be investigated further.

6.2 Feasibility of the Buckyball

Results regarding the feasibility of the buckyball design were given in chapters 4 and 5. In chapter 2 as advantage of the buckyball was already mentioned that it is able to provide estimates of the flow in a multitude of directions. In chapter 4 it was shown that with mass constraints the estimates in each direction can be equally accurate. Moreover, in chapter 4 it was shown that flows that do not fulfill the homogeneity condition can still be accurately determined by a buckyball with mass constraints, see figure 4.6. So a buckyball can cover as a single moored device a larger measurement volume without introducing large inaccuracies in any particular direction.

Later in chapter 5 the main motivation for the buckyball was investigated: can a buckyball measure a more complicated flow like the shearing motion of an internal wave? With its multiple beams a buckyball should be able to reliably measure internal wave parameters. In chapter 5 a proof of concept is shown that a buckyball can measure the relevant wave parameters without the restrictions that a conventional set up has.

So based on these results a buckyball can fulfill its designated purpose. However concrete statements regarding its feasibility are difficult to make. This is mainly due to the simulated environment. In order to compare the synthetic buckyball measurements of internal waves with those of a real conventional set up the simulation has to be improved. A next step is to generalize the simulation to three dimensions, and furthermore include more realistic effects like the instrument being off-pitch and rotating. Furthermore, improvements in the internal wave model to also include solitons for example can be useful. Also upgrades in the numerical algorithm to extract the wave properties can be made. With these effects the simulation results are more realistic, and a comparison with data from other configurations can be made.

There is also an abundance of further research opportunities left. It was attempted in section 5.3.1 to reconstruct the internal wave using basis functions that allow for second-order derivatives of the streamfunction. They failed in reconstructing the internal wave, but could still be of use in reconstructing other complicated flow fields, like vortices. If this succeeds the velocity field in the whole sphere can be visualized in a continuous manner instead of being approximated by a discrete set of estimates. Furthermore, the buckyball might also be used in estimating turbulence parameters. As an example the anisotropy parameter can be estimated, since each velocity direction is measured by multiple beams. To conclude, the ADCP-buckyball offers multiple possible improvements to the standard design, as has been qualitatively shown in case of internal wave measurements.

Appendix A

Derivations in Chapter 4

In all the derivations an underlying true streamfunction $\psi(x,z)$ is used, with velocities $(u(x,z), w(x,z))$. It is assumed that its third and higher-order derivatives are negligible.

A.1 Approximation of Best Estimates

Consider a voxel $\Omega_{1,n}$ lying in the first angular section. As a first step to simplify calculations the voxel is translated a distance $\frac{r_n}{2}\sqrt{3}$ to the left along the x-axis. So the centre of the voxel lies now at the origin. Also with $h = \frac{d}{2}\sqrt{3}$ its width is denoted, and with $H = \frac{r_n}{2}$ the intersect of the top of the voxel with the vertical axis is denoted. The area $\Omega_{1,n}$ can then be described by:

$$\Omega_{1,n} : \begin{cases} -h/2 \le x \le h/2 \\ -H - \frac{x}{\sqrt{3}} \le y \le H + \frac{x}{\sqrt{3}}. \end{cases}$$

In the two following approximations Simpson's rule will be used[1]. Simpson's rule is as follows:

Suppose $f \in \mathcal{C}^4\big([a,b]\big)$ then

$$\int_a^b f(x)\,dx = \frac{b-a}{6}\big(f(a) + 4f(\frac{a+b}{2}) + f(b)\big) - \frac{1}{90}\big(\frac{b-a}{2}\big)^5 f^{(4)}(\xi) \quad \text{for } a \le \xi \le b. \tag{A.1}$$

Horizontal Velocity Estimate

For the best possible horizontal velocity estimate in the translated voxel $\Omega_{1,n}$:

$$\begin{aligned} U_{1,n} &= \frac{1}{|\Omega_{1,n}|}\int_{\Omega_{1,n}} \psi_z(x,z)\,dxdz \\ &= \frac{1}{|\Omega_{1,n}|}\int_{-h/2}^{h/2}\int_{-H-x/\sqrt{3}}^{H+x/\sqrt{3}} \psi_z(x,z)\,dzdx \\ &= \frac{1}{|\Omega_{1,n}|}\int_{-h/2}^{h/2} \psi(x, H+\frac{x}{\sqrt{3}}) - \psi(x, -H-\frac{x}{\sqrt{3}})\,dx. \end{aligned}$$

Then Simpson's rule is applied to the first part of the integral, where the notation $H_\pm = H \pm \frac{d}{4}$ is used:

$$\int_{-h/2}^{h/2} \psi(x, H+\frac{x}{\sqrt{3}})\,dx \approx \frac{h}{6}\big[\psi(-\frac{h}{2}, H_-) + 4\psi(0,H) + \psi(\frac{h}{2}, H_+)\big]$$

$$\approx h\psi(0,0) + hH\psi_z(0,0) + \frac{h^3}{24}\psi_{xx}(0,0) + h\big(\frac{H^2}{2} + \frac{d^2}{96}\big)\psi_{zz}(0,0) + \frac{dh^2}{24}\psi_{xz}(0,0)$$

where in the last step a Taylor-expansion around voxel centre $(0,0)$ is performed. A similar computation can be done to the second part of the integral:

$$\int_{-h/2}^{h/2} \psi(x, -H - \frac{x}{\sqrt{3}})\,dx \approx h\psi(0,0) - hH\psi_z(0,0) + \frac{h^3}{24}\psi_{xx}(0,0) + h\big(\frac{H^2}{2} + \frac{d^2}{96}\big)\psi_{zz}(0,0) - \frac{dh^2}{24}\psi_{xz}(0,0).$$

Combining these last two equations yields:

$$\int_{\Omega_{1,n}} \psi_z(x,z)\,dxdz \approx 2hH\psi_z(0,0) + \frac{dh^2}{12}\psi_{xz}(0,0).$$

Then, together with $|\Omega_{1,n}| = r_n \frac{d}{2}\sqrt{3} = 2hH$ the approximation is finalized:

$$\begin{aligned} U_{1,n} &\approx \frac{1}{2hH}\big(2hH\psi_z(0,0) + \frac{dh^2}{12}\psi_{xz}(0,0)\big) \\ &= \psi_z(0,0) + \frac{d^2}{24r_n}\sqrt{3}\psi_{xz}(0,0). \end{aligned} \tag{A.2}$$

Vertical Velocity Estimate

To approximate the best possible vertical velocity estimate the translated voxel $\Omega_{1,n}$ is divided into three disjoint areas:

$$\Omega_a = \begin{cases} -H_+ \le y \le -H_- \\ \sqrt{3}(y+H) \le x \le h/2 \end{cases} \tag{A.3}$$

$$\Omega_b = \begin{cases} -H_- \le y \le H_- \\ h/2 \le x \le h/2 \end{cases} \tag{A.4}$$

$$\Omega_c = \begin{cases} H_- \le y \le H_+ \\ \sqrt{3}(y-H) \le x \le h/2 \end{cases} \tag{A.5}$$

so $\Omega_{1,n} = \Omega_a \cup \Omega_b \cup \Omega_c$. Now the best possible vertical velocity estimate is:

$$\begin{aligned} W_{1,n} &= -\frac{1}{|\Omega_{1,n}|}\int_{\Omega_{1,n}} \psi_x(x,z)\,dxdz \\ &= -\frac{1}{|\Omega_{1,n}|}\Big(\int_{\Omega_a} \psi_x(x,z)\,dxdz + \int_{\Omega_b} \psi_x(x,z)\,dxdz + \int_{\Omega_c} \psi_x(x,z)\,dxdz\Big) \end{aligned}$$

Each integral is computed separately with Simpson's rule:

$$\begin{aligned} \int_{\Omega_c} \psi_x(x,z)\,dxdz &= \int_{H_-}^{H_+} \psi(\frac{h}{2}, z) - \psi(\sqrt{3}(z-H), z)\,dz \\ &\approx \frac{d}{12}\big[\psi(\frac{h}{2}, H_-) - \psi(-\frac{h}{2}, H_-) + 4\psi(\frac{h}{2}, H) - 4\psi(0, H)\big] \end{aligned}$$

$$\begin{aligned}
\int_{\Omega_a} \psi_x(x,z)\,dxdz &= \int_{-H_-}^{-H_+} \psi(\frac{h}{2},z) - \psi(\sqrt{3}(z+H),z)\,dz \\
&\approx \frac{d}{12}\big[\psi(\frac{h}{2},-H_-) - \psi(-\frac{h}{2},-H_-) + 4\psi(\frac{h}{2},-H) - 4\psi(0,-H)\big] \\
\int_{\Omega_b} \psi_x(x,z)\,dxdz &= \int_{-H_-}^{H_-} \psi(\frac{h}{2},z) - \psi(-\frac{h}{2},z)\,dz \\
&\approx \frac{H_-}{3}\big[\psi(\frac{h}{2},-H_-) - \psi(-\frac{h}{2},H_-) + 4\psi(\frac{h}{2},0) \\
&\quad - 4\psi(-\frac{h}{2},0) + \psi(\frac{h}{2},H_-) - \psi(-\frac{h}{2},H_-)\big].
\end{aligned}$$

Adding these three integrals together, and Taylor-expanding the terms around voxel centre $(0,0)$ yields:

$$\int_{\Omega_{1,n}} \psi_z(x,z) \approx 2hH\psi_x(0,0) + \frac{dh^2}{12}\psi_{xx}(0,0)$$

and dividing by $-|\Omega_{1,n}|$ produces the desired estimate:

$$W_{1,n} \approx -\psi_x(0,0) - \frac{d^2}{24r_n}\sqrt{3}\psi_{xx}(0,0). \tag{A.6}$$

Generalization

Next the voxel is translated back to its original position, so the voxel centre $(0,0)$ returns to $\mathbf{x}_{1,n} = \frac{r_n}{2}\sqrt{3}(1,0)$. Hence:

$$\begin{cases}
U_{1,n} & \approx \psi_z(\mathbf{x}_{1,n}) + \frac{d^2}{24r_n}\sqrt{3}\psi_{xz}(\mathbf{x}_{1,n}) \\
& = u(\mathbf{x}_{1,n}) - \frac{d^2}{24r_n}\sqrt{3}w_z(\mathbf{x}_{1,n}) \\
W_{1,n} & \approx -\psi_x(\mathbf{x}_{1,n}) - \frac{d^2}{24r_n}\sqrt{3}\psi_{xx}(\mathbf{x}_{1,n}) \\
& = w(\mathbf{x}_{1,n}) + \frac{d^2}{24r_n}\sqrt{3}w_x(\mathbf{x}_{1,n}).
\end{cases} \tag{A.7}$$

Using the symmetric set up of the buckyball this can be generalized to every voxel $\Omega_{i,n}$. This is done by using a polar coordinate system. Suppose radius and polar angle (r,θ) with radial and azimuthal velocities $(\rho(r,\theta),\pi(r,\theta))$. Note that $u(\mathbf{x}_{1,n}) = \rho(\frac{r_n}{2}\sqrt{3},0)$, $w(\mathbf{x}_{1,n}) = \pi(\frac{r_n}{2}\sqrt{3},0)$, $w_z(\mathbf{x}_{1,n}) = \frac{1}{r_n}\pi_\theta(r_n,0)$ and $w_x(\mathbf{x}_{1,n}) = \pi_r(\frac{r_n}{2}\sqrt{3},0)$. So (A.1) are rewritten as:

$$\begin{aligned}
U_{1,n} &\approx \rho(\frac{r_n}{2}\sqrt{3},0) - \frac{d^2}{24r_n^2}\sqrt{3}\pi_\theta(\frac{r_n}{2}\sqrt{3},0) \\
W_{1,n} &\approx \pi(\frac{r_n}{2}\sqrt{3},0) + \frac{d^2}{24r_n}\sqrt{3}\pi_r(\frac{r_n}{2}\sqrt{3},0).
\end{aligned}$$

The buckyball is rotational symmetric over angle $\frac{\pi}{6}$, and so these approximations should hold for every angular section, in other words:

$$\begin{cases}
U_{i,n} & \approx \rho(\frac{r_n}{2}\sqrt{3},\Theta_i) - \frac{d^2}{24r_n^2}\sqrt{3}\pi_\theta(\frac{r_n}{2}\sqrt{3},\Theta_i) \\
W_{i,n} & \approx \pi(\frac{r_n}{2}\sqrt{3},\Theta_i) + \frac{d^2}{24r_n}\sqrt{3}\pi_r(\frac{r_n}{2}\sqrt{3},\Theta_i).
\end{cases} \tag{A.8}$$

Now the standard transformation to Cartesian velocities:

$$\begin{aligned}
\rho(r,\theta) &= \cos(\theta)u(r\cos\theta, r\sin\theta) + \sin(\theta)w(r\cos\theta, r\sin\theta) \\
\pi(r,\theta) &= \cos(\theta)w(r\cos\theta, r\sin\theta) - \sin(\theta)u(r\cos\theta, r\sin\theta).
\end{aligned}$$

and for the gradients:

$$\begin{aligned}\frac{1}{r}\pi_\theta(r,\theta) =& \cos\theta\big(\cos(\theta)w_z(r\cos\theta, r\sin\theta) - \sin(\theta)u_z(r\cos\theta, r\sin\theta)\big)\\ &- \sin\theta\big(\cos(\theta)w_x(r\cos\theta, r\sin\theta) - \sin(\theta)u_x(r\cos\theta, r\sin\theta)\big)\\ \pi_r(r,\theta) =& \cos\theta\big(\cos(\theta)w_x(r\cos\theta, r\sin\theta) - \sin(\theta)u_x(r\cos\theta, r\sin\theta)\big)\\ &+ \sin\theta\big(\cos(\theta)w_z(r\cos\theta, r\sin\theta) - \sin(\theta)u_z(r\cos\theta, r\sin\theta)\big).\end{aligned}$$

Inserting these transformations into (A.8) produces the desired results:

$$\begin{aligned}U_{i,n} \approx& \psi_z(\mathbf{x}_{i,n}) + \frac{d^2\sqrt{3}}{24r_n}\\ &\Big(-\cos^2(\Theta_i)\cos(\theta_{i+1})\psi_{xx}(\mathbf{x}_{i,n})\\ &+\frac{1}{2}(2\cos(\Theta_i) + \sin(\theta_{i+1}) - \sin(3\theta_i))\psi_{xz}(\mathbf{x}_{i,n})\\ &+\frac{1}{4}(3\sin(\Theta_i) - 4\cos(\theta_{i+1}) + \cos(3\theta_i))\psi_{zz}(\mathbf{x}_{i,n})\Big)\\ W_{i,n} \approx& -\psi_x(\mathbf{x}_{i,n}) + \frac{d^2\sqrt{3}}{24r_n}\\ &\Big(-\sin^2(\Theta_i)\sin(\theta_{i+1})\psi_{zz}(\mathbf{x}_{i,n})\\ &+\frac{1}{2}(-2\sin(\Theta_i) + \cos(\theta_{i+1}) + \cos(3\theta_i))\psi_{xz}(\mathbf{x}_{i,n})\\ &+\frac{1}{4}(-3\cos(\Theta_i) - 4\sin(\theta_{i+1}) - \sin(3\theta_i))\psi_{xx}(\mathbf{x}_{i,n})\Big).\end{aligned}$$

A.2 Approximation of Conventional Estimates

As mentioned in section 4.3 the conventional estimates (4.4) are:

$$\begin{cases}\hat{u}_{i,n} &= \frac{2}{\sqrt{3}}\Big(\sin(\theta_i)M_{i-1,n} - \sin(\theta_{i-1})M_{i,n}\Big)\\ \hat{w}_{i,n} &= \frac{2}{\sqrt{3}}\Big(\cos(\theta_{i-1})M_{i,n} - \cos(\theta_i)M_{i-1,n}\Big).\end{cases}$$

and the measurements can be expressed in the streamfunction as:

$$M_{i,n} = \cos(\theta_i)\psi_z(\mathbf{s}_{i,n}) - \sin(\theta_i)\psi_x(\mathbf{s}_{i,n})$$

where $\mathbf{s}_{i,n} = r_n(\cos\theta_i, \sin\theta_i)$ is the measurement point. First a Taylor expansion of $M_{i,n}$ and $M_{i-1,n}$ around voxel centre $\mathbf{x}_{i,n}$ is done, where $h_n = \frac{r_n}{2}\sqrt{3}$ denotes the distance of the voxel centre to origin:

$$\begin{aligned}M_{i,n} =& \cos(\theta_i)\psi_z(\mathbf{s}_{i,n}) - \sin(\theta_i)\psi_x(\mathbf{s}_{i,n})\\ =& \cos(\theta_i)\Big[\psi_z(\mathbf{x}_{i,n}) + (r_n\cos\theta_i - h_n\cos\Theta_i)\psi_{xz}(\mathbf{x}_{i,n}) + (r_n\sin\theta_i - h_n\sin\Theta_i)\psi_{zz}(\mathbf{x}_{i,n})\Big]\\ &- \sin(\theta_i)\Big[\psi_x\mathbf{x}_{i,n}) + (r_n\cos\theta_i - h_n\cos\Theta_i)\psi_{xx}(\mathbf{x}_{i,n}) + (r_n\sin\theta_i - h_n\sin\Theta_i)\psi_{xz}(\mathbf{x}_{i,n})\Big]\\ =& \cos\theta_i\psi_z(\mathbf{x}_{i,n}) - \sin\theta_i\psi_x(\mathbf{x}_{i,n})\\ &- r_n\sin\theta_i(\cos\theta_i - \frac{\sqrt{3}}{2}\cos\Theta_i)\psi_{xx}(\mathbf{x}_{i,n}) + r_n\cos\theta_i(\sin\theta_i - \frac{\sqrt{3}}{2}\sin\Theta_i)\psi_{zz}(\mathbf{x}_{i,n})\\ &+ (r_n\cos\theta_i(\cos\theta_i - \frac{\sqrt{3}}{2}\cos\Theta_i) - r_n\sin\theta_i(\sin\theta_i - \frac{\sqrt{3}}{2}\sin\Theta_i)\psi_{xz}(\mathbf{x}_{i,n})\end{aligned}$$

and similarly:

$$\begin{aligned}
M_{i-1,n} =& \cos\theta_{i-1}\psi_z(\mathbf{x}_{i,n}) - \sin\theta_{i-1}\psi_x(\mathbf{x}_{i,n}) \\
&- r_n \sin\theta_{i-1}(\cos\theta_{i-1} - \frac{\sqrt{3}}{2}\cos\Theta_i)\psi_{xx}(\mathbf{x}_{i,n}) + r_n\cos\theta_{i-1}(\sin\theta_{i-1} - \frac{\sqrt{3}}{2}\sin\Theta_i)\psi_{zz}(\mathbf{x}_{i,n}) \\
&+ (r_n\cos\theta_{i-1}(\cos\theta_{i-1} - \frac{\sqrt{3}}{2}\cos\Theta_i) - r_n\sin\theta_{i-1}(\sin\theta_{i-1} - \frac{\sqrt{3}}{2}\sin\Theta_i)\psi_{xz}(\mathbf{x}_{i,n}).
\end{aligned}$$

Inserting both these expressions for $M_{i,n}$ and $M_{i-1,n}$ into (4.4) produces the desired results:

$$\begin{aligned}
\hat{u}_{i,n} \approx& \psi_z(\mathbf{x}_{i,n}) + \frac{2}{\sqrt{3}}r_n \\
&\Big[\sin(\theta_{i-1})\sin(\theta_i)(\cos(\theta_i) - \cos(\theta_{i-1}))\psi_{xx}(\mathbf{x}_{i,n}) \\
&- (\sin(\theta_{i-1})\sin(\theta_i)(\cos(\theta_i) - \cos(\theta_{i-1})) + \frac{3}{4}\sin(\Theta_i))\psi_{zz}(\mathbf{x}_{i,n}) \\
&+ (\sin(\theta_i)\cos(2\theta_{i-1}) - \sin(\theta_{i-1})\cos(2\theta_i) - \frac{3}{4}\cos(\Theta_i))\psi_{xz}(\mathbf{x}_{i,n})\Big] \\
\hat{w}_{i,n} \approx& -\psi_z(\mathbf{x}_{i,n}) + \frac{2}{\sqrt{3}}r_n \\
&\Big[\cos(\theta_{i-1})\cos(\theta_i)(\sin(\theta_i) - \sin(\theta_{i-1}))\psi_{zz}(\mathbf{x}_{i,n}) \\
&- (\cos(\theta_{i-1})\cos(\theta_i)(\sin(\theta_i) - \sin(\theta_{i-1})) - \frac{3}{4}\cos(\Theta_i))\psi_{xx}(\mathbf{x}_{i,n}) \\
&- (\cos(\theta_i)\cos(2\theta_{i-1}) - \cos(\theta_{i-1})\cos(2\theta_i) - \frac{3}{4}\sin(\Theta_i))\psi_{xz}(\mathbf{x}_{i,n})\Big].
\end{aligned}$$

A.3 Mass Conservation of Enclosed Hexagons

The sum over all measurements within the same ring can be approximated as follows:

$$\begin{aligned}
\sum_{i=1}^{6} M_{i,n} &= \sum_{i=1}^{6}\big[\cos\theta_i\psi_z(\mathbf{s}_{i,n}) - \sin\theta_i\psi_x(\mathbf{s}_{i,n})\big] \\
&\approx \sum_{i=1}^{6}\big[\cos\theta_i[\psi_z(0,0) + r_n\cos\theta_i\psi_{xz}(0,0) + r_n\sin\theta_i\psi_{zz}(0,0)] \\
&\quad - \sin\theta_i[\psi_x(0,0) + r_n\cos\theta_i\psi_{xx}(0,0) + r_n\sin\theta_i\psi_{xz}(0,0)]\big] \\
&\qquad \text{where a first order Taylor expansion around the origin is done} \\
&= \psi_z(0,0)\sum_{i=1}^{6}\cos\theta_i - \psi_z(0,0)\sum_{i=1}^{6}\sin\theta_i \\
&\quad + r_n\big[(\psi_{zz}(0,0) - \psi_{xx}(0,0))/2\sum_{i=1}^{6}\sin 2\theta_i + \psi_{xz}(0,0)\sum_{i=1}^{6}\cos 2\theta_i\big] \\
&= 0.
\end{aligned}$$

Summing over (4.9) yields:

$$\sum_{i=1}^{6}\bar{\rho}_{i,n} = \frac{r_n - d/2}{r_n + d/2}\sum_{i=1}^{6}\bar{\rho}_{i,n-2} - \frac{2d}{2r_n + d}\sum_{i=1}^{6}\bar{\rho}_{i,n-1} + 0$$

and this equation can be reiterated with (4.9) till $\sum_{i=1}^{6}\bar{\rho}_{i,1}$ and $\sum_{i=1}^{6}\bar{\rho}_{i,2}$ are the only remaining sums. Now note that $\bar{\rho}_{i,1}=\hat{\rho}_{i,1}$ and $\bar{\rho}_{i,2}=\hat{\rho}_{i,2}$ and that:

$$\begin{aligned}\sum_{i=1}^{6}\hat{\rho}_{i,n} &= \frac{1}{\sqrt{3}}\sum_{i=1}^{6}M_{i,n}+M_{i-1,n}\\ &= 0 \text{ with the previous results,}\end{aligned}$$

and so $\sum_{i=1}^{6}\bar{\rho}_{i,n}$ must be zero too. Hence $\sum_{i=1}^{6}M_{i,n}$ and $\sum_{i=1}^{6}\bar{\rho}_{i,n}$ are zero up to second-order Taylor-expansion of the streamfunction.

A.4 Fit of Azimuthal Estimators

So derived is the iterative equation (4.13):

$$\bar{\pi}_{i,n}=\bar{\pi}_{i-1,n}+\frac{r_n}{2d\sqrt{3}}\Big(\bar{\rho}_{i,n-1}-\bar{\rho}_{i,n+1}+\bar{\rho}_{i-1,n-1}-\bar{\rho}_{i-1,n+1}\Big)-M_{i-1,n},$$

and together with $\bar{\pi}_{1,n}=\omega_n$ all the new azimuthal estimators can be derived, as is partly done in (4.14):

$$\begin{aligned}
\bar{\pi}_{1,n} &= \omega_n\\
\bar{\pi}_{2,n} &= \omega_n+\frac{r_n}{2d\sqrt{3}}\Big(\bar{\rho}_{2,n-1}-\bar{\rho}_{2,n+1}+\bar{\rho}_{1,n-1}-\bar{\rho}_{1,n+1}\Big)-M_{1,n}\\
\bar{\pi}_{3,n} &= \omega_n+\frac{r_n}{2d\sqrt{3}}\Big(\bar{\rho}_{3,n-1}-\bar{\rho}_{3,n+1}+2\bar{\rho}_{2,n-1}-2\bar{\rho}_{2,n+1}+\bar{\rho}_{1,n-1}-\bar{\rho}_{1,n+1}\Big)-M_{1,n}-M_{2,n}\\
\bar{\pi}_{4,n} &= \omega_n+\frac{r_n}{2d\sqrt{3}}\Big(\bar{\rho}_{4,n-1}-\bar{\rho}_{4,n+1}+2\bar{\rho}_{3,n-1}-2\bar{\rho}_{3,n+1}+2\bar{\rho}_{2,n-1}-2\bar{\rho}_{2,n+1}+\bar{\rho}_{1,n-1}-\bar{\rho}_{1,n+1}\Big)\\
&\quad -M_{1,n}-M_{2,n}-M_{3,n}\\
\bar{\pi}_{5,n} &= \omega_n+\frac{r_n}{2d\sqrt{3}}\Big(\bar{\rho}_{5,n-1}-\bar{\rho}_{5,n+1}+2\bar{\rho}_{4,n-1}-2\bar{\rho}_{4,n+1}+2\bar{\rho}_{3,n-1}-2\bar{\rho}_{3,n+1}+2\bar{\rho}_{2,n-1}-2\bar{\rho}_{2,n+1}\\
&\quad +\bar{\rho}_{1,n-1}-\bar{\rho}_{1,n+1}\Big)-M_{1,n}-M_{2,n}-M_{3,n}-M_{4,n}\\
\bar{\pi}_{6,n} &= \omega_n+\frac{r_n}{2d\sqrt{3}}\Big(\bar{\rho}_{6,n-1}-\bar{\rho}_{6,n+1}+2\bar{\rho}_{5,n-1}-2\bar{\rho}_{5,n+1}+2\bar{\rho}_{4,n-1}-2\bar{\rho}_{4,n+1}+2\bar{\rho}_{3,n-1}-2\bar{\rho}_{3,n+1}\\
&\quad +2\bar{\rho}_{2,n-1}-2\bar{\rho}_{2,n+1}+\bar{\rho}_{1,n-1}-\bar{\rho}_{1,n+1}\Big)-M_{1,n}-M_{2,n}-M_{3,n}-M_{4,n}-M_{5,n}
\end{aligned}$$

Now ω_n is determined by fitting the expressions (4.14) to the conventional estimates:

$$\omega_n=\arg\min\sqrt{\sum_{i=1}^{6}(\bar{\pi}_{i,n}-\hat{\pi}_{i,n})^2}.$$

This is done by equalizing its derivative with respect to ω_n to zero:

$$\begin{aligned}0 &= \frac{\partial}{\partial\omega_n}\sqrt{\sum_{i=1}^{6}(\bar{\pi}_{i,n}-\hat{\pi}_{i,n})^2}\\ &= \frac{\sum_{i=1}^{6}\bar{\pi}_{i,n}-\hat{\pi}_{i,n}}{\sqrt{\sum_{i=1}^{6}(\bar{\pi}_{i,n}-\hat{\pi}_{i,n})^2}}\end{aligned}$$

and so

$$\begin{aligned}
0 &= \sum_{i=1}^{6} \bar{\pi}_{i,n} - \hat{\pi}_{i,n} \\
&= 6\omega_n + \frac{r_n}{2d\sqrt{3}}\Big(\bar{\rho}_{6,n-1} - \bar{\rho}_{6,n+1} + 3\bar{\rho}_{5,n-1} - 3\bar{\rho}_{5,n+1} + 5\bar{\rho}_{4,n-1} - 5\bar{\rho}_{4,n+1} + 7\bar{\rho}_{3,n-1} - 7\bar{\rho}_{3,n+1} \\
&\quad + 9\bar{\rho}_{2,n-1} - 9\bar{\rho}_{2,n+1} + 5\bar{\rho}_{1,n-1} - 5\bar{\rho}_{1,n+1}\Big) - 5M_{1,n} - 4M_{2,n} - 3M_{3,n} - 2M_{4,n} - M_{5,n} - \sum_{i=1}^{6} \hat{\pi}_{i,n}.
\end{aligned}$$

Hence it can be concluded:

$$\begin{aligned}
\omega_n &= \frac{1}{6}\sum_{i=1}^{6} \hat{\pi}_{i,n} - \frac{1}{6}\frac{r_n}{2d\sqrt{3}}\Big(\bar{\rho}_{6,n-1} - \bar{\rho}_{6,n+1} + 3\bar{\rho}_{5,n-1} - 3\bar{\rho}_{5,n+1} + 5\bar{\rho}_{4,n-1} - 5\bar{\rho}_{4,n+1} \\
&\quad + 7\bar{\rho}_{3,n-1} - 7\bar{\rho}_{3,n+1} + 9\bar{\rho}_{2,n-1} - 9\bar{\rho}_{2,n+1} + 5\bar{\rho}_{1,n-1} - 5\bar{\rho}_{1,n+1}\Big) \\
&\quad + \frac{1}{6}\Big(5M_{1,n} + 4M_{2,n} + 3M_{3,n} + 2M_{4,n} + M_{5,n}\Big) \\
&= \frac{1}{6}\sum_{i=1}^{6} \hat{\pi}_{i,n} + \frac{1}{6}\big(3M_{1,n} + 2M_{2,n} + M_{3,n} - M_{5,n} - 2M_{6,n}\big) \\
&\quad + \frac{1}{6}\frac{r_n}{d\sqrt{3}}\big(2\bar{\rho}_{6,n-1} - 2\bar{\rho}_{6,n+1} + \bar{\rho}_{5,n-1} - \bar{\rho}_{5,n+1} - \bar{\rho}_{3,n-1} + \bar{\rho}_{3,n+1} - 2\bar{\rho}_{2,n-1} + 2\bar{\rho}_{2,n+1}\big)
\end{aligned}$$

where in the last step it is used that $\sum_{i=1}^{6} M_{i,n} = 0$ and $\sum_{i=1}^{6} \bar{\rho}_{i,n\pm1} = 0$. Now note that since $\hat{\pi}_{i,n} = M_{i,n} - M_{i-1,n}$ that $\sum_{i=1}^{6} \hat{\pi}_{i,n} = 0$. Therefore the final expression:

$$\begin{aligned}
\omega_n &= \frac{1}{6}\big(3M_{1,n} + 2M_{2,n} + M_{3,n} - M_{5,n} - 2M_{6,n}\big) \\
&\quad + \frac{1}{6}\frac{r_n}{d\sqrt{3}}\big(2\bar{\rho}_{6,n-1} - 2\bar{\rho}_{6,n+1} + \bar{\rho}_{5,n-1} - \bar{\rho}_{5,n+1} - \bar{\rho}_{3,n-1} + \bar{\rho}_{3,n+1} - 2\bar{\rho}_{2,n-1} + 2\bar{\rho}_{2,n+1}\big)
\end{aligned}$$

A.5 Error in Radial Estimates

Consider only angular section 1 for simplicity and let $\epsilon_{1,n}$ denote the error in the radial estimates $\bar{u}_{1,n}$. So,

$$\bar{\rho}_{1,n} = \psi_z(\mathbf{x}_{1,n}) + \epsilon_{1,n},$$

and inserting this into (4.9):

$$\begin{aligned}
\bar{\rho}_{1,n+1} &= \frac{R_n}{R_{n-1}}\bar{\rho}_{1,n-1} - \frac{d}{2R_n}(\bar{\rho}_{6,n-1} + \bar{\rho}_{2,n-1}) + \frac{d\sqrt{3}}{R_n}(\hat{\pi}_{6,n} - \hat{\pi}_{2,n}) \\
&= \frac{R_n}{R_{n-1}}(\psi_z(\mathbf{x}_{1,n-1}) + \epsilon_{1,n-1}) - \frac{d}{2R_n}(\frac{\sqrt{3}}{2}(\psi_x(\mathbf{x}_{6,n}) - \psi_x(\mathbf{x}_{2,n}) \\
&\quad + \frac{1}{2}(\psi_z(\mathbf{x}_{6,n}) + \psi_z(\mathbf{x}_{2,n}) + \epsilon_{6,n-1} + \epsilon_{2,n-1}) + \frac{d\sqrt{3}}{R_n}(M_{6,n} - M_{5,n} - M_{2,n} + M_{1,n})
\end{aligned}$$

where $R_n = r_n + d/2$. Then Taylor-expanding this expression around the relevant voxel centre $\mathbf{x}_{1,n+1}$ yields:

$$\bar{\rho}_{1,n+1} = \psi_z(\mathbf{x}_{1,n+1}) + \frac{d}{R_n}\big(r_n(\sqrt{3} - \frac{3}{4}) + \frac{3}{4}(\sqrt{3} - 1)d\big)\psi_{xz}(\mathbf{x}_{1,n+1})$$

$$+ \frac{R_{n-1}}{R_n}\epsilon_{1,n-1} - \frac{d}{2R_n}(\epsilon_{6,n-1} + \epsilon_{2,n-1})$$

which implies

$$\begin{aligned}
\epsilon_{1,n+1} &= \frac{d}{R_n}\big(r_n(\sqrt{3} - \frac{3}{4}) + \frac{3}{4}(\sqrt{3}-1)d\big)\psi_{xz}(\mathbf{x}_{1,n+1}) \\
&\quad + \frac{R_{n-1}}{R_n}\epsilon_{1,n-1} - \frac{d}{2R_n}(\epsilon_{6,n-1} + \epsilon_{2,n-1}) \\
&\approx \frac{d}{R_n} r_n \psi_{xz}(\mathbf{x}_{1,n+1}) + \frac{R_{n-1}}{R_n}\epsilon_{1,n-1} - \frac{d}{2R_n}(\epsilon_{6,n-1} + \epsilon_{2,n-1}) \\
&\quad \text{since } \sqrt{3} - \frac{3}{4} \approx 1 \text{ and } d \ll R_n \\
&\approx \frac{d}{R_n} r_n \psi_{xz}(\mathbf{x}_{1,n+1}) + \frac{R_{n-1}}{R_n}\epsilon_{1,n-1} \\
&\quad \text{since } d \ll R_{n-1} \text{ and it is assumed that } \epsilon_{1,n_1} \text{ is as large as } \epsilon_{2,n-1} \text{ and } \epsilon_{6,n-1} \\
&\approx d\psi_{xz}(\mathbf{x}_{1,n+1}) + \frac{R_{n-1}}{R_n}\epsilon_{1,n-1} \\
&\quad \text{since } r_n \approx R_n \text{ for large } n.
\end{aligned}$$

Reiterating this expression a couple of times yields:

$$\begin{aligned}
\epsilon_{1,n} &\approx d\psi_{xz}(\mathbf{x}_{1,n}) + \frac{R_{n-2}}{R_{n-1}}\epsilon_{1,n-2} \\
&\approx d\psi_{xz}(\mathbf{x}_{1,n}) + d\frac{R_{n-2}}{R_{n-1}}\psi_{xz}(\mathbf{x}_{1,n}) + \frac{R_{n-2}}{R_{n-1}}\frac{R_{n-4}}{R_{n-3}}\epsilon_{1,n-4} \\
&\approx d\psi_{xz}(\mathbf{x}_{1,n}) + d\frac{R_{n-2}}{R_{n-1}}\psi_{xz}(\mathbf{x}_{1,n}) + \frac{R_{n-2}}{R_{n-1}}\frac{R_{n-4}}{R_{n-3}}\psi_{xz}(\mathbf{x}_{1,n}) + \frac{R_{n-2}}{R_{n-1}}\frac{R_{n-4}}{R_{n-3}}\frac{R_{n-6}}{R_{n-5}}\epsilon_{1,n-6}
\end{aligned}$$

where it is used that $\psi_{xz}(\mathbf{x}_{1,n}) = \psi_{xz}(\mathbf{x}_{1,n-2})$ since third and higher-order derivatives are negligible. Now, denote $\kappa_n = \frac{R_{n-2}}{R_{n-1}}$, and note that $\frac{R_{n-j}}{R_{n-j+1}} < \kappa_n$ for all $j > 2$. Then

$$\begin{aligned}
\epsilon_{1,n} &< \big(1 + \kappa_n + \kappa_n^2 + \cdots + \kappa_n^{\lfloor \frac{n-1}{2} \rfloor}\big) d\psi_{xz}(\mathbf{x}_{1,n}) + \kappa_n^{\lfloor \frac{n+1}{2} \rfloor}\epsilon_{1,t} \\
&\quad \text{where } t = 1 \text{ if } n \text{ odd and } t = 2 \text{ if } n \text{ even} \\
&\approx \frac{1 - \kappa_n^{\lfloor \frac{n+1}{2} \rfloor}}{1 - \kappa_n} d\psi_{xz}(\mathbf{x}_{1,n}) \\
&\quad \text{where the error in the inner two rings is neglected: } \epsilon_{1,t} \approx 0 \\
&\approx \frac{1 - (1 - \lfloor \frac{n+1}{2} \rfloor \frac{d}{R_{n-1}})}{d/R_{n-1}} d\psi_{xz}(\mathbf{x}_{1,n}) \\
&\quad \text{where a first-order Taylor expansion around } \kappa_n = 1 \text{ is done} \\
&\approx \lfloor \frac{n+1}{2} \rfloor d\psi_{xz}(\mathbf{x}_{1,n}) \\
&\approx \frac{r_n}{2}\psi_{xz}(\mathbf{x}_{1,n}).
\end{aligned}$$

A.6 Error in Azimuthal Estimates

Consider only angular section 1 for simplicity. The corrected azimuthal estimate is given by (4.16):

$$\begin{aligned}\bar{\pi}_{1,n} = &\frac{1}{6}\big(3M_{1,n} + 2M_{2,n} + M_{3,n} - M_{5,n} - 2M_{6,n}\big) \\ &+ \frac{1}{6}\frac{r_n}{d\sqrt{3}}\big(2\bar{\rho}_{6,n-1} - 2\bar{\rho}_{6,n+1} + \bar{\rho}_{5,n-1} - \bar{\rho}_{5,n+1} - \bar{\rho}_{3,n-1} + \bar{\rho}_{3,n+1} - 2\bar{\rho}_{2,n-1} + 2\bar{\rho}_{2,n+1}\big)\end{aligned}$$

Now note, building on the derivation in section A.5, that:

$$\begin{aligned}\bar{\rho}_{1,n+1} - \bar{\rho}_{1,n-1} &= \psi_z(\mathbf{x}_{1,n+1}) + \epsilon_{1,n+1} - \psi_z(\mathbf{x}_{1,n-1}) - \epsilon_{1,n-1} \\ &\approx \frac{d}{\sqrt{3}}\psi_{xz}(\mathbf{x}_{1,n+1}) + \epsilon_{1,n+1} - \epsilon_{1,n-1} \\ &\approx \frac{d}{\sqrt{3}}\psi_{xz}(\mathbf{x}_{1,n+1}) + d\psi_{xz}(\mathbf{x}_{1,n+1}) + \big(\frac{R_{n-1}}{R_n} - 1\big)\epsilon_{1,n-1} \\ &= d\big(1 + \frac{1}{\sqrt{3}}\big)\psi_{xz}(\mathbf{x}_{1,n+1}) - \frac{d}{R_n}\epsilon_{1,n-1} \\ &\quad \text{since } d \ll R_n \\ &\approx d\big(1 + \frac{1}{\sqrt{3}}\big)\psi_{xz}(\mathbf{x}_{1,n+1}).\end{aligned}$$

This is generalized to any angular section using the transforms to polar coordinates:

$$\begin{aligned}\bar{\rho}_{i,n+1} - \bar{\rho}_{i,n-1} \approx d\big(1 + \frac{1}{\sqrt{3}}\big)\big[&\cos\Theta_i \cos\theta_{i+1}\psi_{xx}(\mathbf{x}_{i,n}) \\ &+ \sin(\theta_{i+1} + \Theta_i)\psi_{xz}(\mathbf{x}_{i,n}) \\ &+ \sin\Theta_i \sin\theta_{i+1}\psi_{zz}(\mathbf{x}_{i,n})\big]\end{aligned}$$

So the expression for $\bar{\pi}_{1,n}$ becomes:

$$\begin{aligned}\bar{\pi}_{1,n} = &\frac{1}{6}\big(3M_{1,n} + 2M_{2,n} + M_{3,n} - M_{5,n} - 2M_{6,n}\big) \\ &+ \frac{1}{6}\frac{r_n}{\sqrt{3}}\big(1 + \frac{1}{\sqrt{3}}\big)\frac{\sqrt{3}}{2}[\psi_{xx}(\mathbf{x}_{1,n}) - \psi_{zz}(\mathbf{x}_{1,n})] \\ &\quad \text{where it is noted that the second-order derivatives are assumed to be constant} \\ &= \frac{1}{6}\big(3M_{1,n} + 2M_{2,n} + M_{3,n} - M_{5,n} - 2M_{6,n}\big) + \frac{r_n}{12}\big(1 + \frac{1}{\sqrt{3}}\big)[\psi_{xx}(\mathbf{x}_{1,n}) - \psi_{zz}(\mathbf{x}_{1,n})] \\ &\quad \text{which is Taylor-expanded around } \mathbf{x}_{1,n} \\ &\approx -\psi_x(\mathbf{x}_{1,n}) + \frac{r_n}{\sqrt{3}}\psi_{xx}(\mathbf{x}_{1,n}) + \frac{r_n}{2\sqrt{3}}\psi_{zz}(\mathbf{x}_{1,n}) \\ &\quad \text{where the second term is neglected.}\end{aligned}$$

Let $\eta_{1,n}$ denote the error in $\bar{\pi}_{1,n}$, then

$$\begin{aligned}\eta_{1,n} &= \bar{\pi}_{1,n} + \psi_x(\mathbf{x}_{1,n}) \\ &= \frac{r_n}{\sqrt{3}}\psi_{xx}(\mathbf{x}_{1,n}) + \frac{r_n}{2\sqrt{3}}\psi_{zz}(\mathbf{x}_{1,n}).\end{aligned}$$

Appendix B

Derivations in Chapter 5

B.1 Coefficients of Fourier Transforms

B.1.1 Fourier-Bessel Transform

So the unknown streamfunction is written as linear combination of (co)sines and Bessel functions:

$$\psi(r,\theta) = \sum_{q=1}^{Q}\sum_{p=0}^{P}\Big(A_{pq}\cos(p\theta) + B_{pq}\sin(p\theta)\Big)J_p\big(\frac{\alpha_{pq}}{L}r\big)$$

where

A_{pq}, B_{pq} are real coefficients

J_p is the p^{th} Bessel function of the first kind

α_{pq} is the q^{th} positive root of J_p

and L is the radius of the disk domain that is considered, where $L = r_N + d/2$, and B_{pq} are zero for $p = 0$.

So the measurements can be expressed as:

$$\begin{aligned} M_{i,n} &= \frac{1}{r_n}\psi_\theta(r_n,\theta_i) \\ &= \frac{1}{r_n}\sum_{q=1}^{Q}\sum_{p=1}^{P} p\Big(-A_{pq}\sin(p\theta_i) + B_{pq}\cos(p\theta_i)\Big)J_p\big(\frac{\alpha_{pq}}{L}r_n\big), \end{aligned}$$

and the following orthogonality conditions hold:

$$\begin{aligned} &\int_0^{2\pi}\cos(p_1\theta)\cos(p_2\theta\,d\theta = \pi\delta_{p_1\,p_2} \\ &\int_0^{2\pi}\sin(p_1\theta)\sin(p_2\theta)\,d\theta = \pi\delta_{p_1\,p_2} \\ &\int_0^{2\pi}\cos(p_1\theta)\sin(p_2\theta\,d\theta = 0 \\ &\int_0^{1} J_p(\alpha_{p\,q_1}r)J_p(\alpha_{p\,q_2}r)r\,dr = \frac{1}{2}J_{p+1}(\alpha_{p\,q_1})^2\delta_{q_1\,q_2} \end{aligned} \tag{B.1}$$

for positive integers p_1, p_2, q_1 and q_2. Then via these conditions it follows that:

$$A_{pq} = -\frac{1}{p}\frac{2}{\pi L^2 J_{p+1}(\alpha_{pq})^2}\int_0^L\int_0^{2\pi}\Big(\frac{1}{r}\psi_\theta(r,\theta)\Big)r^2\sin(p\theta)J_p(\frac{\alpha_{pq}}{L}r)\,dr\,d\theta$$

$$B_{pq} = \frac{1}{p}\frac{2}{\pi L^2 J_{p+1}(\alpha_{pq})^2}\int_0^L\int_0^{2\pi}\Big(\frac{1}{r}\psi_\theta(r,\theta)\Big)r^2\cos(p\theta)J_p(\frac{\alpha_{pq}}{L}r)\,dr\,d\theta$$

where $p \neq 0$.

Note that coefficients A_{pq} for $p = 0$ cannot be determined, which means that the part of $\psi(r,\theta)$ that is solely dependent on the radius cannot be determined, and hence any part of the azimuthal velocity v_θ that is independent of the angle θ will be unknown. So if the buckyball is exactly at the centre of a vortex, then this would be unknown. This is unsurprising, since any velocity perpendicular to the radial beams is not measured. So A_{pq} is zero for $p = 0$. Of course since the position of the buckyball is arbitrary when measuring, it is highly unlikely that it will be at exactly the centre of a vortex.

These integral relations can be discretized as Riemann sum, and hence the coefficients are determined with:

$$A_{pq} = -\frac{1}{p}\frac{2}{\pi L^2 J_{p+1}(\alpha_{pq})^2}\sum_{i=1}^{6}\sum_{n=1}^{N}M_{i,n}r_n^2\sin(p\theta_i)J_p(\frac{\alpha_{pq}}{L}r_n)\,\Delta r_n\,\Delta\theta$$

$$B_{pq} = \frac{1}{p}\frac{2}{\pi L^2 J_{p+1}(\alpha_{pq})^2}\sum_{i=1}^{6}\sum_{n=1}^{N}M_{i,n}r_n^2\cos(p\theta_i)J_p(\frac{\alpha_{pq}}{L}r_n)\,\Delta r_n\,\Delta\theta$$

where

$$\Delta\theta = \frac{\pi}{3}$$

$$\Delta r_n = \begin{cases} R_0 + d \text{ for } n = 0 \\ d \text{ for } 1 \leq n \leq N. \end{cases}$$

With these all coefficients can be computed. To prevent aliasing the number of coefficients used is limited with $P < 6$ and $Q < N$.

B.1.2 Fourier-Zernike Transform

So the unknown streamfunction is written as linear combination of Zernike polynomials:

$$\psi(r,\theta) = \sum_{q=1}^{Q}\sum_{p=0}^{P}\Big(A_{pq}\cos(p\theta) + B_{pq}\sin(p\theta)\Big)R_q^p(\frac{r}{L})$$

where

A_{pq}, B_{pq} are real coefficients

R_q^p is the radial part of the Zernike polynomial of radial degree q and azimuthal degree p

with $L = r_N + d/2$ is the radius of the disk domain and again B_{pq} are zero for $p = 0$.

Then for the measurements:

$$\begin{aligned} M_{i,n} &= \frac{1}{r_n}\psi_\theta(r_n,\theta_i) \\ &= \frac{1}{r_n}\sum_{q=1}^{Q}\sum_{p=1}^{P}p\Big(-A_{pq}\sin(p\theta_i) + B_{pq}\cos(p\theta_i)\Big)R_q^p(\frac{r_n}{L}), \end{aligned}$$

and added to the previous orthogonality relations (B.1) is:

$$\int_0^1 R_{q_1}^p(r)R_{q_2}^p(r)r\,dr = \frac{\delta_{q_1\,q_2}}{2q_1+2}$$

for positive integers p, q_1 and q_2. Then via the orthogonality of these basis functions follows that:

$$A_{pq} = -\frac{1}{p}\frac{2q+2}{L^2}\int_0^L\int_0^{2\pi}\Big(\frac{1}{r}\psi_\theta(r,\theta)\Big)r^2\sin(p\theta)R_q^p\big(\frac{r}{L}\big)\,dr\,d\theta$$
$$B_{pq} = \frac{1}{p}\frac{2q+2}{L^2}\int_0^L\int_0^{2\pi}\Big(\frac{1}{r}\psi_\theta(r,\theta)\Big)r^2\cos(p\theta)R_q^p\big(\frac{r}{L}\big)\,dr\,d\theta$$
$$\text{where } p \neq 0,$$

where for the same reason as in section B.1.1 coefficients A_{pq} for $p = 0$ cannot be determined.

Similarly as in section B.1.1, these integral relations are discretized with Riemann sums yielding:

$$A_{pq} = -\frac{1}{p}\frac{2q+2}{L^2}\sum_{i=1}^{6}\sum_{n=1}^{N}M_{i,n}r_n^2\sin(p\theta_i)R_q^p\big(\frac{r_n}{L}\big)\,\Delta r_n\,\Delta\theta$$
$$B_{pq} = \frac{1}{p}\frac{2q+2}{L^2}\sum_{i=1}^{6}\sum_{n=1}^{N}M_{i,n}r_n^2\cos(p\theta_i)R_q^p\big(\frac{r_n}{L}\big)\,\Delta r_n\,\Delta\theta$$
$$\text{where}$$
$$\Delta\theta = \frac{\pi}{3}$$
$$\Delta r_n = \begin{cases} R_0 + d \text{ for } n = 0 \\ d \text{ for } 1 \leq n \leq N. \end{cases}$$

These produce the coefficients for the Zernike Transform, where the number of coefficients used is limited with $P < 6$ and $Q < N$ as aliasing prevention.

Bibliography

[1] Uri M Ascher and Chen Greif. *A First Course on Numerical Methods*. SIAM, 2011.

[2] Blair H Brumley et al. "Performance of a broad-band acoustic Doppler current profiler". In: *IEEE Journal of Oceanic Engineering* 16.4 (1991), pp. 402–407.

[3] Ming-Huei Chang et al. "Nonlinear internal wave properties estimated with moored ADCP measurements". In: *Journal of Atmospheric and Oceanic Technology* 28.6 (2011), pp. 802–815.

[4] Benoit Cushman-Roisin and Jean-Marie Beckers. *Introduction to geophysical fluid dynamics: physical and numerical aspects*. Academic press, 2011.

[5] Subhasisch Dey. *Fluvial hydrodynamics*. Springer, 2014.

[6] J.J. Duistermaat and W. Eckhaus. *Analyse van Gewone Differentiaalvergelijkingen*. Epsilon Uitgaven, 2015.

[7] Takahiro Endoh et al. "Estimating propagation speed and direction, and vertical displacement of second-mode nonlinear internal waves from ADCP measurements". In: *Continental Shelf Research* 233 (2022), p. 104644.

[8] Heinz Werner Engl, Martin Hanke, and Andreas Neubauer. *Regularization of inverse problems*. Vol. 375. Springer Science & Business Media, 1996.

[9] Ann E Gargett. "Observing turbulence with a modified acoustic Doppler current profiler". In: *Journal of Atmospheric and Oceanic Technology* 11.6 (1994), pp. 1592–1610.

[10] Gregory J Gbur. *Mathematical methods for optical physics and engineering*. Cambridge University Press, 2011.

[11] T. Gerkema and J.T.F. Zimmerman. *An introduction to internal waves*. Lecture notes at Royal NIOZ. 2008.

[12] Theo Gerkema, Frans–Peter A Lam, and Leo RM Maas. "Internal tides in the Bay of Biscay: conversion rates and seasonal effects". In: *Deep Sea Research Part II: Topical Studies in Oceanography* 51.25-26 (2004), pp. 2995–3008.

[13] Miguel Gilcoto, Emlyn Jones, and Luis Fariña-Busto. "Robust estimations of current velocities with four-beam broadband ADCPs". In: *Journal of Atmospheric and Oceanic Technology* 26.12 (2009), pp. 2642–2654.

[14] Romain UG Guion and Anna M Young. "The frequency response of acoustic Doppler current profilers: Spatiotemporal response and implications for tidal turbine site assessment". In: *Oceans-St. John's* (2014), pp. 1–10.

[15] Hans van Haren and Louis Gostiaux. "Detailed internal wave mixing above a deep-ocean slope". In: *Journal of Marine Research* 70.1 (2012), pp. 173–197.

[16] Karen J Heywood, S Scrope-Howe, and ED Barton. "Estimation of zooplankton abundance from shipborne ADCP backscatter". In: *Deep Sea Research Part A. Oceanographic Research Papers* 38.6 (1991), pp. 677–691.

[17] Teledyne RD Instruments. *Acoustic Doppler Current Profiler Principles of Operation: A Practical Primer*. Teledyne Technologies. La Gaude, France, 2006.

[18] Christopher R Jackson and J Apel. "An atlas of internal solitary-like waves and their properties". In: *Contract* 14.03-C (2004), p. 0176.

[19] Nishu V Kurup et al. "Study of nonlinear internal waves and impact on offshore drilling units". In: *International Conference on Offshore Mechanics and Arctic Engineering*. Vol. 44335. 2011, pp. 831–840.

[20] Yuri A. Kuznetsov and Heinz Hanßmann. *Basis Differentiaalvergelijkingen*. Lecture notes for course Differentiaalvergelijkingen at Utrecht University. 2017.

[21] Tristan van Leeuwen and Christoph Brune. *Lectures on Inverse Problems and Imaging*. Lecture notes for course Inverse Problems in Imaging at MasterMath. 2022.

[22] R Lhermitte and U Lemmin. "Probing water turbulence by high frequency Doppler sonar". In: *Geophysical Research Letters* 17.10 (1990), pp. 1549–1552.

[23] Atle Lohrmann, Bruce Hackett, and Lars Petter Røed. "High resolution measurements of turbulence, velocity and stress using a pulse-to-pulse coherent sonar". In: *Journal of Atmospheric and Oceanic Technology* 7.1 (1990), pp. 19–37.

[24] Youyu Lu and Rolf G Lueck. "Using a broadband ADCP in a tidal channel. Part I: Mean flow and shear". In: *Journal of Atmospheric and Oceanic Technology* 16.11 (1999), pp. 1556–1567.

[25] Youyu Lu and Rolf G Lueck. "Using a broadband ADCP in a tidal channel. Part II: Turbulence". In: *Journal of Atmospheric and Oceanic Technology* 16.11 (1999), pp. 1568–1579.

[26] L.R.M. Maas. *Wave Attractors*. Lecture notes for course Wave Attractors at Utrecht University. 2019.

[27] Nortek Manuals. *Principles of Operation*. Nortek. Oslo, Norway, 2017.

[28] Nortek Manuals. *The Comprehensive Manual for ADCP's*. Nortek. Oslo, Norway, 2017.

[29] Katherine McCaffrey et al. "Characterization of turbulence anisotropy, coherence, and intermittency at a prospective tidal energy site: Observational data analysis". In: *Renewable Energy* 76 (2015), pp. 441–453.

[30] Ramzi Mirshak and Daniel E Kelley. "Inferring propagation direction of nonlinear internal waves in a vertically sheared background flow". In: *Journal of Atmospheric and Oceanic Technology* 26.3 (2009), pp. 615–625.

[31] JN Moum et al. "Energy transport by nonlinear internal waves". In: *Journal of Physical Oceanography* 37.7 (2007), pp. 1968–1988.

[32] DS Mueller and C Wagner. "Measuring discharge with ADCPs from a moving boat". In: *US Geological Survey Techniques and Methods 3A-22, USGS, Reston VA* (2009).

[33] Michael W Ott. "An improvement in the calculation of ADCP velocities". In: *Journal of Atmospheric and Oceanic Technology* 19.10 (2002), pp. 1738–1741.

[34] Alberto Scotti et al. "A modified beam-to-earth transformation to measure short-wavelength internal waves with an acoustic Doppler current profiler". In: *Journal of Atmospheric and Oceanic Technology* 22.5 (2005), pp. 583–591.

[35] Mark T Stacey, Stephen G Monismith, and Jon R Burau. "Measurements of Reynolds stress profiles in unstratified tidal flow". In: *Journal of Geophysical Research: Oceans* 104.C5 (1999), pp. 10933–10949.

[36] Marek Stastna and Kevin G Lamb. "Large fully nonlinear internal solitary waves: The effect of background current". In: *Physics of fluids* 14.9 (2002), pp. 2987–2999.

[37] Yury Stepanyants. "How internal waves could lead to wreck American and Indonesian submarines?" In: *arXiv preprint arXiv:2107.00828* (2021).

[38] H.E. de Swart. *Ocean Waves.* Lecture notes for course Ocean Waves at Utrecht University. 2019.

[39] K Theriault. "Incoherent multibeam Doppler current profiler performance: Part I–Estimate variance". In: *IEEE Journal of Oceanic Engineering* 11.1 (1986), pp. 7–15.

[40] K Theriault. "Incoherent multibeam Doppler current profiler performance: Part II–Spatial response". In: *IEEE Journal of Oceanic Engineering* 11.1 (1986), pp. 16–25.

[41] N.H. Thomas and T.N. Stevenson. "A similarity solution for viscous internal waves". In: *Journal of Fluid Mechanics* 54.3 (1972), pp. 495–506.

[42] Michael Togneri et al. "Comparison of 4-and 5-beam acoustic Doppler current profiler configurations for measurement of turbulent kinetic energy". In: *Energy Procedia* 125 (2017), pp. 260–267.